Characterisation studies on the optics of the prototype fluorescence telescope FAMOUS

von

Hans Michael Eichler

Masterarbeit in Physik

vorgelegt der

Fakultät für Mathematik, Informatik und Naturwissenschaften
der Rheinisch-Westfälischen Technischen Hochschule Aachen

im März 2014

angefertigt im

III. Physikalischen Institut A

bei

Prof. Dr. Thomas Hebbeker

Erstgutachter und Betreuer

Prof. Dr. Thomas Hebbeker
III. Physikalisches Institut A
RWTH Aachen University

Zweitgutachter

Prof. Dr. Christopher Wiebusch
III. Physikalisches Institut B
RWTH Aachen University

Abstract

In this thesis, the Fresnel lens of the prototype fluorescence telescope FAMOUS, which is built at the III. Physikalisches Institut of the RWTH Aachen, is characterised. Due to the usage of silicon photomultipliers as active detector component, an adequate optical performance is required. The optical performance and transmittance of the used Fresnel lens and the qualification for the operation in the fluorescence telescope FAMOUS is examined in several series of measurements and simulations.

Zusammenfassung

In dieser Arbeit wird die Fresnel-Linse des Prototyp-Fluoreszenz-Teleskops FAMOUS charakterisiert, welches am III. Physikalischen Institut der RWTH Aachen gebaut wird. Durch die Verwendung von Silizium-Photomultipliern als aktive Detektorkomponente werden besondere Anforderungen an die Optik des Teleskops gestellt. In verschiedenen Messreihen und Simulationen wird untersucht, ob die Abbildungsqualität und die Transmission der verwendeten Fresnel-Linse für die Verwendung in diesem Fluoreszenz-Teleskop geeignet ist.

Contents

List of figures

Aurora Borealis [1]

1 Introduction

The sky and its visible phenomena hold a strong fascination for everyone. As could have been expected, the most interesting facets - especially for scientific research - are not directly visible for the human eye.

This is also the case for cosmic rays, particles having incredibly high energies up to 10^{20} eV which predominantly originate outside of our solar system, ceaselessly striking the atmosphere of the Earth. The sources and acceleration mechanisms of these particles are mostly unknown. Due to their low flux, which is below one per year and square-kilometer for energies above 10^{19} eV, the observation and corresponding studies are challenging. To collect as much statistics as possible in a certain period of time, which is - among others - the aim of the Pierre Auger Observatory, the only approach is the construction of detectors covering as much surface as possible.

As those incoming particles - also called primaries - enter the atmosphere, cascades of secondary particles are induced like in a calorimeter, containing a hadronic, muonic and electromagnetic component. Besides emitting Cherenkov radiation in flight direction, the contained electrons and positrons also excite nitrogen molecules which, as a consequence, emit fluorescence photons in the UV range isotropically distributed. Instead of observing the primary directly, this calorimetric measurement is viable at far distance, making it possible to scan a large area with only few detectors.

However, as inherent to the described principle, the fluorescence signal is weak and a detection is possible only in clear dark nights. To still allow a measurement of such low light fluxes, the use of photomultiplier tubes is quite popular because of their high photon detection sensitivity, in conjunction with a large focusing mirror.

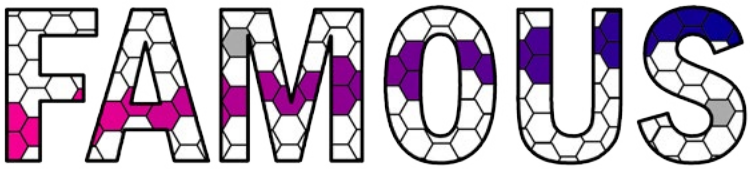

Figure 1.1: Logo of FAMOUS: "First Auger Multi pixel photon counter camera for the Observation of Ultra-high-energy cosmic ray air Showers"

As an alternative to this traditional setup, a relatively new kind of semiconductor light sensor is used as the active detector component of the prototype fluorescence telescope FAMOUS (figure 1.1). The acronym, standing for First Auger MPPC camera for the Observation of Ultra high energy cosmic ray air Showers, emphasizes the usage of so-called Multi Pixel Photon Counters - also known as silicon photomultipliers (SiPMs) which are built from a Geiger-mode avalanche photodiode array. As the name suggests, these devices are sensitive enough to detect single photons and thus are suitable to detect fluorescence radiation. In comparison to photomultiplier tubes, SiPMs operate at much lower voltage and promise a higher photon detection efficiency in the future.

For the prototype FAMOUS, a refractive telescope design was chosen using a Fresnel lens of roughly half a meter diameter. On that scale, Fresnel lenses have certain advantages in comparison to bulky lenses if image quality is of secondary importance. As a Fresnel lens is significantly thinner than its bulky counterpart, the transmittance of light in the ultraviolet regime is much higher, which is important since the characteristic spectrum of fluorescence radiation reaches from 280 nm to 420 nm. On top of that, a more compact and lightweight construction is possible.

In this thesis, the optics of the fluorescence telescope FAMOUS is characterised with special regard to the properties of the Fresnel lens, including the form of the focal point, various aberrational effects like spherical and coma aberration, distortion, curvature of field and the transmittance. Therefore, the listed effects are measured for the Fresnel lens of FAMOUS and for a conventional lens of smaller diameter to understand the influence of the experimental setup. Furthermore, the results are compared to a simulation of the setup.

As a result of this analysis, the systematic effects and influence of the Fresnel lens on the detector response of FAMOUS as well as the cooperation of the lens and the SiPM camera pixels can be better understood and quantised. The results will help to compute the uncertainties for the detected fluorescence signal.

2 Cosmic rays

When Viktor Hess launched his balloon-experiments in 1912, he opened a new window to the cosmos and hence gave birth to the modern field of astroparticle physics. His measurements were the first to indicate the existence of cosmic rays [2]. To date the explanation of the ionisation of air was based on radioactive material in the Earth. As this assumption is partially true, the ionisation rate descends on the first thousand meters of altitude. However, beyond that height, the intensity increases again, revealing a second component which seems to have an extraterrestrial origin.

Ongoing experiments were able to uncover the secrets behind these observations. With the help of new technologies, a maximum of ionisation was found to be at 15 km height. In the hope to proof that the cosmic rays are high energetic gamma rays, producing secondary compton electrons, Walter Bothe and Werner Kolhörster found a majority of charged particles that could penetrate 4.1 cm of gold, which was an inconsistent observation to the assumed theory [3]. With other experiments measuring coincidences at large lateral distances, it could be concluded that the detected radiation consists of charged particles which are produced by primary cosmic rays.

Today, these secondary particles are well understood and known as extensive air showers. The measurement of extensive air showers is an important part of modern - indirect - detection methods for cosmic rays (CR). The majority of questions which are still unanswered today, address the ultra high energy cosmic rays which have energies higher than 10^{18} eV. Due to the very low flux, neither origin nor composition of these particles is known today as they arrive isotropically at our atmosphere. By contrast, the composition of their lower energy pendants is well measured and summarised in table 2.1 [4].

Z	Element	F
1	H	540
2	He	26
3-5	Li-B	0.40
6-8	C-O	2.20
9-10	F-Ne	0.30
11-12	Na-Mg	0.22
13-14	Al-Si	0.19
15-16	P-S	0.03
17-18	Cl-Ar	0.01
19-20	K-Ca	0.02
21-25	Sc-Mn	0.05
26-28	Fe-Ni	0.12

Table 2.1: Relative abundances F of CR nuclei with E = 10.6 GeV normalised to oxygen (≡1). [4]

2.1 Energy Spectrum

One extensively studied property of cosmic rays is their energy spectrum. It shows the flux density as a function of energy. Summarising the results of many experiments, the spectrum is now measured over 31 orders of magnitude in flux and 11 orders in energy. The flux, getting steeper with energy, generally follows a power law [4]

$$\frac{\mathrm{d}^4 n}{\mathrm{d}E\ \mathrm{d}t\ \mathrm{d}\Omega\ \mathrm{d}A} \propto E^{-\gamma} \tag{1}$$

with a spectral index $\gamma = 2.7$ to $\gamma = 3.3$. Here, n is the number of incoming cosmic rays with energy E per time t, solid angle Ω and area A. This provides a first indication for nonthermal accelerating sources.

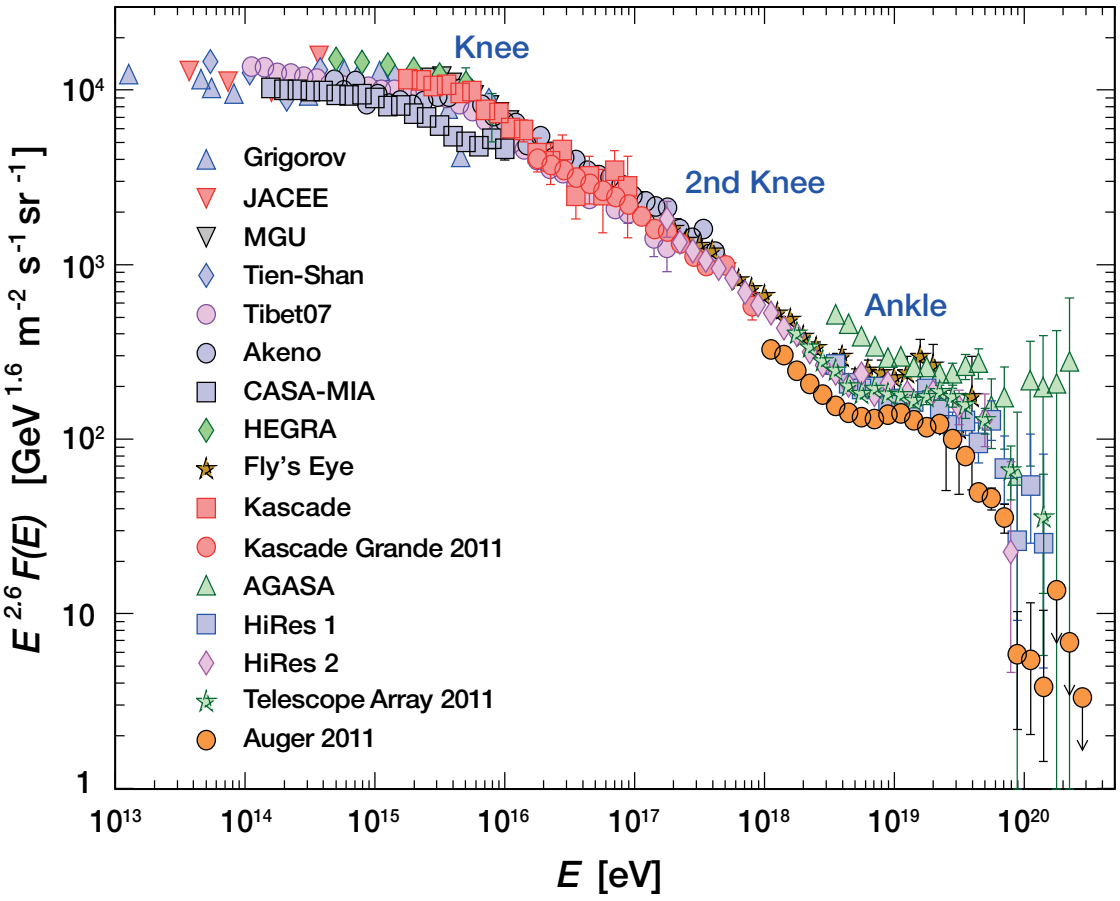

Figure 2.1: The all-particle cosmic ray spectrum as a function of the energy E compiled from different air shower measurements. The flux is multiplied by a factor $E^{2.6}$ to make the features known as knee, second knee and ankle better visible. The spectrum follows a power law with changing spectral index γ from 2.7 to 3.1. Above an energy of 10^{20} eV, the spectrum is cut off by yet undetermined reason. Taken from [2].

As marked in figure 2.1, the spectral index changes at different characteristic energies. The first feature to be identified at an energy of $10^{15.5}$ eV is known as knee. Here, the spectrum gets even steeper with energy. The spectral index changes from $\gamma = 2.7$ to $\gamma = 3.1$. At a slightly higher energy of $4 \cdot 10^{17}$ eV a second downturn to $\gamma = 3.3$ was observed later, thus it was called the second knee. In the ultra high energy regime, another feature was observed at $4 \cdot 10^{18}$ eV. As the change in spectral index is now negative, switching to $\gamma = 2.6$, this characteristic point is called ankle. At an energy of about 10^{20} eV, the spectrum cuts off.

The explanation for the observed structures is accompanied by the understanding of the acceleration and propagation mechanisms of cosmic rays which are presently debated [5]. In one of the favourite approaches, the knee is explained as a consequence of the upper limit of acceleration by galactic sources, whereas a second component for extragalactic sources, which should be harder, but less intense, would dominate the spectrum from the ankle to the highest energies [5]. Another explanation for the knee includes the magnetic field of our galaxy: The Larmor radius

$$R_l = 1.08\,\mathrm{pc}\,\frac{E/\mathrm{PeV}}{Z \cdot B/\mu\mathrm{G}} \tag{2}$$

describes the circular motion of a particle with charge Z and an energy E in presence of a magnetic field B. Evaluating the latter equation for energies above $E = 10^{18}$ eV ($= 10^3$ PeV) and magnetic field strength B of around 3 µG shows that the larmor radius for protons exceeds the thickness of the galactic disk of around 0.1 kpc[1] at that point. As a consequence, protons with such a high energy are not bound to the galaxy and will escape after a certain path length. This results in a characteristic cut-off energy for protons as well as for all other elements of the periodic table, which were all found to be part of the composition of cosmic rays, at low energies partially reflecting the element composition of the solar system. For elements with higher charge Z, the cut-off appears at higher energies. As a result, the knee might represent the cut-off for protons, followed by subsequent cut-offs for the other elements, which form the relatively flat part of the all-particle spectrum above the knee. The second knee is assumed to be formed by the cut-off of ultra heavy nuclei which represents the upper energy limit of the galactic component [3].

As mentioned before, the spectrum decreases significantly at an energy of approximately 10^{20} eV. Due to the flux, which drops below one particle per century and square-kilometer, only 47 events of energies higher than $E = 3 \cdot 10^{19}$ eV have been observed by the Pierre Auger Observatory in total [6]. Thus, it is very difficult to verify the existing theories concerning the cut-off of the all particle spectrum. The simplest explanation for this is the lack of sources capable to accelerate particles to higher energies. Besides this assumption, the Greisen-Zatsepin-Kuzmin (GZK) limit also predicts a cut-off of the spectrum above $6 \cdot 10^{19}$ eV due to significant energy losses during propagation, caused by interactions of protons with photons of the cosmic microwave background [5].

[1] The parsec is an unit of length used in astronomy. 1 pc = 3.26 ly

2.2 Sources of cosmic rays

In the previous chapter, the energy spectrum was described to follow a power law. This provides first information about the acceleration mechanisms to accelerate particles to high energies. One of the mainly accepted mechanisms by which particles gain nonthermal energies is called Fermi acceleration [7]. The main idea of this theory is multiple elastic scattering of energetic particles off magnetic turbulences, allowing them to pass many acceleration cycles in shock fronts. In each cycle, the particle energy gain is proportional to the characteristic velocity β_s = v/c of the shock front. The maximum energy of a particle E_{max} with charge Z then depends on the size R and the magnetic field strength B of the source:

$$E_{\max} \approx 10^{18}\mathrm{eV} \cdot Z\beta_s \left(\frac{R}{\mathrm{kpc}}\right) \cdot \left(\frac{B}{\mu\mathrm{G}}\right) \tag{3}$$

In the Hillas plot (cf. figure 2.2), the maximum achievable energy of known astrophysical objects are presented as a function of size and magnetic field strength. In addition, the diagonal lines denote a limit for sources to accelerate protons to 10^{20} eV. Most of the sources, except for neutron stars and possibly gamma ray bursts (GRB), seem too weak to accelerate particles to the highest energies, which have already been observed. However, the Hillas plot has to be regarded with caution since large uncertainties are involved, which are not plotted.

Apart from the acceleration of particles, which is known as the bottom-up model, another scenario is popularly proposed for the origin of cosmic rays, known as top-down model. It uses possible physics beyond the standard model of particle physics to describe the origin of ultra high energy cosmic rays: The decay of very high mass relics from the early universe, e.g. particles which could have been produced after the end of inflation, can decay into secondaries with energies even up to 10^{25} eV [8].

According to the GZK theory, particles reaching us with energies above 10^{20} eV should originate from sources closer than 100 Mpc [7]. As the eligible sources within this radius are limited, the isotropic arrival directions of particles in the energy regime which is measured is another property which is not yet understood. To develop a better understanding of the origin of ultra-high energy cosmic rays, large surface detectors like the Pierre Auger Observatory were built, to gather more statistics on using indirect detection principles: the study of extensive air showers.

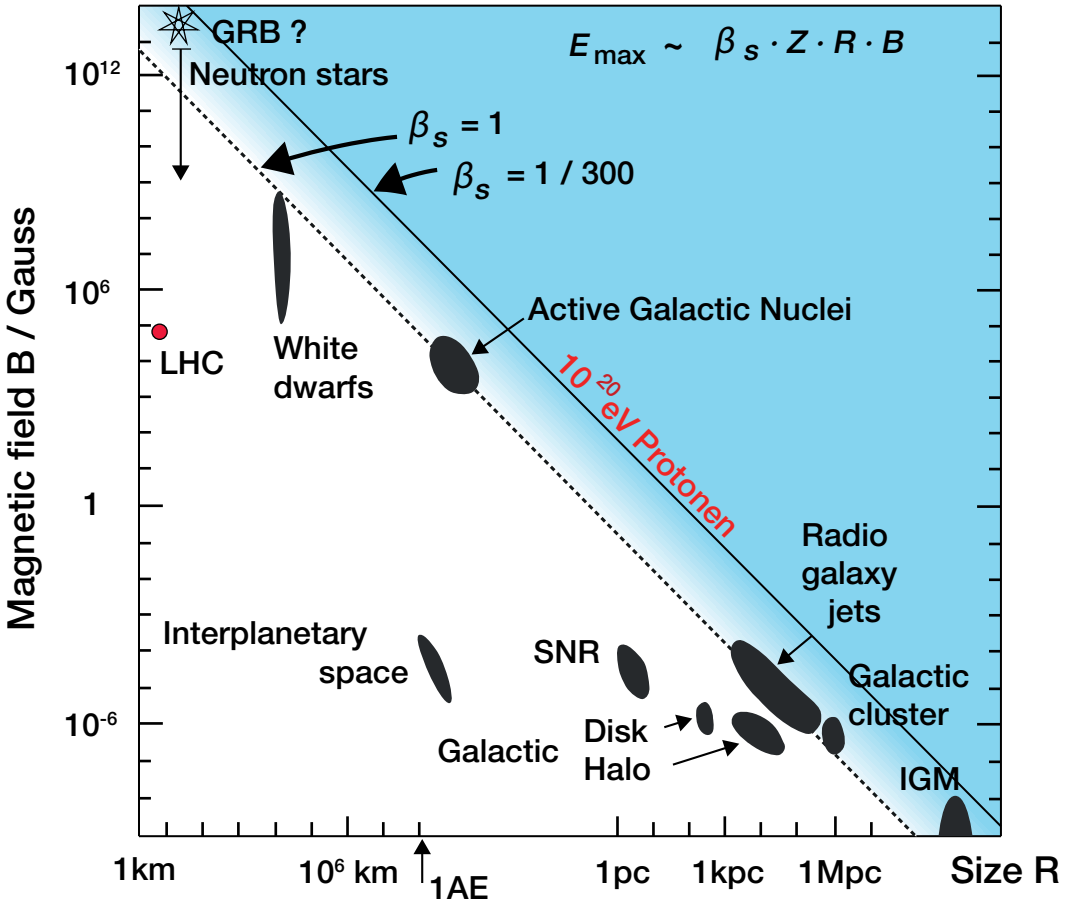

Figure 2.2: The Hillas plot illustrates known astrophysical sources for cosmic rays as a function of magnetic field strength and size of the source, to accelerate particles to the highest observed energies. The diagonal lines mark the combination of size and field strength for a source being capable of accelerating protons to 10^{20} eV with two characteristic velocities β_s. Adapted from [7].

2.3 Extensive Air Showers

When a cosmic ray enters the atmosphere of the Earth, its energy is transferred to many secondary particles, which are created due to decays and inelastic scattering with molecules of the air [7]. As a result, an avalanche of ionised particles and electromagnetic radiation evolves through the atmosphere. Despite the fact that the formation of such cascades relies on stochastic processes, they can be well described by suitable models. The analysis of extensive air showers allows to conclude on properties of the primary cosmic rays.

As illustrated in figure 2.3, the composition of an air shower for a primary particle can be separated into three components: a hadronic, an electromagnetic and a muonic. The hadronic cascade is the starting point for the two other components, as the continuous interactions also generate neutral pions, which decay almost instantly into two photons, repeatedly generating the electromagnetic component of the shower while the muonic component arises from the decay of charged pions or kaons. The dominant decay mechanisms are also summarised in figure 2.3.

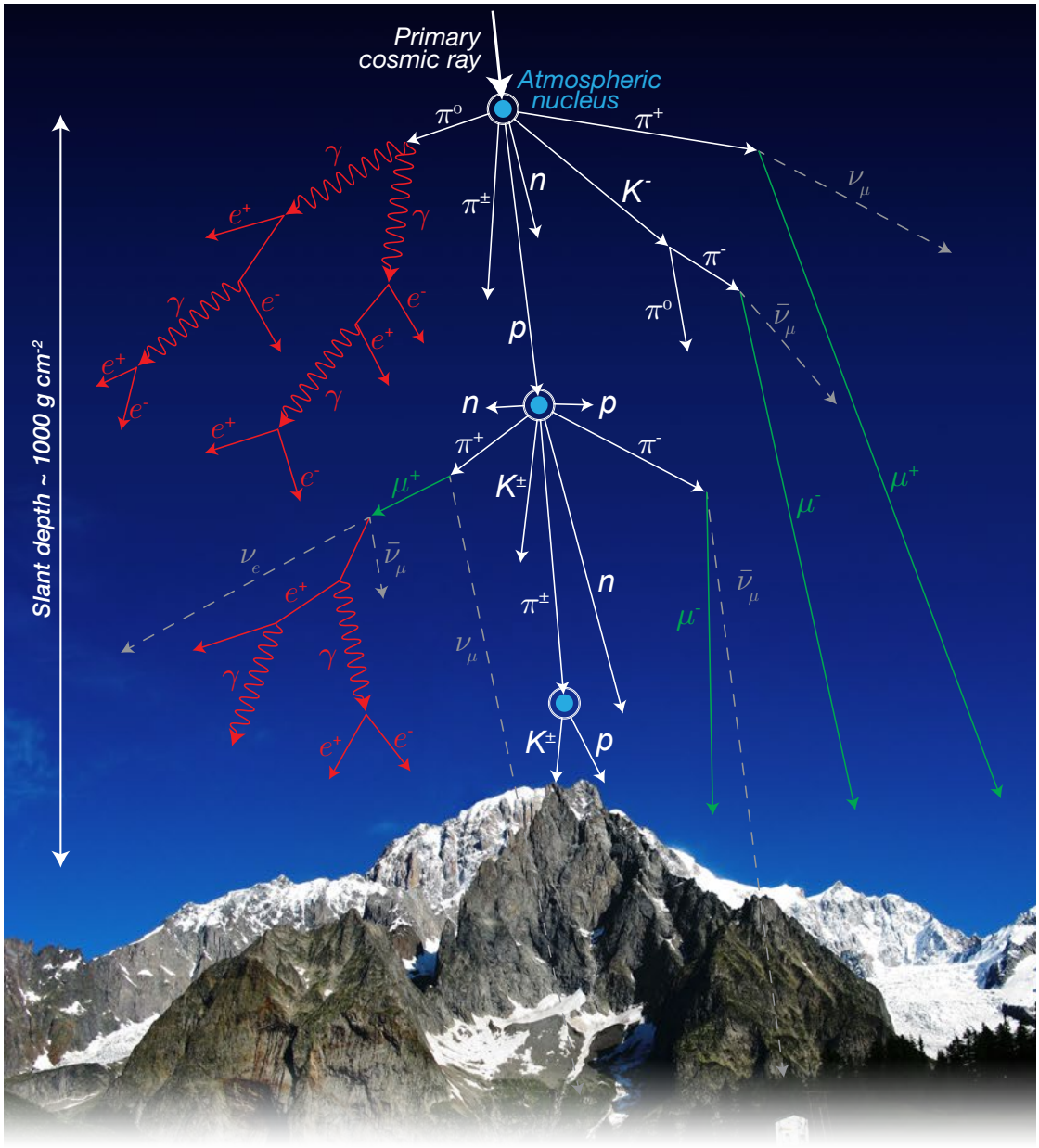

Figure 2.3: Schematic of an air shower formation in the atmosphere. The primary cosmic ray collides with an air molecule which generates unstable hadrons like pions and kaons as well as protons and neutrons. Starting from the decay of these neutral and charged hadrons, the electromagnetic and muonic components of the air shower are generated. The dominant interaction and decay processes are summarised on the bottom of the picture. Background picture adapted from [1].

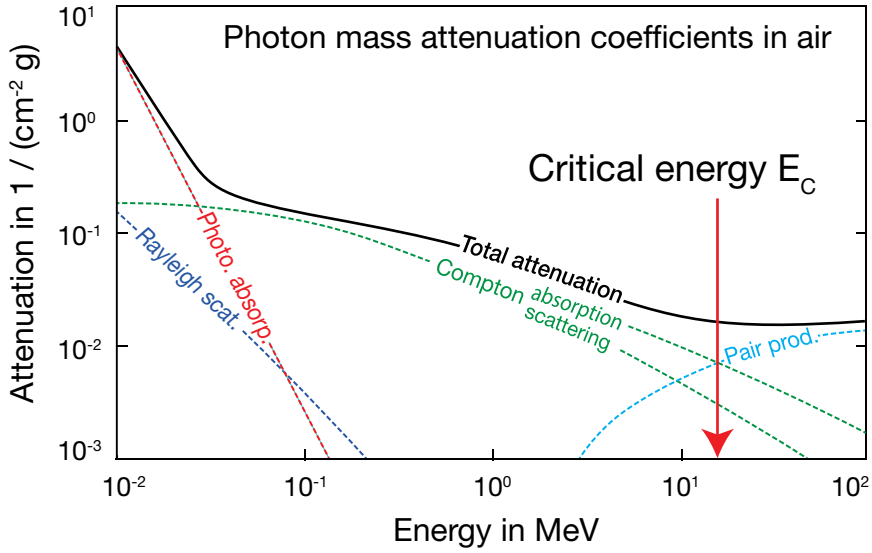

Figure 2.4: Components of the photon attenuation coefficient in 1/g cm^{-2} in air as function of the energy. At the critical energy E_C pair production becomes the most dominant effect. Adapted from [9].

The general structure of an extensive air shower depends on the incident particle. First, an electromagnetic shower, which can be induced by electrons, positrons or photons, will be discussed. A simple, but effective model to describe the development of an electromagnetic cascade was presented by Heitler [7]. The main idea of the Heitler model is that each electromagnetic particle will undergo two-body splitting after a mean interaction length λ_{int} as long as the particle energy drops below a critical energy E_C (figure 2.4), from which energy loss due to Compton scattering for photons and ionisation for charged particles become more dominant than pair production. In a first approximation, the energy of the mother particle E_0 is divided equally among the daughter particles with energy E_1:

$$E_1 = \frac{E_0}{2} \tag{4}$$

For high energetic electrons, the primary interaction process is bremsstrahlung, whereas photons convert into an electron positron pair. With this approach, the electromagnetic shower can be divided into segments with distances of λ_{int}, every segment "n" containing $N = 2^n$ particles with a resulting energy E_n for each of the particles:

$$E_n = \frac{E_0}{2^n} \tag{5}$$

As mentioned before, this process of duplication stops when the energy of the particles drops below the critical characteristic energy E_C (figure 2.4). From this point, the number of particles decreases again due to absorption processes. This allows the calculation of the stage n_{max}, that contains most particles N_{max}:

$$E_n \stackrel{!}{=} E_C \qquad n_{\max} = \frac{\ln\left(\frac{E_0}{E_C}\right)}{\ln 2} \qquad n_{\max} = \frac{E_0}{E_C} \tag{6}$$

Including the interaction length in air for the described processes, the slant depth X of the shower maximum can be determined, which describes the amount of matter that

has to be passed by integrating the density of the atmosphere ρ from a given altitude h to the top of the atmosphere using ρ_0 =1.35 kg m^{-3} and h_0 = 7.25 km:

$$X(h) = \int_h^\infty \rho(h')\mathrm{d}h' = \rho_0 e^{-h'/h_0}\mathrm{d}h' \approx 1000\,\mathrm{g\,cm^{-2}}\; e^{-h/h_0} \tag{7}$$

One of the most popular models to describe these showers is known as the Gaisser Hillas function [10]:

$$N\,(X) = N_{\max}\left(\frac{X - X_0}{X_{\max} - X_0}\right)^{\frac{X_{\max}-X_0}{\lambda}} exp\left(\frac{X_{\max} - X}{\lambda}\right) \tag{8}$$

It is used to parameterise the longitudinal particle density of extensive air showers with four parameters: $X_{\max}$ is the atmospheric depth of the shower maximum in cm^{-2} g, $N_{\max}$ the maximum number of shower particles and λ as well as X_0 are fit shape parameters, which have no direct physical meaning. As shown in figure 2.5, the parameterisation describes the longitudinal profile of a measured shower very well. In this plot, the deposited energy of the shower particles as function of the slant depth, $\mathrm{d}E/\mathrm{d}X$, is presented, which is related to the number of shower particles per slant depth. The parameters, determined with the Gaisser Hillas fit, bear information about the energy and mass of the primary particle, thus they can also be used to study the chemical composition of cosmic rays.

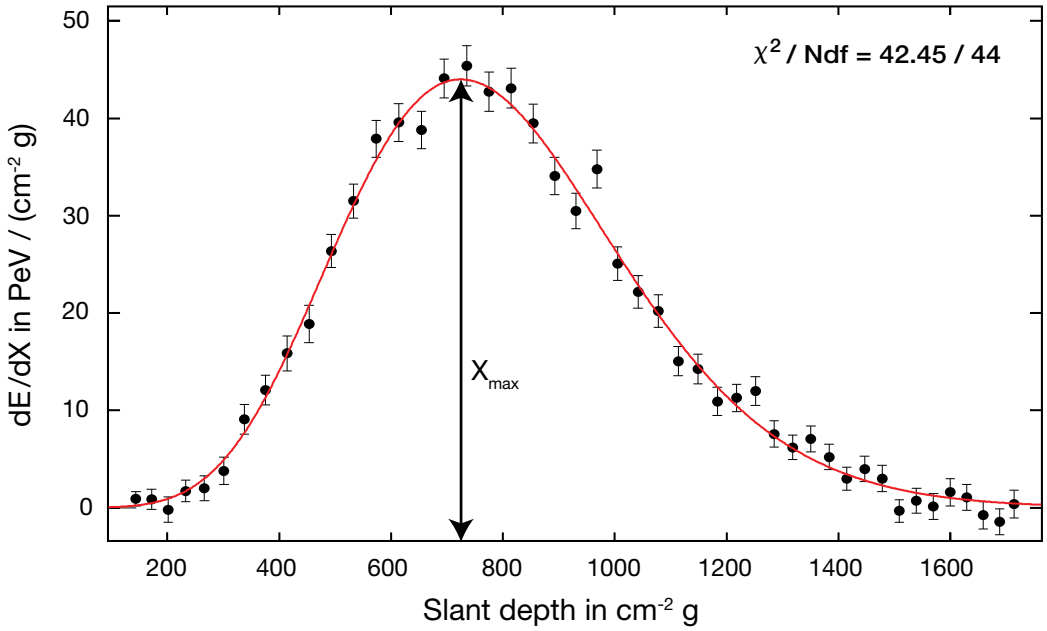

Figure 2.5: Energy deposit as a function of the slant depth X, reconstructed from the light of one air shower observed by a fluorescence telescope of the Pierre Auger Observatory. The red line denotes the Gaisser Hillas function fitted to the data. Adapted from [11].

To obtain the necessary information on the longitudinal shower profile, the fluorescence light, which is emitted by nitrogen molecules in cause of the ionising particles of the air shower, can be recorded by imaging telescopes. This fluorescence detection principle is discussed in the next chapter.

3 Fluorescence light detection

The measurement of extensive air showers by detecting the emitted fluorescence light is an established procedure. With the functionality of a calorimeter, the atmosphere of the earth becomes part of the detector. This method involves advantages as well as disadvantages. The imaging telescopes are able to record the longitudinal profile of the air showers and can also observe large areas. On the other hand, the measurement process is highly sensitive to stray light and implies relatively large systematic uncertainties dominated by the uncertainty on the fluorescence yield (14% for the Pierre Auger Observatory [12]).

3.1 Fluorescence yield

As is well known, charged particles lose energy while traversing matter. The same applies to the particles - mostly electrons[2] - of an extensive air shower propagating through the atmosphere [13]. The deposited energy is used to excite nitrogen molecules from the ground state to upper levels which are shown in figure 3.1. The transitions, which are most important for the generation of fluorescence light, are marked as colored arrows: the second positive band system of N_2, which is known as 2P and the first negative of N_2^+ known as 1N. The resulting fluorescence spectrum is depicted in figure 3.2. Beneath these radiative transitions, the excited molecules also relax in cause of collisional de-excitation called quenching. The listed processes can all be described by simple decay laws [13]:

$$\left(\frac{\mathrm{d}N^*}{\mathrm{d}t}\right)_{\mathrm{q}} = -\frac{1}{\tau_{\mathrm{q}}\left(p,T\right)}\cdot N^* \qquad \left(\frac{\mathrm{d}N^*}{\mathrm{d}t}\right)_{\mathrm{rad}} = -\frac{1}{\tau_0}\cdot N^* \qquad \frac{1}{\tau_0} = \frac{1}{\tau_{\mathrm{FL}}} + \frac{1}{\tau_{\mathrm{i_k}}} \tag{9}$$

with corresponding lifetimes τ_0 and τ_q for radiative and quenching processes and the number N^* of excited molecules per time t. Besides the radiation of fluorescence light with lifetime τ_{FL}, τ_0 also includes internal relaxation processes τ_{ik}. The time constant for de-excitation caused by quenching is dependent on pressure p and temperature T according to gas kinetic theory.

[2] and positrons

Figure 3.1

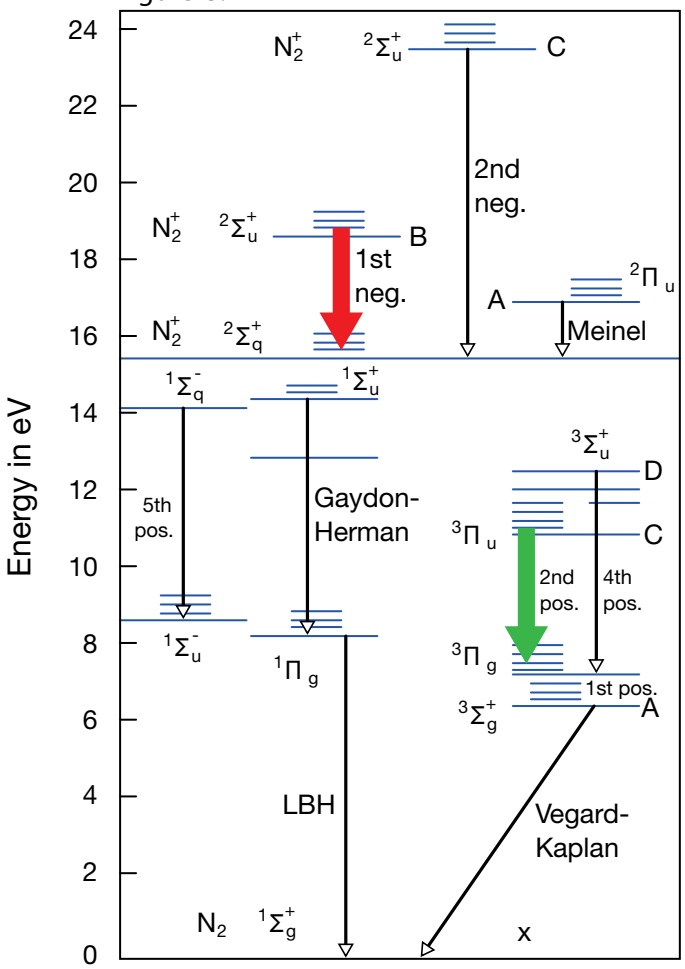

Figure 3.1: Molecular levels of nitrogen N_2 and N_2^+. The colored arrows represent the dominant transitions for fluorescence emission:
Green: 2P $B^2\Sigma_u^+ \rightarrow X^2\Sigma_g^+$
Red: 1N $C^3\Pi_u \rightarrow B^3\Pi_g$
Adapted from [13].

Figure 3.2

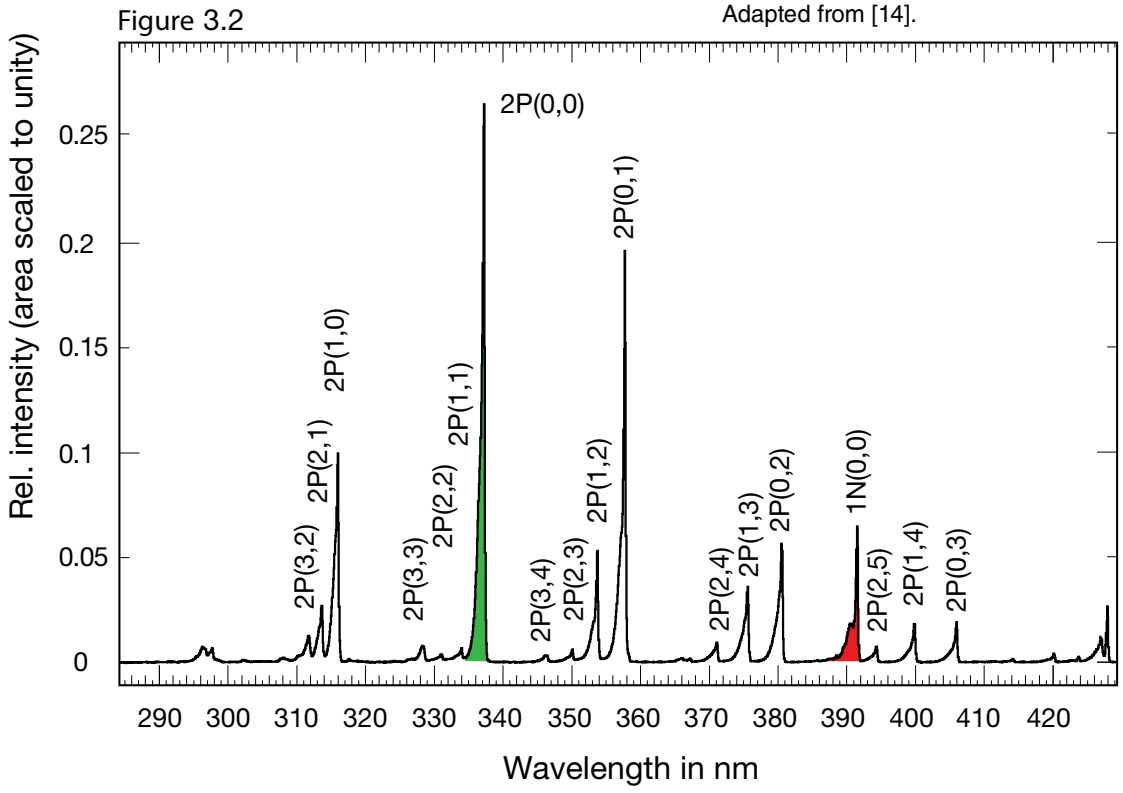

Figure 3.2: Air fluorescence spectrum as a function of the photon wavelength λ excited by 3 MeV electrons at a pressure of 800 hPa as measured by the AIRFLY Collaboration. The colored peaks correspond to the colored transitions shown in figure 3.1. Adapted from [14].

To quantify the amount of fluorescence light, which is emitted in this process, the fluorescence yield is used. Latter is defined in different ways in the literature as the same name is used for slightly different physical quantities. The main difference will be discussed below. The starting point for the fluorescence yield is the fluorescence efficiency [13]

$$\Phi_\lambda = \frac{\text{radiated energy}}{\text{deposited energy}} = \frac{n_\lambda \cdot E_\lambda}{E_{\text{dep}}} \qquad E_{\text{dep}} = n_e \cdot \frac{\mathrm{d}E}{\mathrm{d}X}\,\rho\,\Delta x \tag{10}$$

which is the ratio of radiated energy (with number of photons n_λ) of the nitrogen molecules to deposited energy E_{dep} of n_e shower particles along a path Δx in a gaseous medium of density ρ, which is given by the Bethe-Bloch-formula. This can also be expressed using the time constant for de-excitation via fluorescence emission divided by the sum of time constants for all processes of de-excitation [13]

$$\Phi_\lambda = \frac{\frac{1}{\tau_{\text{FL}}}}{\frac{1}{\tau_0} + \frac{1}{\tau_q}} = \frac{\Phi_\lambda^0}{1 + \frac{p}{p'}} \qquad \Phi_\lambda^0 = \frac{\tau_0}{\tau_{\text{FL}}} \qquad \frac{\tau_0}{\tau_q} = \frac{p}{p'} \tag{11}$$

with the pure fluorescence efficiency Φ_λ^0 without quenching and a reference pressure p', at which the radiative lifetime τ_0 equals the lifetime of collisional deactivation τ_q. By combining equation 10 and 11 and solving for the number of emitted photons n_λ per deposited energy E_{dep}, the fluorescence yield $Y_{E_{\text{dep}}}$ can be expressed as

$$Y_{E_{\text{dep}}}(\lambda, p, T) = \frac{n_\lambda}{E_{\text{dep}}} = \frac{\Phi_\lambda^0 / E_\lambda}{1 + \frac{p}{p'}} \tag{12}$$

Besides this definition of the fluorescence yield $Y_{E_{\text{dep}}}$, a similar definition Y_x is often used in literature, describing emitted photons per path length X of the charged particle. Both definitions are related by

$$Y_x = Y_{E_{\text{dep}}} \cdot \frac{\mathrm{d}E}{\mathrm{d}X}\,\rho \tag{13}$$

The fluorescence yield is typically $Y_{E_{\text{dep}}} \approx 5$ photons / MeV [12] and $Y_x \approx$? photons / m at ground level. Taking into account that the emitted fluorescence photons have to traverse through the atmosphere before being recorded by the telescope, the transmittance of the air τ_{ATM} with additional dependencies on pressure p, temperature T, humidity and wavelength λ has to be considered as well. Furthermore, the detector efficiency $\epsilon_{\text{FD}} \sim 50\%$ [15] has influence on the final photon count, which can be expressed as

$$\frac{\mathrm{d}n_\gamma}{\mathrm{d}X} = \frac{\mathrm{d}E_{\text{dep}}^{\text{tot}}}{\mathrm{d}X} \cdot \int Y_{E_{\text{dep}}}(\lambda, p, T) \cdot \tau_{\text{ATM}}(\lambda, p, X) \cdot \epsilon_{\text{FD}}(\lambda)\,\mathrm{d}\lambda \tag{14}$$

Here, $\mathrm{d}n_\lambda/\mathrm{d}X$ describes the number of detected photons observed per path length. To determine the energy of the primary, the energy deposit per path length has to be integrated over the extent of the shower. Finally, this value has to be corrected due to "invisible" energy which was carried away by other particles than electrons.

3.2 The Pierre Auger fluorescence detector

The largest experiment today with the aim to detect cosmic rays with energies above 10^{18} eV is the Pierre Auger Observatory. It is located in the Argentinian Pampa Amarilla near Malargüe at an altitude of approximately 1350 m and covers over 3000 km^2 of area, as shown in figure 3.3.

Besides the observation of the longitudinal profile of extensive air showers with the fluorescence detector (FD) as described in the previous section, the lateral shower profile is detected by the surface detector (SD), which consists of 1660 water Cherenkov stations arranged in a hexagonal grid with a spacing of 1.5 km [16]. The cooperation of both detectors forms the so called hybrid detection principle. Not all extensive air showers can be detected by both detector systems, as the fluorescence detector is only operational in moonless nights due to its sensitivity to light, while the surface detector has a duty cycle of nearly 100 %.

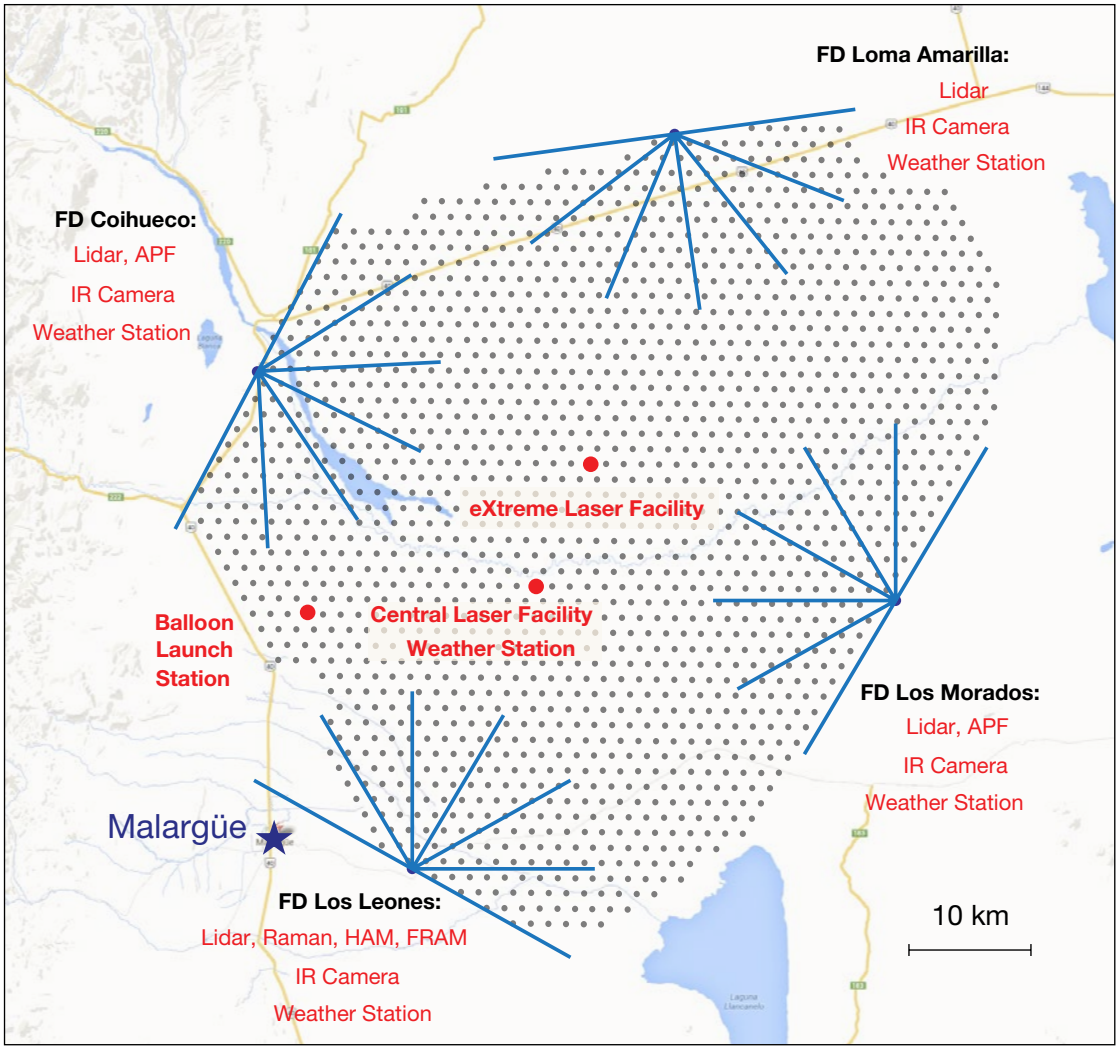

Figure 3.3: Map of the Pierre Auger Observatory (southern site). The black dotted area shows the surface detector while each dot marks the position of one of the 1660 water Cherenkov stations. The blue lines visualise the viewing cone of the fluorescence telescopes that are positioned at the interaction points of the lines. Taken from the Pierre Auger Collaboration and Google Maps.

The fluorescence detector consists of 5 telescope buildings housing a total of 27 fluorescence telescopes, which follow the Schmidt camera design (figure 3.3) [11]. Each telescope has an aperture diameter of 2.2 m and the incoming light is collected by a 3.8 x 3.8 m^2 segmented spherical mirror with a radius of curvature of R = 3.4 m which is composed by 37 tiles (figure 3.4). The reflected light is detected by a hyperbolically curved matrix of 22 x 20 = 440 photomultiplier tubes (PMTs), which are placed between mirror and aperture. The aperture is equipped with Schott M-UG6 UV filter glass absorbing visible light and a Schmidt corrector ring to enhance the optical performance of the telescope by reducing spherical and coma aberration of the mirror (see section 4.1.3.1 and section 4.1.3.2). One of these fluorescence telescopes has a field of view of 30° in azimuth and 28.1° in altitude, corresponding to the differing horizontal and vertical pixel count of the PMT camera.

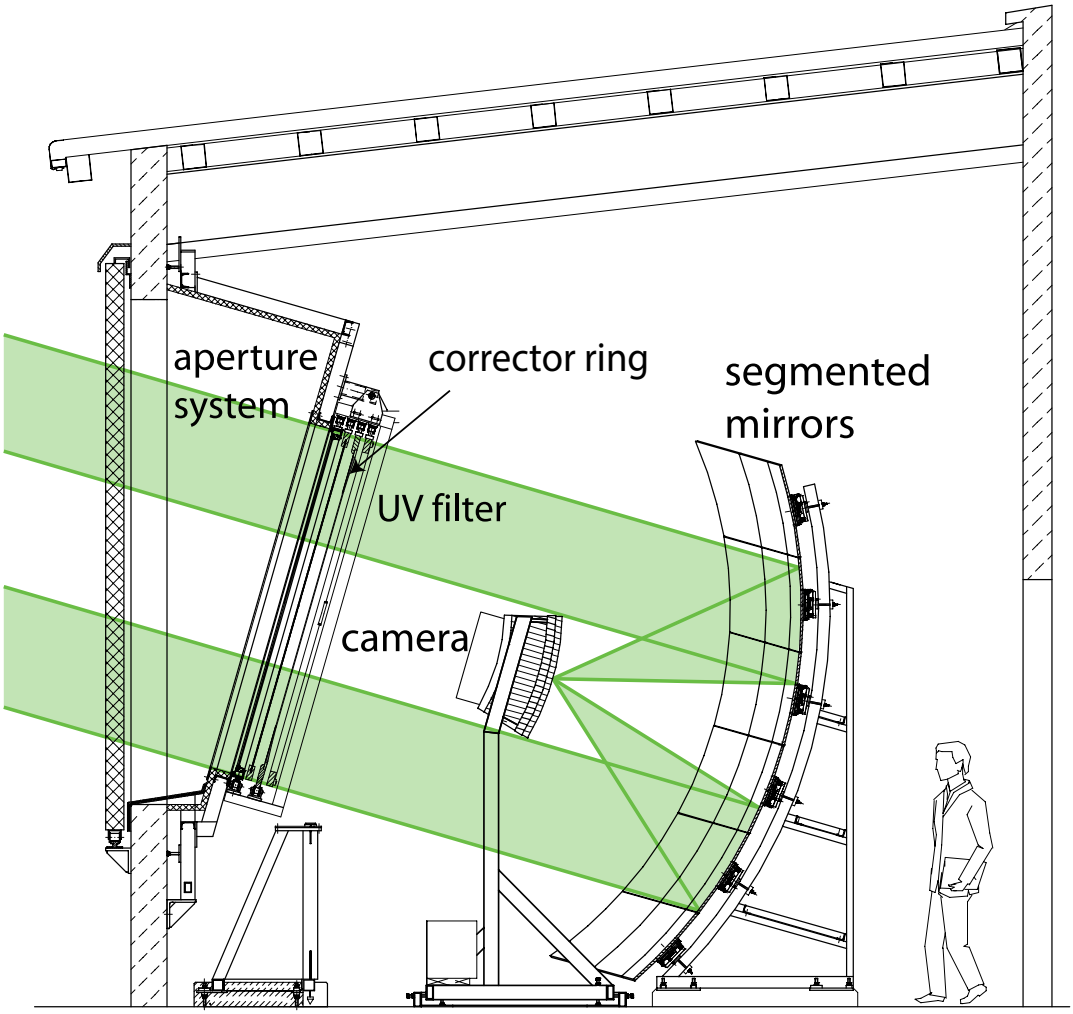

Figure 3.4: Schematic of an Auger fluorescence telescope. The fluorescence light is reflected onto a curved matrix of photomultiplier tubes after it passes a UV filter. The mirror is obstructed by the camera which is the main disadvantage of the Schmidt camera optical layout. Taken from [11] and modified.

3.3 FAMOUS

For the measurement of fluorescence light emitted by an extensive air shower, a detector which is highly sensitive to UV photons has to be used. The most popular device for this task is the photomultiplier tube (PMT). Many experiments take advantage of the high photon detection efficiency (PDE) of about 30-35 % in the UV range [17]. However, a relatively new semiconductor light sensor, known as silicon photomultiplier tube (SiPM), has the potential to be more effective than PMTs while offering a series of additional advantages.

Figure 3.5: Picture of the seven pixel prototype of FAMOUS, built at the III. Physikalisches Institute A of the RWTH Aachen, which is called FAMOUS SEVEN. A Fresnel lens is mounted at the front of the telescope tubus which is attached rotatably in all directions. Photo by Tim Niggemann.

The prototype fluorescence telescope FAMOUS ("First Auger Multi pixel photon counter camera for the Observation of Ultra-high-energy cosmic ray air Showers") (figure 3.5), which is built at the III. Physikalisches Institut A, RWTH Aachen, is a feasibility study with the aim to show that SiPMs are well suited for the observation of extensive air showers. As discussed in [18], a refractive optical design was chosen using a Fresnel lens of d = 549.7 mm diameter and f = 502.1 mm focal length, which leads to a focal number of $N_f = f / d$ = 0.913. As the thickness of a conventional lens with the above listed properties would lead to the absorbtion of most of the fluorescence light, the usage of a Fresnel lens made of UV transparent PMMA is necessary. Thus, the installed lens has a thickness of only 2 mm. An additional advantage is the reduced weight of around 3 % compared to the bulky counterpart of the Fresnel lens made from the same material.

The focal plane of the telescope consists of 64 pixels, each with a field of view of 1.5°. The active part of each pixel, which will detect the light, is a SiPM, which is placed behind a Winston cone. The construction is shown in figure 3.6. The Winston cones are useful to enhance the signal to noise ratio of the SiPMs as more light will be collected to illuminate their small surface, a square of 6 x 6 mm². With the help of the Winston cones, the sensitive surface is enlarged to a circular aperture of 13.4 mm diameter. The total field of view of the fluorescence telescope amounts to 12°.

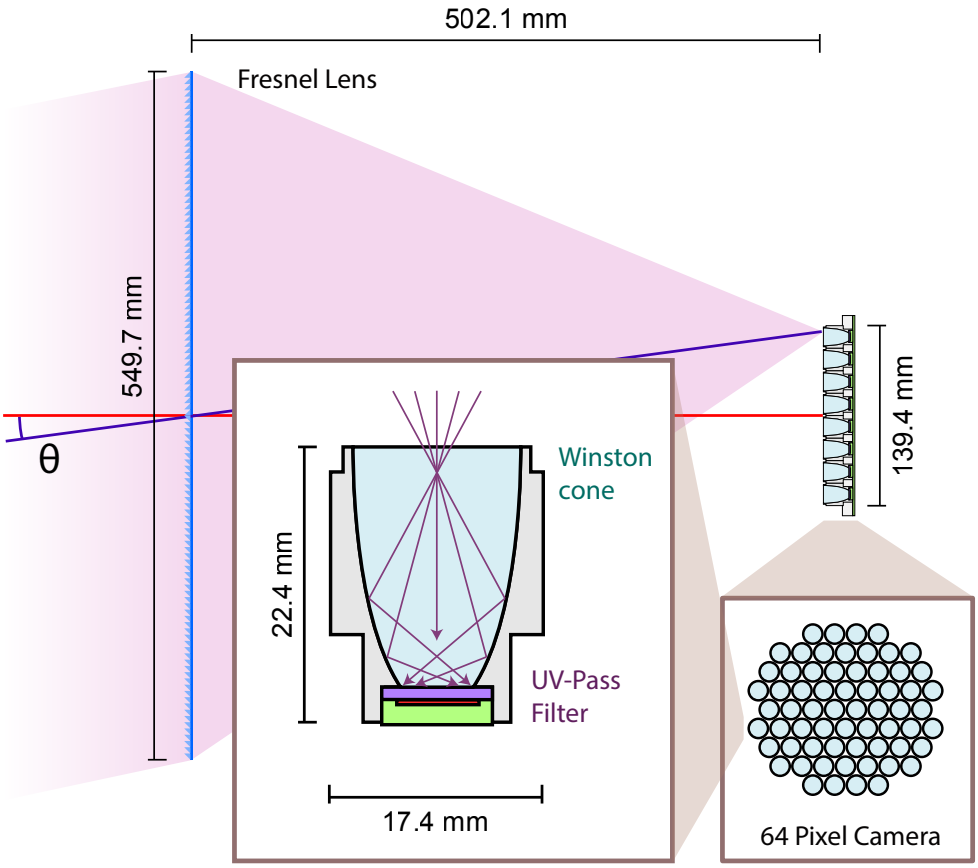

Figure 3.6: Refractive optical design of FAMOUS adapted from [19]. Each of the 64 pixels consists of a SiPM and a UV-pass filter placed at the end of a Winston cone with a field of view of 1.5°. The total field of view of the telescope sums up to θ = 12°.

Two SiPM types, which are mainly identical to the ones installed in a smaller test version of the planned telescope, are characterised in [20]. For the measurement of extensive air showers, the dynamic range of SiPMs has to be studied, as well as several noise phenomena known as thermal noise, crosstalk and afterpulsing. The benefits of SiPMs not only include the potential to offer a higher PDE compared to PMTs, they can also be operated at relatively low voltages below 100 V. Also important for the usage in a fluorescence telescope is the robustness of SiPMs against high light intensities, for example moon light.

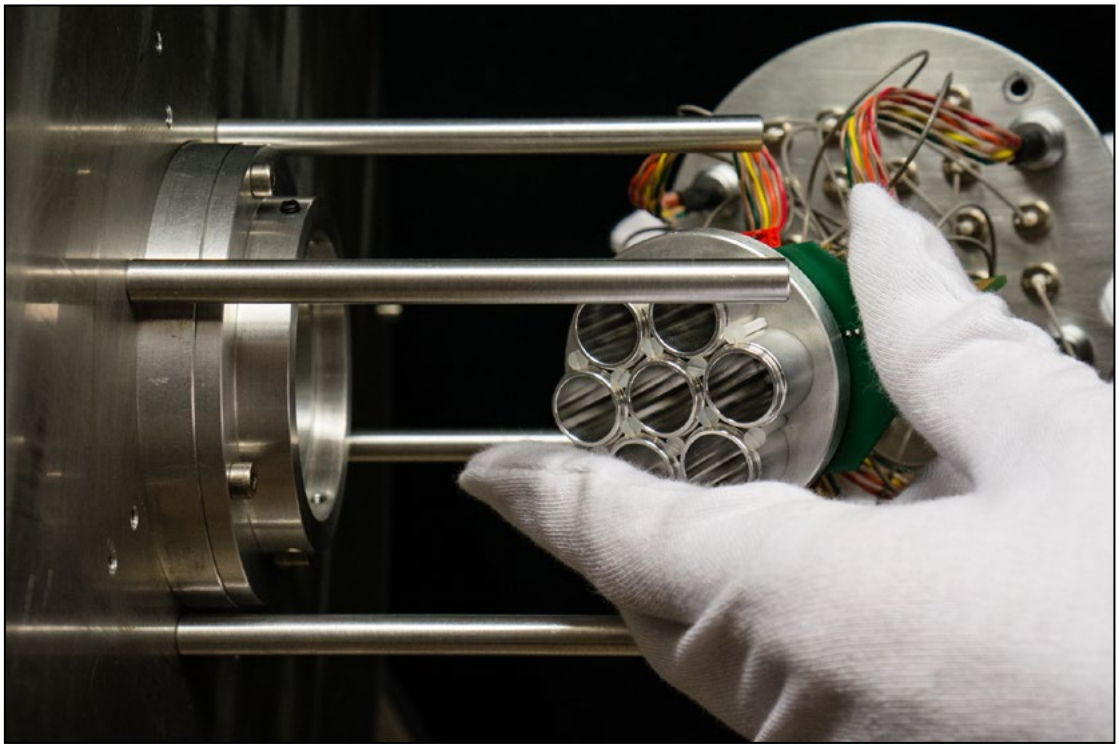

Figure 3.7: Picture of the seven-pixel-focal-plane of FAMOUS SEVEN including readout electronics for the SiPMs. The seven Winston cones are directly visible. Photo by Tim Niggemann.

FAMOUS SEVEN (see figure 3.7) is a seven pixel prototype of FAMOUS, which was constructed to perform first test series with the telescope, being able to study the cooperation of all components used. Also, the brightness of the night sky has to be understood very well as it has a large impact on the operational capability of fluorescence telescopes. The night sky brightness is a continuous background photon flux contaminating the fluorescence light signal of the extensive air showers. An analysis of the local night sky brightness is presented in [19].

Based on the night sky background and additional noise phenomena of the SiPM pixels, a minimum signal to noise ratio can be defined as a threshold to trigger extensive air showers. A simulation of the trigger probability of FAMOUS as a function of the shower core distance and shower energy is presented in figure 3.8. An extensive air shower with an energy of 10^{18} eV can be recorded with almost 100% detector efficiency in a distance of up to 7 km.

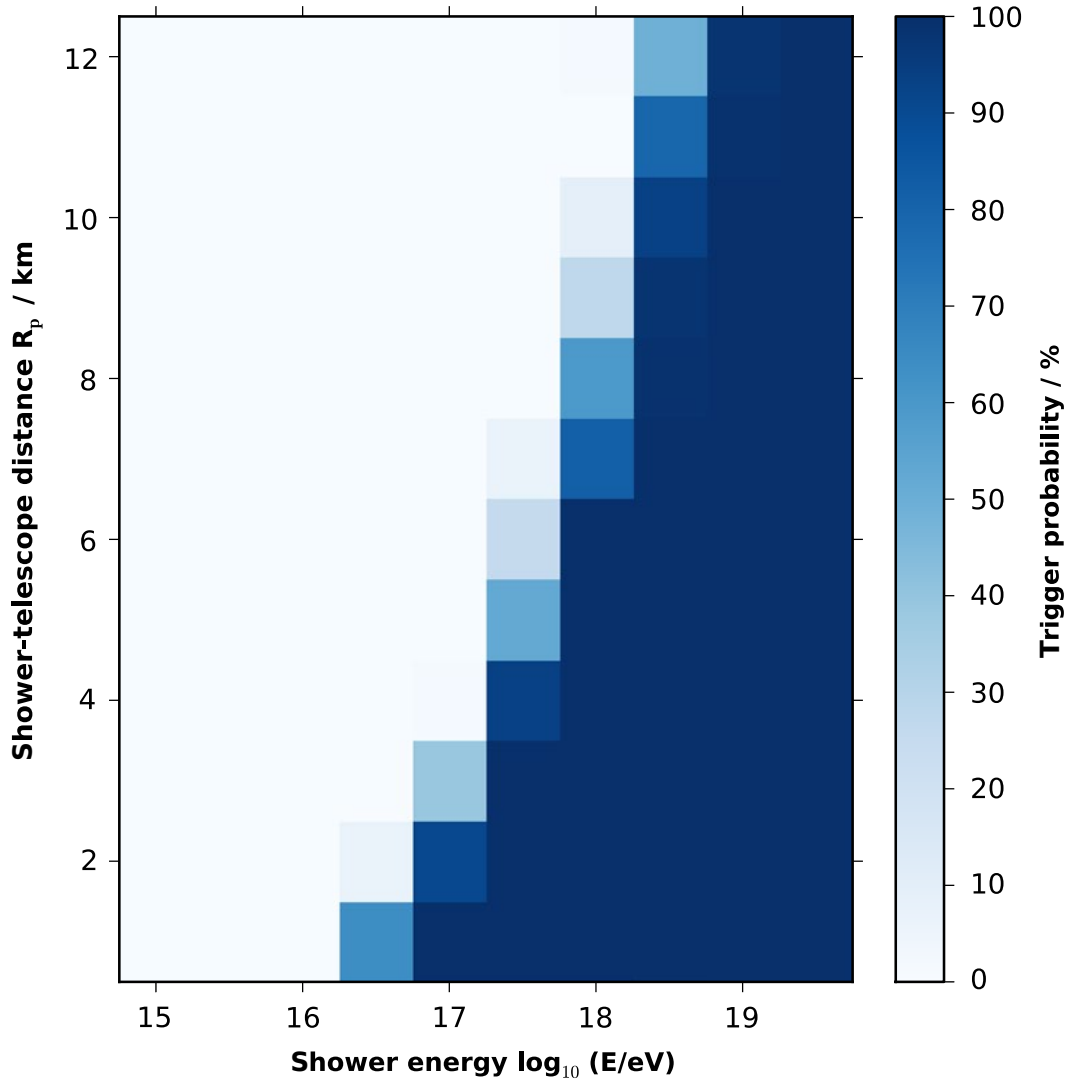

Figure 3.8: Simulated trigger probability of FAMOUS as function of the shower-telescope distance in km and the energy of vertical showers (zenith angle θ = 0°) [21].

Besides the above listed benefits on using a Fresnel lens as optical component, it suffers mostly from relatively poor imaging performance, which will be analysed and quantified in this thesis. Possible future applications of the FAMOUS technology using Fresnel optics in cooperation with a SiPM focal plane are evaluated by simulations in [22].

4 Introduction to lenses and Fresnel lenses

According to today's level of knowledge, the first lenses were made several centuries before Christ. As the treatment and processing of glass was not advanced enough at that time, a glass sphere filled with water was used instead to converge light [23]. The first glass lenses were manufactured in the middle ages. In the early 17. century, Galileo Galilei and Johannes Kepler greatly improved the first telescope designs that used refractive optics, whereas Hans Lippershey, a German-Dutch lens maker, is the earliest person documented to have applied for a patent for such a device [24].

Since then, many forms and types of lenses for a wide range of applications have been developed. In modern optics, it is even possible to produce lenses that exhaust theoretical limits of light. This is called diffraction limit.

Mainly for the use in lighthouses, the Fresnel lens was developed by the French physicist Augustin Jean Fresnel in 1822. With the new technology equipped, the light could easily be observed at distances of 30 km and beyond [25]. Today, Fresnel lenses are used for optical systems with low demand for image quality, for example as collimator in overhead projectors, or if weight is an important criterium. In the following, general properties and effects of lenses will be presented. Additionally, the peculiarities of Fresnel lenses will be discussed in detail.

4.1 Conventional lenses

To understand the special characteristics of a Fresnel lens, conventional lenses have to be examined first. The first possible classification of simple lenses is made by the type of curvature of the two optical surfaces, the light will pass (cf. figure 4.1). While theoretically, each of these lenses can be used in both orientations (light coming from the left side and light coming from the right side), the optimal usage of a lens depends on application situation. A lens produces less spherical aberration (see section 4.1.3.1), if the angle of incidence Φ (cf. figure 4.9 in section 4.1.3) of the light (in particular marginal rays) on both optical surfaces is small. In case of focussing a collimated beam of light, a plano convex lens is the best choice with the curved surface facing towards the incoming light.

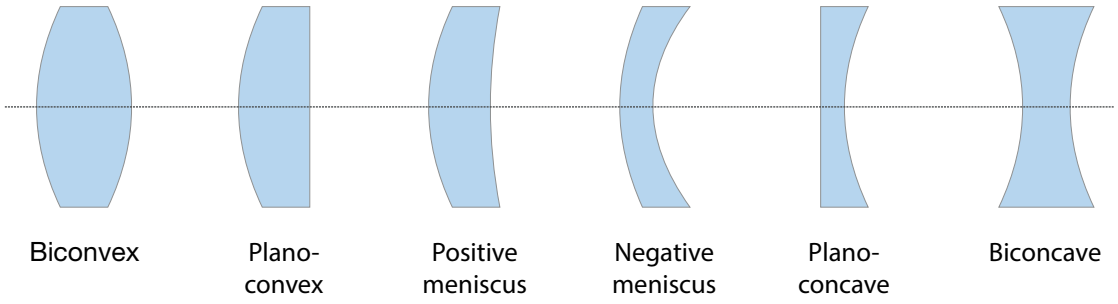

Figure 4.1: Different types of lenses categorised by the form of both optical surfaces.

Each category is further subdivided into spherical and aspherical lenses. The former is characterised by the special parameterisation of its surfaces, both being part of a sphere, while the surfaces of aspheric lenses in most cases follow optimised parameterisations to correct monochromatic aberrations. Another way to correct aberration is the usage of compound lenses, i.e. an array of simple lenses with a common axis. As both methods lead to the same result, one aspherical lens can achieve the optical performance of a system consisting of 3 ~ 4 spherical lenses [26]. Nevertheless, the use of compound lenses is often preferred for financial reasons if space and weight is not a limiting factor.

The lens surface is rotationally symmetric with respect to the optical axis, thus the aspheric profile of a lens can be parameterised using the sagitta function with cylindrical coordinates [26]:

$$z(\rho) = \frac{\frac{\rho^2}{R}}{1+\sqrt{1-(1+k)\,\frac{\rho^2}{R^2}}} + \sum_i C_i\,\rho^{2+2i} \tag{15}$$

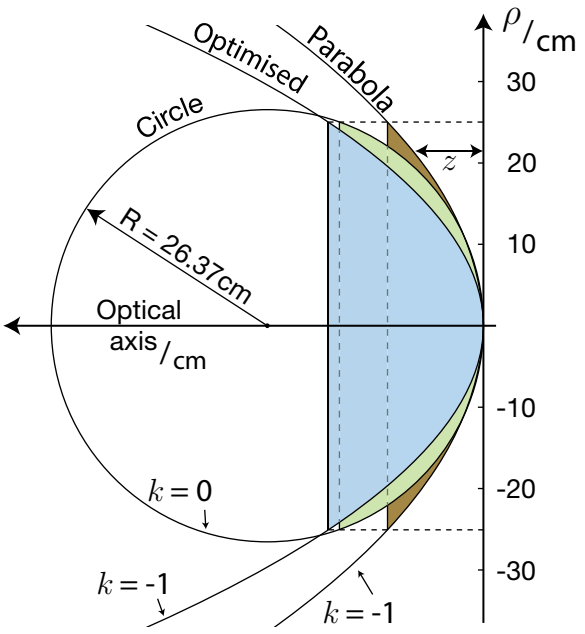

Figure 4.2: Construction of a lens surface with cylindrical coordinates. Three different profiles with the same radius of curvature R were used: green spherical, brown parabola and blue parabola including aspherical deformation constants C_i which were optimised for the fluorescence telescope FAMOUS.

Here, z describes the thickness of the lens along the optical axis, ρ describes the axial radius perpendicular to the optical axis, R denotes the bending radius of curvature and k is the conic constant.

The coefficients C_i are aspherical deformation constants that represent a perturbation to the conic surface profile. Possible surface profiles depending on the conic constant without aspherical perturbation result from the intersection of a conical surface and a plane, illustrated in figure 4.3.

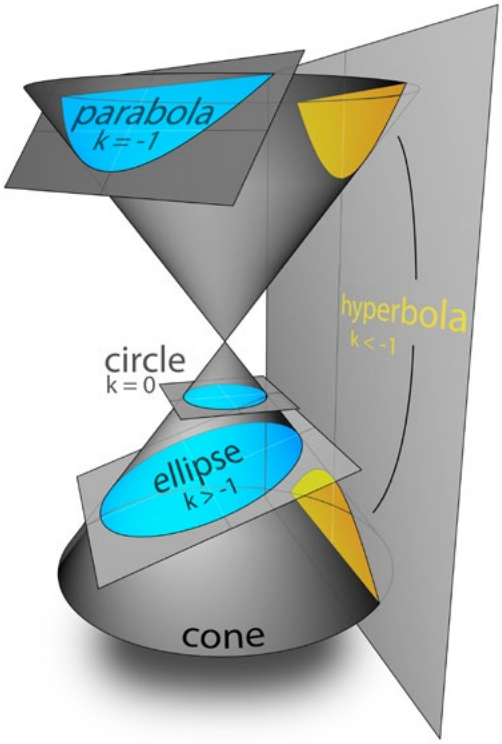

Figure 4.3: Conic sections are formed by the intersection of a cone surface and various planes. In blue: parabola, circle and ellipse, in yellow: hyperbola.

Constant	Value
C_1	$1.18 \cdot 10^{-4}$ m^{-1}
C_2	$1.34 \cdot 10^{-9}$ m^{-3}
C_3	$9.52 \cdot 10^{-15}$ m^{-5}
C_4	$-2.04 \cdot 10^{-19}$ m^{-7}

Table 2: Deformation constants of the lens surface profile for the fluorescence telescope FAMOUS. Taken from [18].

For the fluorescence telescope FAMOUS, an optimal set of parameters was obtained by using the commercial optics design software Zemax [18]. The optimisation process in this software is based on the minimisation of a definable "merit-function", which consists of operands representing individual qualities of the optical system, which needs to be optimised. Each operand holds a "target" and a "weight", which give the ability to set a desired value, and the corresponding relative importance for that quality in comparison to the other attributes of the system. This feature is necessary for the optimisation of optical systems, as the only perfect optical device is a plane mirror. All other optical components and systems have to be optimised for the individual operating range. The optimised lens profile for FAMOUS, which describes the conventional, i.e. "bulky" counterpart to the desired Fresnel lens, is shown in figure 4.2 in comparison to a parabola and a spherical profile with the same radius of curvature. The deformation constants are listed in table 2.

Since the production of a Fresnel lens with an individual aspherical surface profile is rather expensive, a similar prefabricated Fresnel lens was used for the studies in this thesis.

4.1.1 Point spread function

One of the most important quality criteria for imaging performance is the image resolution. In case of a lens, the image resolution quantifies how close two point like objects can be to each other and still be differentiated on the image plane. This is closely related to the point spread function (PSF), which is the intensity distribution on the image plane of the focal point of the lens.

The point spread function is a measure for the ability of the lens to focus light on a single point which also depends on the application situation, leading to different aberration effects, discussed in section 4.1.3. The influence of the point spread function on the process of image formation is explained in the following section.

In a more general approach, the PSF is the two-dimensional response function of a focussed optical system. In this approach, the lens in combination with the image plane is a dynamic system, that gives a characteristic response to an input signal, which is the light - reflected or emitted - by an object, for example the fluorescence light of an extensive air shower. To study the characteristic response, a preferably simple input signal (an impulse) is presented to the system [27]. In general, the choice of an appropriate impulse is not trivial and depends on the nature of the system.

In the case of non-coherent linear imaging optics, with the aim to reproduce an object plane on an image plane (see figure 4.4), the formation process of an image follows the superposition principle, which is due to the non-interacting property of photons and can be described by linear system theory [27]:

$$\text{Image}\ (\text{Object}_1 + \text{Object}_2) = \text{Image}\ (\text{Object}_1) + \text{Image}\ (\text{Object}_2) \quad (16)$$

For this reason, the object plane $O(x,y)$ can be subdivided into infinitesimal portions at locations (x_0, y_0), i.e. many individual objects (figure 4.4) performing a convolution with a two-dimensional Dirac delta function:

$$O(x_0, y_0) = \iint O(x, y)\ \delta(x_0 - x, y_0 - y)\ \mathrm{d}x\,\mathrm{d}y \quad (17)$$

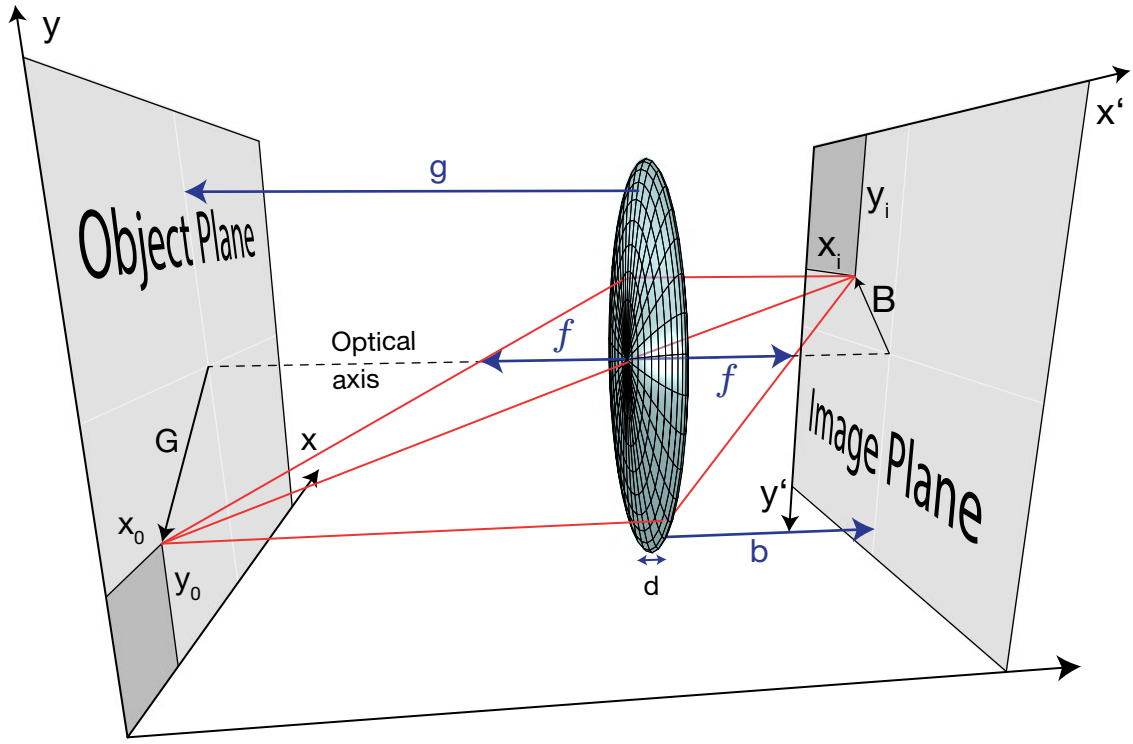

Figure 4.4: Image formation of a refractive optical system. The object plane can be subdivided into individual points with coordinates (x_0 , y_0), which are translated to the image plane with distance from lens to object plane and lens to image plane of g and b, respectively, and the focal length f, which is identical on both sides of the lens. The distance of a point on the object plane from the optical axis is denoted as G while the distance from the optical axis to the transferred point is denoted as B. The coordinate system of the image plane is reversed from the object plane coordinate system.

The coordinates of each point of the object plane can then be translated into coordinates on the image plane (figure 4.4) with the knowledge of the focal length f of the used lens and a given object distance g, contained in the magnification M for a focussed system:

$$M(f,g) = \frac{f}{f-g} \tag{18}$$

Each point of the object plane $O(x_0,y_0)$ is individually mapped on the image plane, including the response of the lens, the PSF. As a result, a characteristic blur is added to each image point, overlapping with nearby image points (figure 4.5). The total resulting image $I(x_i,y_i)$ is formed by the superposition of the images from all object points [27]:

$$I(x_i,y_i) = \iint O(x,y)\ PSF(x - x_i/M, y - y_i/M)\ \mathrm{d}x\,\mathrm{d}y \tag{19}$$

Figure 4.5: Graphical representation of equation 19: The image is formed by convolution of the original picture of the object and the PSF of the optical system. The PSF is the image of a point light source.

The magnification M needs to be included to translate between the coordinates of the object plane and the image plane. Precisely, the total image can be expressed as the weighting function of the object plane, convoluted with the impulse response function, which is the image of the Dirac function. The Dirac function is the mathematical analogon to a point light source.

4.1.2 Diffraction limit

The size of a focal point is mainly influenced by geometrical imperfections of the surface of a lens. While uncorrected lenses suffer from several aberration effects, the imaging performance of modern aspheric corrected lenses is limited only due to the diffraction of light. This is one of few directly visible consequences of quantum mechanics and was the inspiration for Heisenberg's quantum uncertainty principle [28]. An optical system, with an angular resolution that is limited by diffraction effects is called diffraction limited.

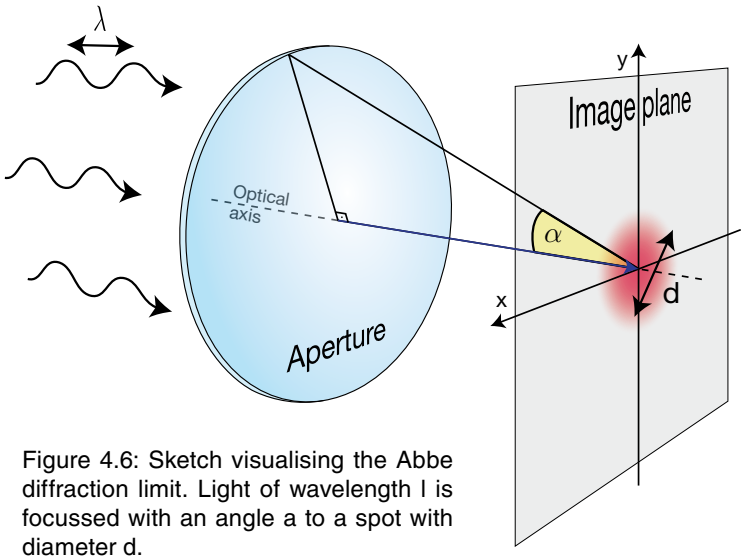

Figure 4.6: Sketch visualising the Abbe diffraction limit. Light of wavelength l is focussed with an angle a to a spot with diameter d.

The minimum spot size d of light with wavelength λ, focussed with an angle α, in a medium with refractive index n is given by the Abbe diffraction limit (cf. figure 4.6):

$$d = \frac{\lambda}{2n\sin(\alpha)} \approx \frac{\lambda}{2} \tag{20}$$

The point spread function for such a system with circular aperture and infinitely distant point light source is known as Airy pattern [29],

$$I(\beta) = I_0 \left(\frac{2J_1(x)}{x} \right)^2 \tag{21}$$

which is shown in figure 4.7. It is a special case of the more general Fraunhofer diffraction pattern. Here $J_1(x)$ is the Bessel function of the first kind of order one and x is a dimensionless variable which contains not only the radius a of the aperture, i.e. the lens, and the wavenumber $k = 2\pi/\lambda$ of the light, but also includes the incident angle β of

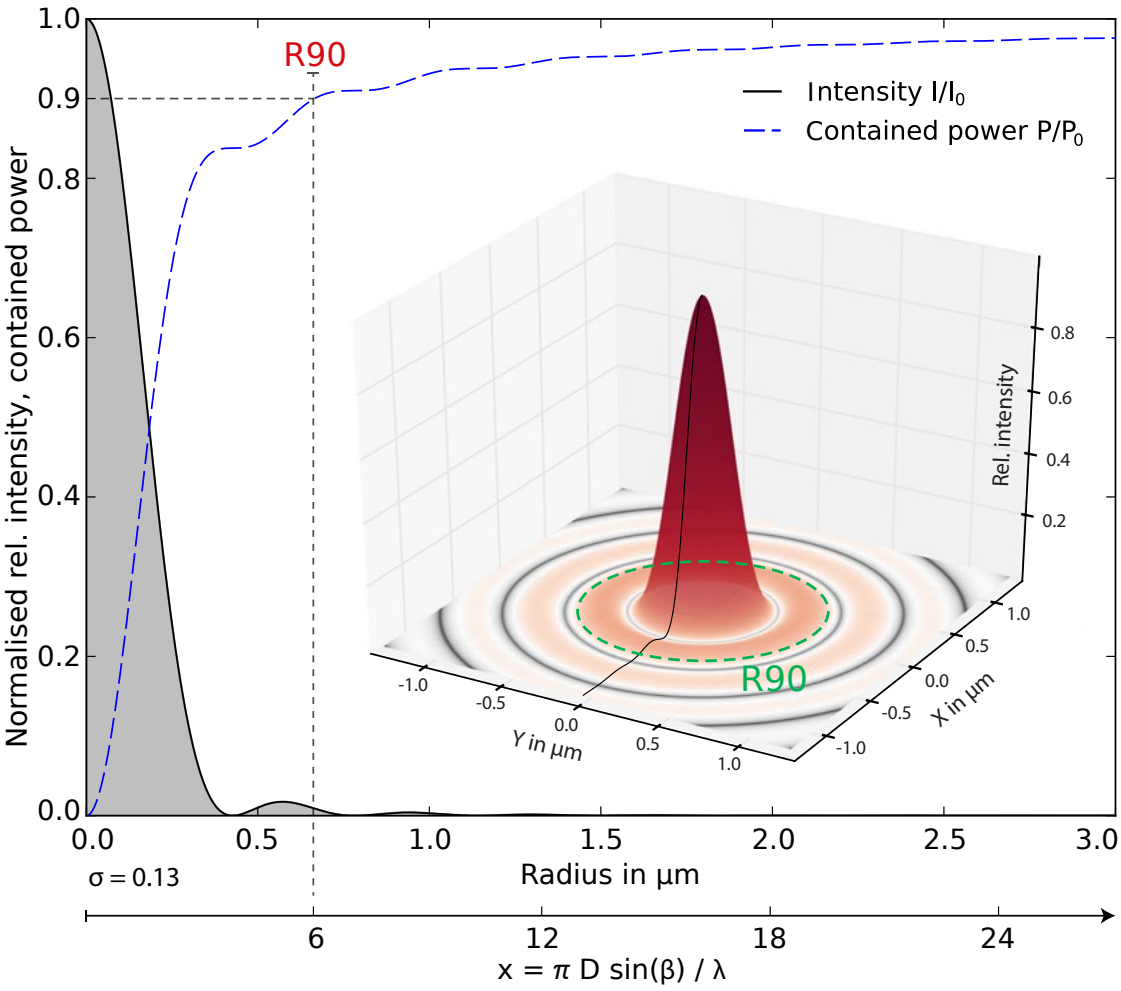

Figure 4.7: Airy pattern on the image plane for a circular aperture with D = 2a = 549.7 mm diameter, focal length f = 502.1 mm and light with λ = 350 nm wavelength. The grey plot represents the relative intensity distribution as a function of radius using the dimensionless variable x = πD sin(β) / λ and for comparison the radius is also plotted in µm. The dashed blue line denotes the integrated encircled energy as a function of the radius. The black dashed line resp. green dashed circle in the equivalent 3d surface plot marks the aberration radius R90 of 90 % encircled energy at r = 0.67 µm.

the light rays on the image plane, illustrated in figure 4.8. For small angles β, x can be approximated with the distance r to the optical axis in the image plane:

$$x = ka \sin(\beta) \approx \frac{\pi D}{\lambda} \cdot \frac{r}{f} = \frac{\pi r}{\lambda N} \tag{22}$$

In the center of the Airy pattern, a blurry spot is formed, also named Airy disk or circle of least confusion with a maximum intensity I_0, surrounded by altering dark and bright rings caused by constructive and destructive interference. In figure 4.7, the Airy pattern is plotted as a function of x but also as a function of r for the aperture parameters describing the "bulky" counterpart of the Fresnel lens of FAMOUS.

A significant value for the size of the Airy pattern is the radius of a centered circle on the image plane, which encircles a certain portion of the total integrated intensity. In figure 4.7, the radius for 90% encircled energy is shown. It is referred to as R90 (see section 4.2.5) and is also used to describe the size of the point spread functions measured for the Fresnel lens in chapter 8. Note that the peripheral rings contain a significant portion of the total intensity, while radial intensity tends against zero. This is due to the encircled area, which increases with the square of the radius. Not only theoretically but also practically, the point spread function will never drop to absolute zero in its intensity rings even for infinite distance to the center of the spot.

An alternative method to determine the size of the point spread function is a Gaussian fit to the pattern. The size is then given by the width of the Gaussian function $\sigma = 0.42 \lambda N = 0.13$ µm in case of the the Airy pattern. The width σ is a factor of 5 smaller than the aberration radius R90 = 0.67 µm.

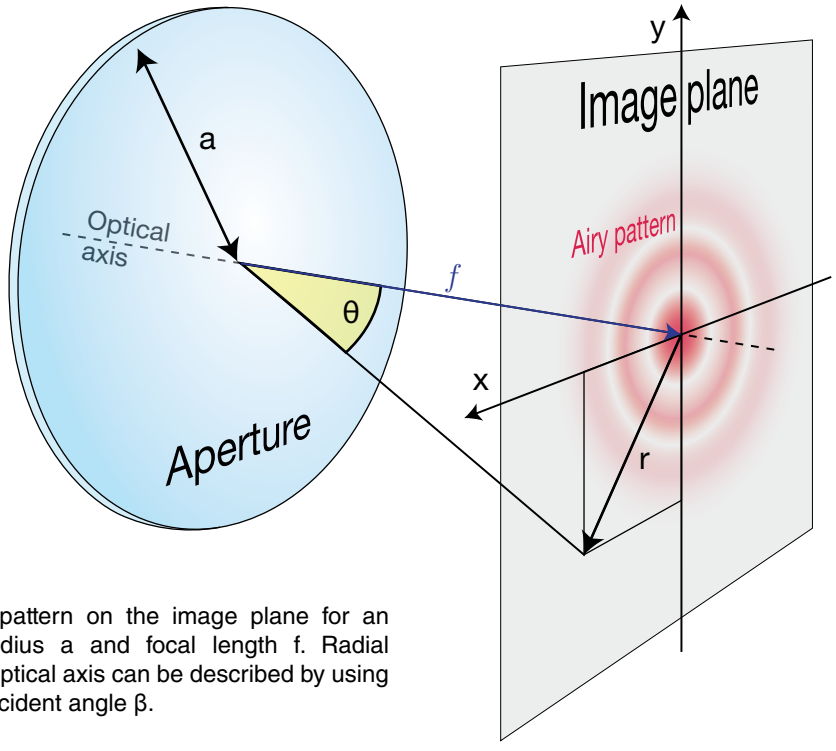

Figure 4.8: Airy pattern on the image plane for an aperture with radius a and focal length f. Radial distances to the optical axis can be described by using radius r and by incident angle β.

4.1.3 Aberrational effects

Apart from the theoretical limit on focussing light, which is given by diffraction, a series of other optical effects can cause a reduction of the imaging performance which are known as “intrinsic aberrations”. Additionally, a perfect alignment of all optical components is not possible in reality, resulting in further “externally induced aberration”. All effects, which deteriorate the image have to be incorporated in the detector response simulation and can be observed as a special pattern or dependency of the PSF, which can be explained due to deviations from spherical geometry of the shape of the wave front which is formed by the lens (figure 4.9).

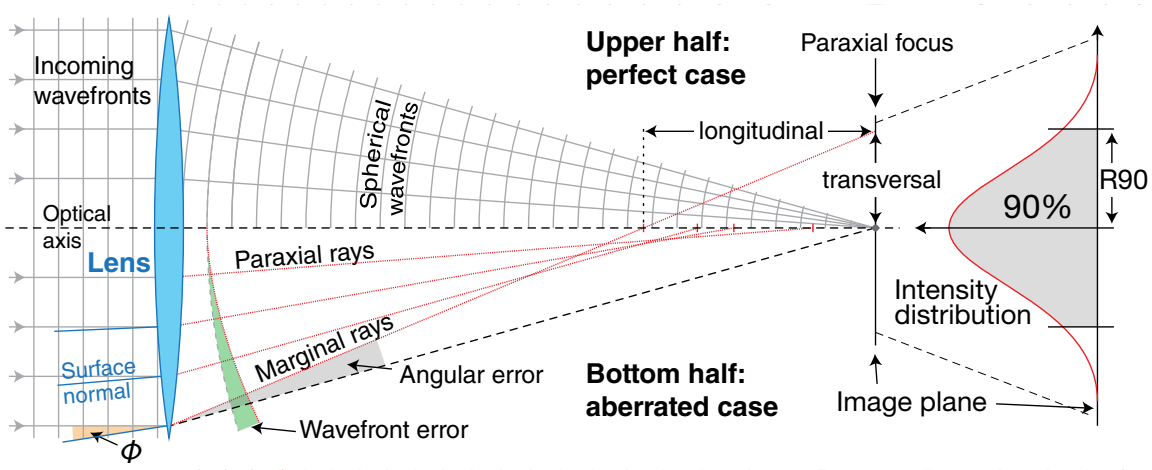

Figure 4.9: Spherical wavefronts formed by a perfect lens (top) and (spherical) aberrated wavefronts of an imperfect lens (bottom). The wavefront error describes the deviation of the refracted wavefront from a spherical surface. The aberrated rays intersect at different longitudinal distances along the optical axis as well as transversal distances in the focal plane. The resulting intensity distribution on the image plane for the aberrated case is described by the point spread function and its radial size characterised by the aberration radius R90. The angle between lens surface normal and parallel incoming light is marked as Φ.

The standard lensmaker’s equation, connecting the surface curvature of the lens with the focal distance is based on the series expansion of the sines in Snell’s law [27]:

$$n \cdot \sin(\phi) = n' \cdot \sin(\phi') \quad \rightarrow \quad n \cdot \phi = n' \cdot \phi' \tag{23}$$

with the angle of incidence Φ and refraction Φ’ of light passing through a boundary of different isotropic media with refractive indices n and n’. The replacement of the sines is also called paraxial or Gaussian approximation, as it is only valid for rays, which are close to the optical axis, called paraxial rays (figure 4.9). This approximation leads to a quick and practical way to determine paraxial focus, but does not provide any information on aberrations, while the Seidel approximation also includes the second term in the sine series expansion:

$$\sin(\phi) = \phi - \frac{\phi^3}{3!} \Big| + \frac{\phi^5}{5!} - \frac{\phi^7}{7!} + \ldots \tag{24}$$

which can be used to describe primary or third order aberrations like spherical aberration, coma, astigmatism and field curvature. In the following, the different aberrational effects for conventional lenses will be presented, to understand their impact on the PSF.

4.1.3.1 Spherical aberration

Spherical aberration describes the effect, that incident rays closer to the edge of a lens (marginal rays) are bent too strong in comparison to rays passing the center (figure 4.9), resulting in different crossover points along the optical axis. This effect appears for spherical lens surfaces, as those do not form spherical wave fronts. The longitudinal aberration is given by the distance between the focal point for paraxial rays and for peripheral rays, also called marginal focus. The best focus locates right between paraxial and marginal focus.

4.1.3.2 Coma aberration

This aberration affects off-axis image points. For these, incoming wavefronts are tilted with regard to the optical axis. The resulting wavefront aberration after refraction is shown in figure 4.10 on the bottom left, which forms a comet like blur on the image plane. At point F_b, the maximum intensity is located, while the Gaussian image point is located at point B. The coma blur is created by progressively expanding circles along the axis of aberration a. Inner circles coincide with the paraxial focus, while the biggest circles are formed by the edge of the lens.

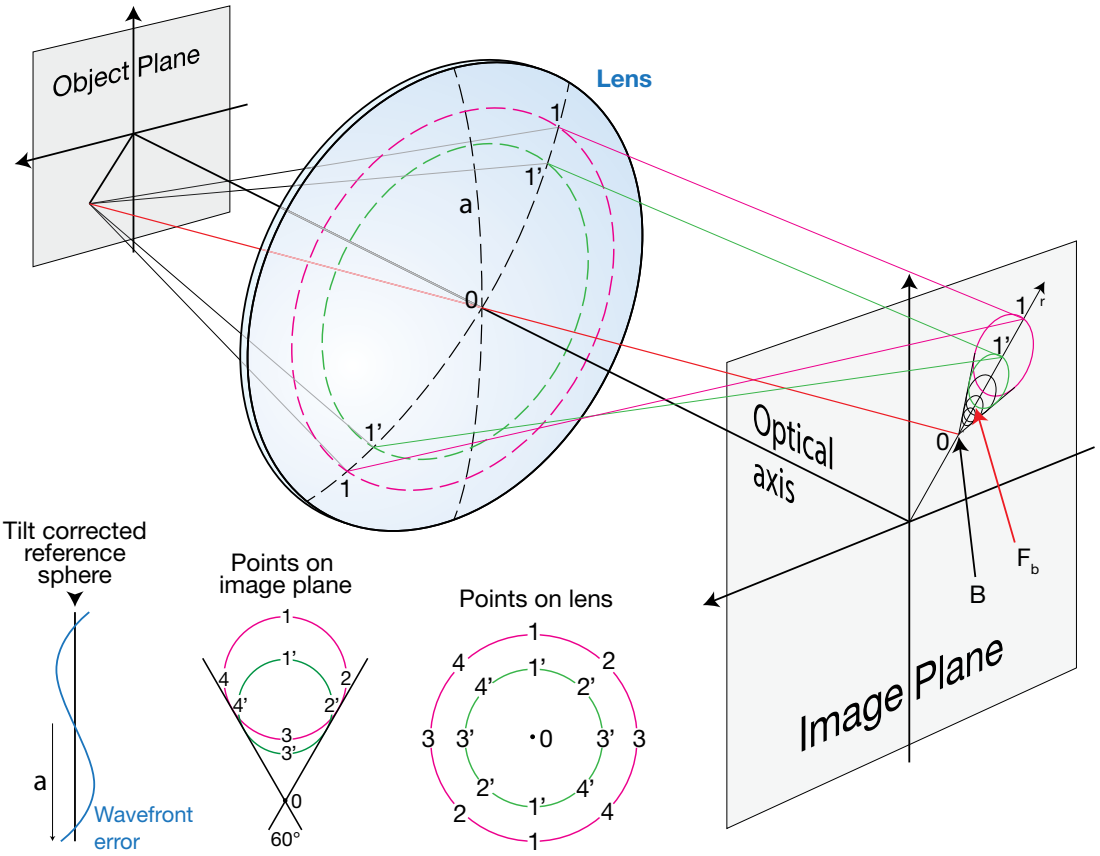

Figure 4.10: Sketch of the geometrical construction of comatic aberration. Different points of two circles on the lens are numbered and their contribution to the comatic blur on the image plane is illustrated. A cross section of the wavefront error in comparison to the tilt corrected reference sphere is also shown on the bottom left. Inspired by [27].

4.1.3.3 Astigmatism

As coma aberration, astigmatism is also caused by inclined incident wavefronts. To understand this effect two imaginary planes have to be introduced: the tangential plane is defined by the central ray and the optical axis, whereas the sagittal plane is orthogonal to it and includes the central ray, as shown in figure 4.11. Due to the incident angle, the projection of the incoming wavefront on the lens surface forms an ellipse. Since the focal length depends on aperture diameter, which for the ellipse is smallest at the intersection with the tangential plane, and largest for the intersection with the sagittal plane, the two orthogonal wavefront sections focus at longitudinal separation. The circle of least confusion is located between the two focal points T and S (figure 4.11).

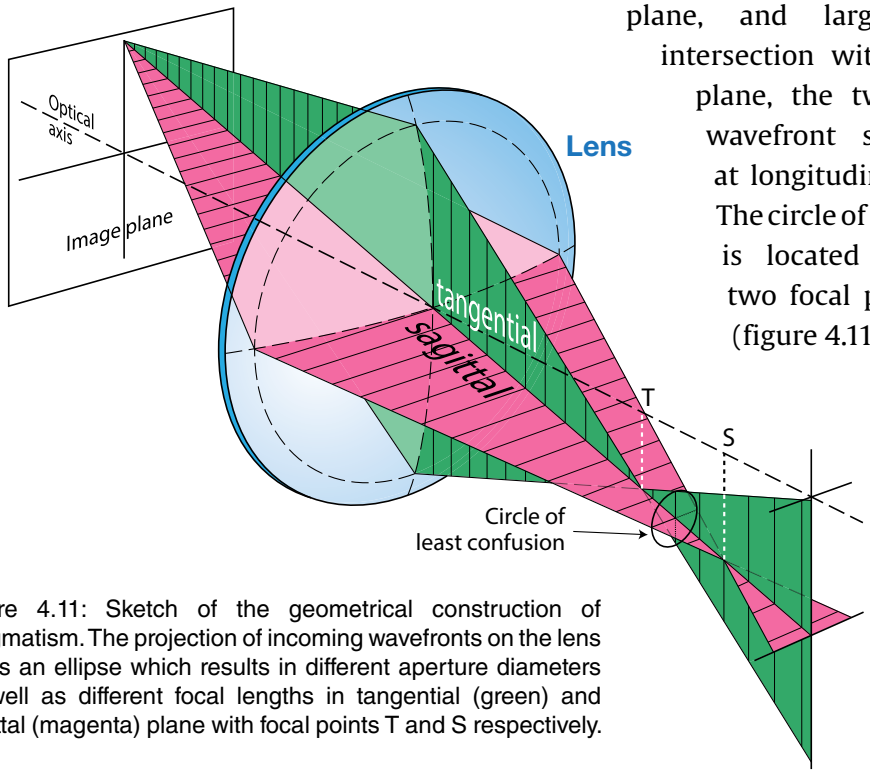

Figure 4.11: Sketch of the geometrical construction of astigmatism. The projection of incoming wavefronts on the lens forms an ellipse which results in different aperture diameters as well as different focal lengths in tangential (green) and sagittal (magenta) plane with focal points T and S respectively.

4.1.3.4 Petzval field curvature

For most of the technical and practical applications, every point imaged by a lens should ideally be contained in the focal plane, containing a flat sensor to process the total image. In fact, the image of a lens is formed over a parabolic curved surface, described by a term called Petzval contribution PC, which is the distance from the flat to the curved image plane (figure 4.12):

$$PC = \frac{\theta^2 f}{2n} \approx \frac{x^2}{2nf} \tag{25}$$

with angle of incidence θ, focal length f and index of refraction n of the lens. Nature solved that problem by developing the eyeball, simply fitting the retina to the curvature needed. As most small camera sensors can not be bent, this aberration has to be corrected by lens systems.

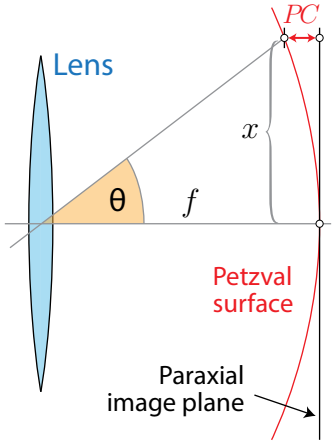

Figure 4.12: The image of a simple lens is formed over a curved surface, the Petzval surface.

4.2 Fresnel lens

4.2.1 Basic concept

A conventional lens of large diameter and high refraction power becomes relatively bulky and can contain several kilograms of material. However, crucial for the light refraction is only the relative angle of the two active surfaces of a lens. The idea of a Fresnel lens is to divide the lens into a set of concentric annular sections called “grooves” and save as much material as possible while the curvature of the active surfaces remains unaffected, see figure 4.13.

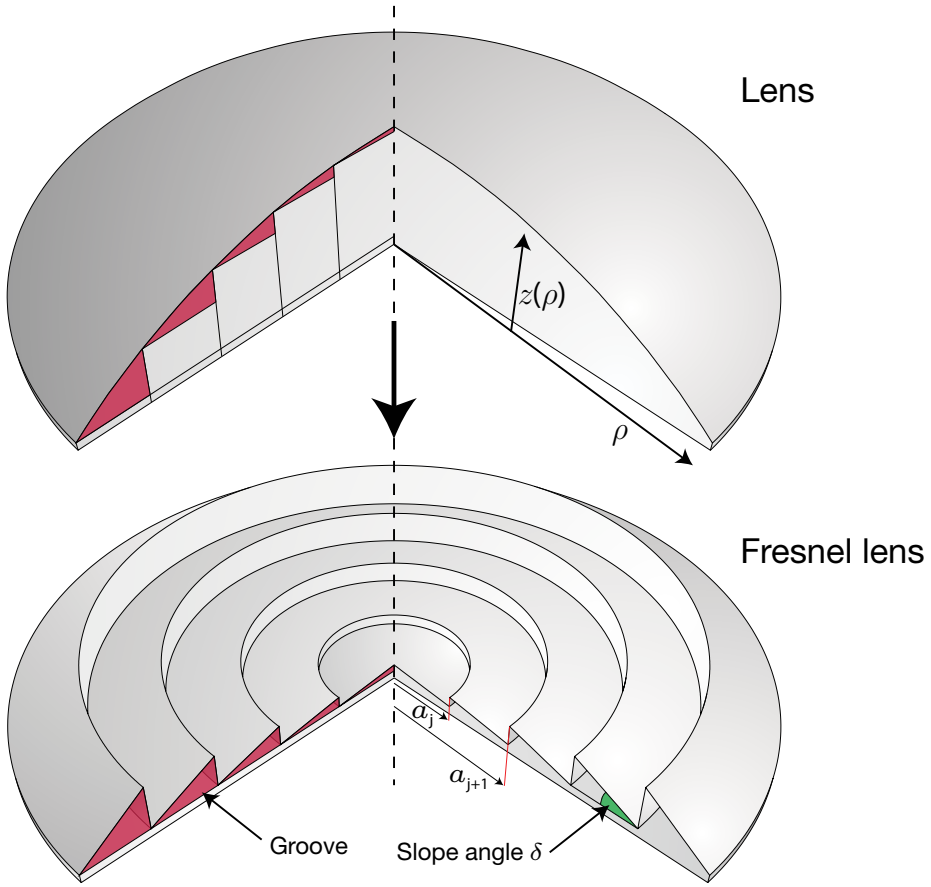

Figure 4.13: Basic construction principle of a Fresnel lens. The bulky lens is divided into a set of concentric annular “prisms” which are named “grooves”. The curvature of the active optical surface still follows the sagitta function (section 4.1) but is approximated by linear segments described by a slope angle δ.

The major disadvantage of this concept results from the stepwise discontinuities in surface between the grooves. Light rays which are bent towards an inactive face that connects two grooves are disturbed due to total internal reflection or additional false refraction as shown in figure 4.14. On top of that, the aberrations of conventional lenses, discussed in the previous section, are also present for Fresnel lenses although the process of manufacturing makes it easier to correct for spherical aberration.

4.2.2 Manufacturing

The Fresnel lens used for the fluorescence telescope FAMOUS is made by compression molding of PMMA[3]. The mold cavity facet geometry is usually cut by a precision diamond tool with a straight cutting edge. Therefore, the active optical surface of the grooves is a flat approximation of the curved lens surface and can be described by a successivly increasing slope angle δ towards the outer region of the lens (figure 4.13). The draft angle ψ also increases with distance to the center of the lens to enhance the transmittance of light, which is refracted near the top edge of a groove (figure 4.14, red dashed light beam). To achieve best transmittance, the angle a_1 (figure 4.14) has to tend to zero. Each of the grooves is individually engraved into the mold, which makes it possible to generate any spherical or aspherical surface profile. It is even possible to generate a groove based on its individual profile, so that every groove on the Fresnel lens is part of a different surface profile. This leads to a maximum degree of freedom to design a lens for special applications [22].

The filling process of the mold cavity is a complicated process because of high temperature and pressure gradients. The Fresnel lens is about 2 mm thick but contains facet structures in the mircometer range. These structures will only be filled with the polymer when it is sufficiently pressurised. The temperature of the filled polymer melt is significantly higher than the temperature of the mold cavity, resulting in a cool down of the polymer after the filling process accompanied by a viscosity increase, which in turn requires additional time dependent pressure control [30].

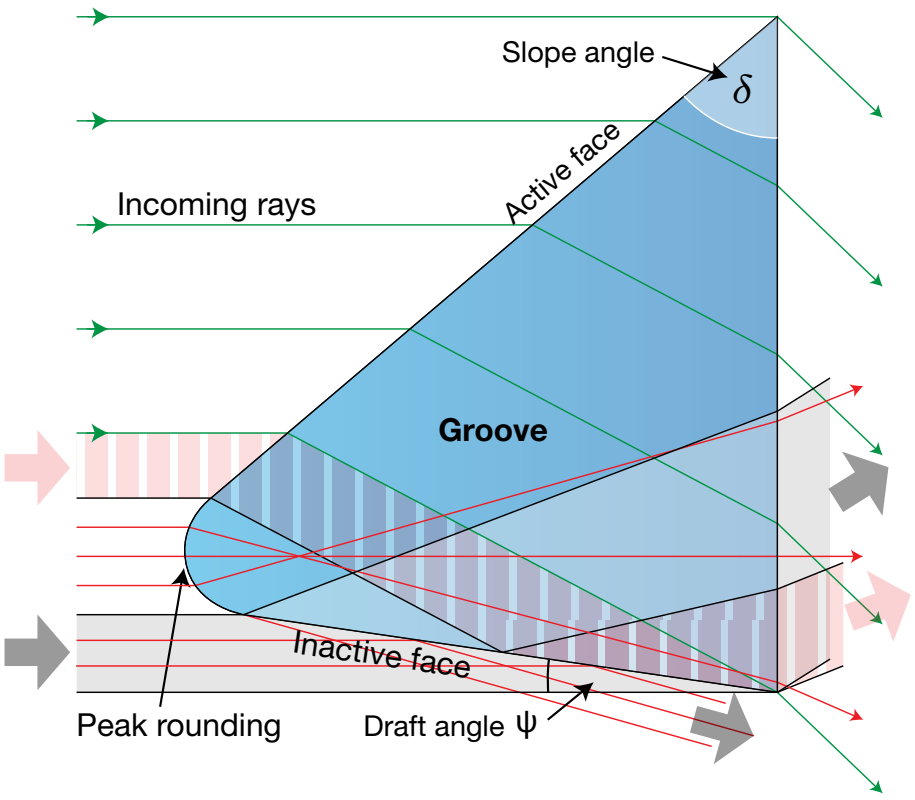

Figure 4.14: Cross section of a groove with relatively high slope angle δ. The fraction of correctly refracted light rays in comparison to the total incoming light gives a first hint on the transmittance of the Fresnel lens.

[3] Polymethyl methacrylate

After the filling process is completed, the polymer has to be cooled and solidified. This step as well as the ejection of the cooled lens from the mold have to be performed in a correct manner to avoid additional stress. The quality of all process parts has direct impact on the performance of the lens. If the pressure after filling the melt into the mold is not high enough or is executed too late, the groove edges are not filled correctly and a rounded groove peak (figure 4.14) is formed, which in consequence reduces imaging quality and transmittance performance [30].

4.2.3 Diffraction of a Fresnel lens

As a first indicator for image quality, the diffraction pattern of a Fresnel lens will be examined and compared to the diffraction pattern of a conventional lens (Airy pattern, section 4.1.2) of same diameter and focal number. The airy pattern results from light passing through finite apertures. A Fresnel lens consists of many annular sections, each representing a circular aperture which is nearly totally obscured, depending on the groove width. The radial intensity of the diffraction pattern for an obscured circular aperture can be expressed as [31]:

$$I(\beta) = \frac{I_0}{(1-\epsilon^2)^2} \cdot \left(\frac{2J_1(x)}{x} - \frac{2\epsilon J_1(\epsilon x)}{x} \right)^2 \tag{26}$$

with maximum intensity I_0 and the bessel function of the first kind of order one $J_1(x)$. The dimensionless variable x is defined in chapter 4.1.2. ϵ is the aperture obscuration ratio. In the case of the groove of a Fresnel lens, ϵ is defined as the quotient of the inner radius a_j and outer radius a_{j+1} of the jth. groove (cf. figure 4.13).

$$\epsilon_j = \frac{a_j}{a_{j+1}} \tag{27}$$

In general, the intensity diffraction pattern on the image plane of multiple apertures may not be simply added up to a total intensity diffraction pattern if the light is coherent, i.e. the incoming light waves on the image plane of different grooves have a fixed temporal and spatial relationship and can interfere constructively or destructively. However, if the discontinuities in optical path length between the single grooves are large, the total intensity diffraction function tends to the ensemble average of $I(\beta)$ [32]:

$$\langle I(\beta) \rangle = \sum_{j=1}^{N} I_j(\beta) \tag{28}$$

In the case of the Fresnel lens, the contributions of the grooves to the total intensity has to be weighted by the corresponding fraction of surface of the groove to the total surface of the lens:

$$I(r) = \sum_{j=1}^{N} \frac{a_{j+1}^2 - a_j^2}{a_F^2} \cdot \frac{I_0}{(1-\epsilon_j^2)^2} \cdot \left(\frac{2J_1(x_j)}{x_j} - \frac{2\epsilon_j J_1(\epsilon_j x_j)}{x_j} \right)^2 \tag{29}$$

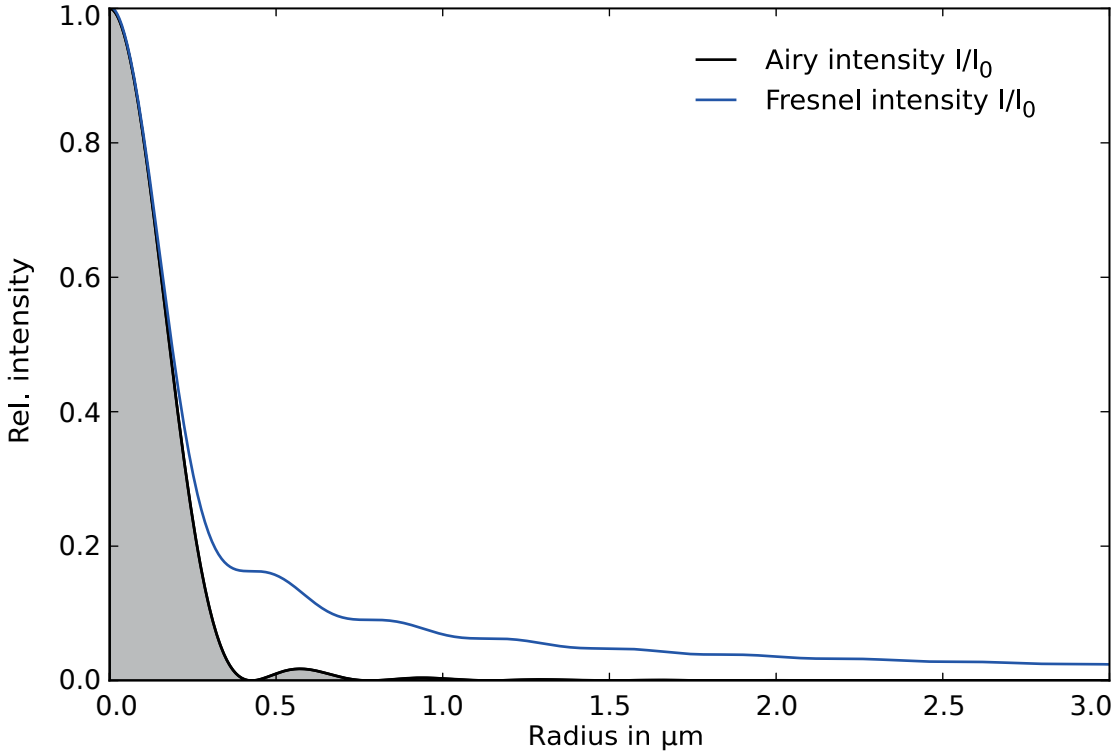

Figure 4.15: Radial intensity distribution of the diffraction pattern for a Fresnel lens of 549.7 mm of diameter and 10 grooves per mm given by equation 29 (blue line) compared to the Airy function with an aperture of the same radius (grey filled line). Light of 350 nm wavelength and a focal length f = 502.1 mm was used.

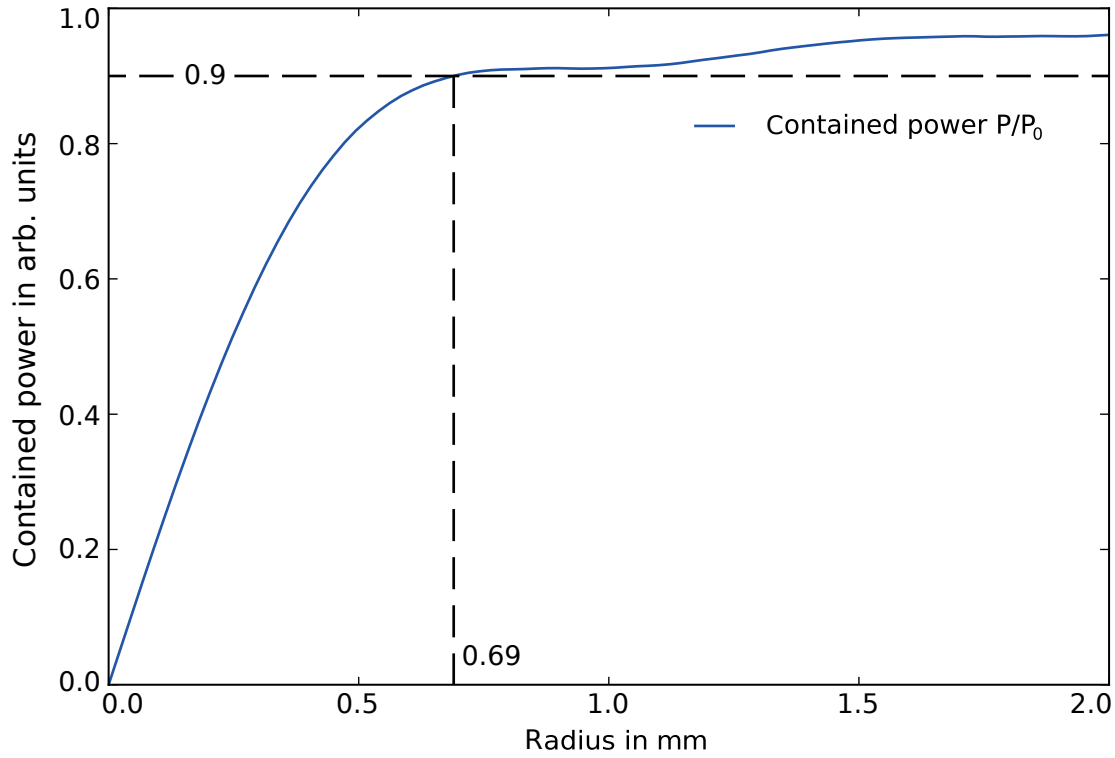

Figure 4.16: Enclosed energy of the diffraction pattern of the Fresnel lens as a function of the radius in mm. The vertical dashed line marks the aberration radius R90 of 90 % encircled energy at r = 0.69 mm. The corresponding plot for the airy function is shown in figure 4.7 with an aberration radius R90 = 0.67 µm.

The dimensionless variable x_j (see section 4.1.2) additionally depends on the aperture radius a_{j+1} for different grooves.

$$x_j \approx \frac{2\pi\, a_{j+1} \cdot r}{\lambda f} \tag{30}$$

The obtained diffraction pattern of a Fresnel lens with 549.7 mm of diameter and 10 grooves per mm, as it is used for the fluorescence telescope FAMOUS, is plotted in figure 4.15 as blue line using light of λ = 350 nm wavelength and a focal length f = 502.1 mm. The Airy pattern of a circular aperture of the same diameter, which was also discussed in section 4.1.2, is plotted for comparison as grey filled line. The radial intensity distribution for the Fresnel lens does not decrease with radius as fast as the Airy funtion. This effect has a large impact on the related aberration radius for the Fresnel diffraction pattern of R90 = 0.69 mm as plotted in figure 4.16, which is about three orders of magnitude larger than the aberration radius of the Airy pattern.

4.2.4 Transmittance

As electromagnetic waves traverse matter, a certain fraction will be absorbed dependent on the material and wavelength. While a conventional lens is thick enough to absorb almost all UV light emitted by an extensive air shower, a Fresnel lens of mere 2 mm is thin enough to fit requirements for the usage in a fluorescence telescope.

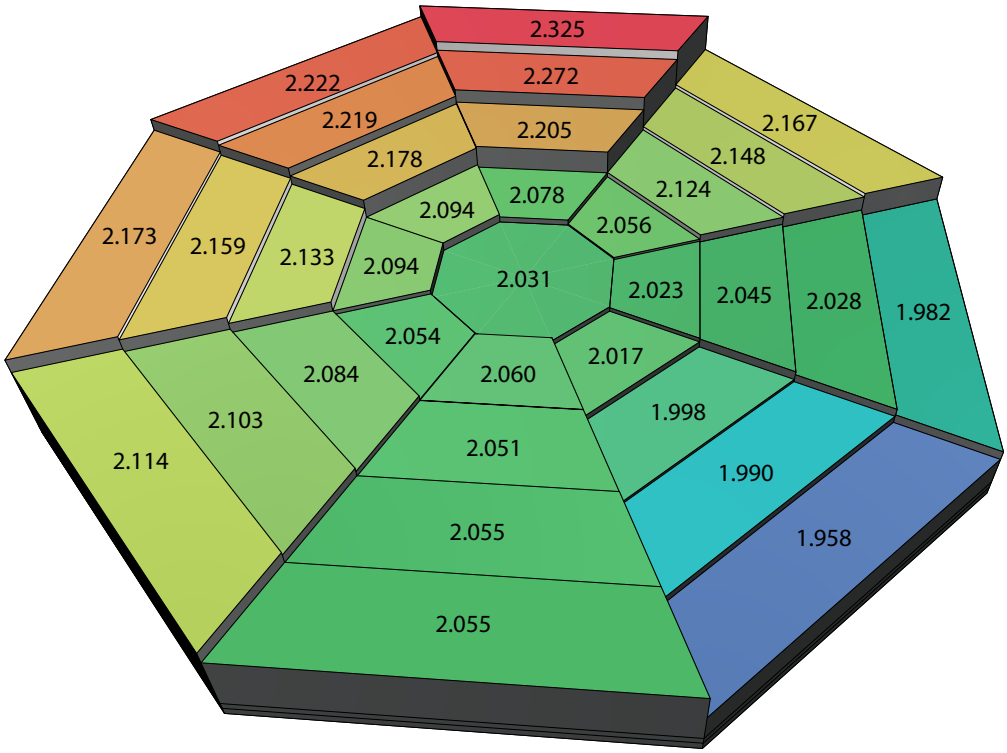

Figure 4.17: The thickness of the Fresnel lens of FAMOUS ranges from 1.958 mm to 2.325 mm. The values are measured with the probe of a CNC milling machine and a precision of ± 0.020 mm.

Unlike in the case of conventional lenses, two factors contribute to the transmittance of Fresnel lenses:

- Despite the use of UV transparent PMMA and a thickness of only about 2 mm (cf. figure 4.17), a small amount of light is still absorbed. The absorbed fraction is estimated to be smaller than 10 % and remains nearly constant over the entire surface of the lens.
- Additionally, the false light scattering at inactive faces leads to a redirection of photons as shown in figure 4.14. Most of these photons will not contribute to the focal point and lead to a reduced transmittance. As the height of the grooves increases with radius and thus also the height of the inactive faces, this effect rises with radius.

4.2.5 Focal point of a Fresnel lens

An important measure for the size of the focal point of a lens is the aberration radius R90, which is the radius of a circle on the image plane, encircling 90 % of the total intensity on the image plane. While the aberration radius of the focal point of a conventional lens is influenced by aberrational effects (section 4.1.3), Fresnel lenses introduce additional dependencies like the granularity g (number of grooves per millimeter) and the draft angle ψ of the grooves, which are discussed in chapter 6. Based on simulations from [18], [22] and this thesis, which analyse the influence of the radius of the Fresnel lens R, the granularity g, the angle of incidence of incoming light θ (cf. figures 8.3 and 8.4) and the focal number N_f of the Fresnel lens (cf. figure 4.18) on the aberration radius R90, the following formula is developed to approximately calculate the aberration radius as a function of the listed parameters for light of 350 nm wavelength:

$$R90(R, g, \theta, N_f) = R \cdot \left(6.50 \cdot 10^{-3} \cdot \frac{1}{N_f} + 0.95 \cdot 10^{-3} \cdot \frac{1}{N_f} \cdot \frac{\theta}{\deg} + 7.58 \cdot 10^{-5} \cdot \left(\frac{\theta}{\deg} \right)^2 \right) + \frac{1}{35} \frac{1}{g \cdot \mathrm{mm}} \quad (31)$$

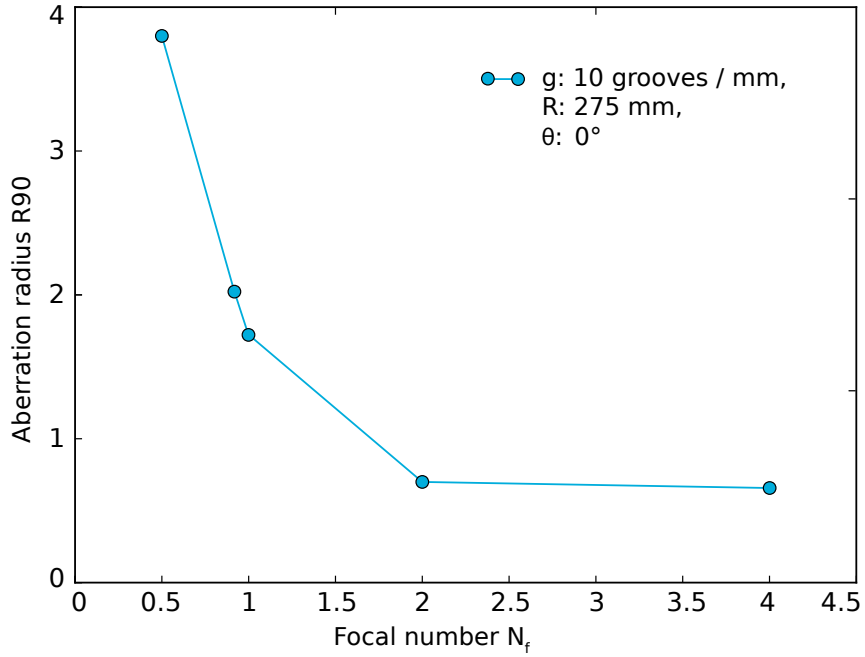

Figure 4.18: Simulated aberration radius R90 of a Fresnel lens as a function of its focal number N_f = f/d. The diameter d of the lens remains constant while its focal length is varied. The incoming light has a wavelength of 350 nm.

5 Measurement setup

In chapter 4, the importance of the point spread function for the understanding of the optical system was explained. As the Fresnel lens is part of the fluorescence detector FAMOUS, observing faint events in large distances up to several kilometers, the point spread function of this lens for a point light source in larger distances and the transmittance has to be measured and analysed. In this chapter, the associated experimental setup will be presented, as well as the construction of its individual components.

Within the scope of Tim Niggemann's master thesis [18], a detector simulation of FAMOUS was developed including a Fresnel lens. As part of this thesis, completely addressing the Fresnel lens, this part of the simulation was revised to add more realistic features. This aspect will be discussed in chapter 6.

A comparison of simulated and measured imaging properties with regard to the point spread function and transmittance will be presented in chapters 8 and chapter 9, respectively.

5.1 Point light source

While stars are suitable light sources for the measurement of the point spread function, the rotation of Earth makes a measurement of desired precision difficult. For this reason, a self made point light source, i.e. a LED in combination with an iris, was placed in about 22 m distance to the lens. By this means, a light source at infinity will be approximated and the related difference (22 m - ∞) can be estimated by simulation (figure 5.1). The aberration radius for the Fresnel lens is expected to increase from R90 = 1.87 mm for a light source at infinity to R90 = 2.00 mm for the point light source at 22 m distance. The focal point shifts from 502 mm to 512 mm distance from the lens.

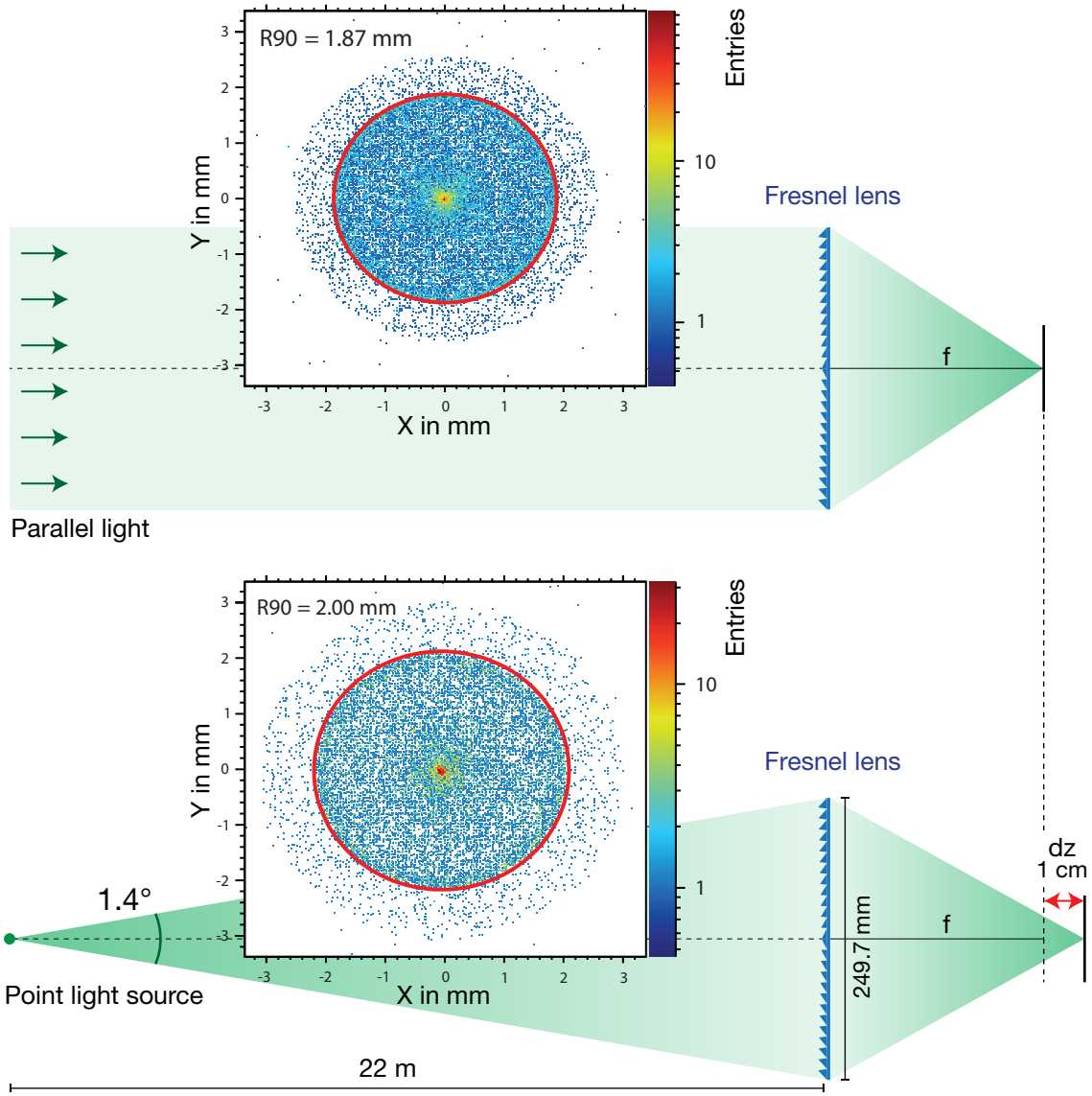

Figure 5.1: An infinitely distant light source illuminates the Fresnel lens with parallel light (top). The focal point will be formed at focal length f from the lens. A point like light source (1 mm diameter) in 22 m distance illuminates the lens with slightly curved wavefronts and is focussed at a distance dz = 10 mm behind the nominal focal length. The spot size of the focal point increases from R90 = 1.87 mm to R90 = 2.00 mm. The point spread functions are generated by a raytracing simulation using Geant4. The light in both cases has a wavelength of 350 nm.

For the experiments, two different LEDs are used. LED1 and LED2 emit photons of approx. 550 nm and 400 nm (figure 5.4) wavelength respectively. The selected LED is mounted into a tubelike casing, directly behind an iris with an aperture of 1 mm diameter (figure 5.2). The back of the tube is closed with only two electric cables exiting, which provide the LED with adjustable current. A picture is shown in figure 5.2. This design ensures that light of the LED can only emerge the tube case by passing through the iris, forming a point like light source. The 22 m distant Fresnel lens forms an angle of Φ =1.4° from the position of the light source (figure 5.1). The radiation pattern of the UV LED2 is shown in figure 5.3. The red area marks an angle of ± 0.7 degrees and illustrates that the Fresnel lens is illuminated reasonably homogeneously.

Figure 5.2: The light source for the experiments. The LED is placed behind an iris of 1 mm diameter. For the close up, the iris was opened completely.

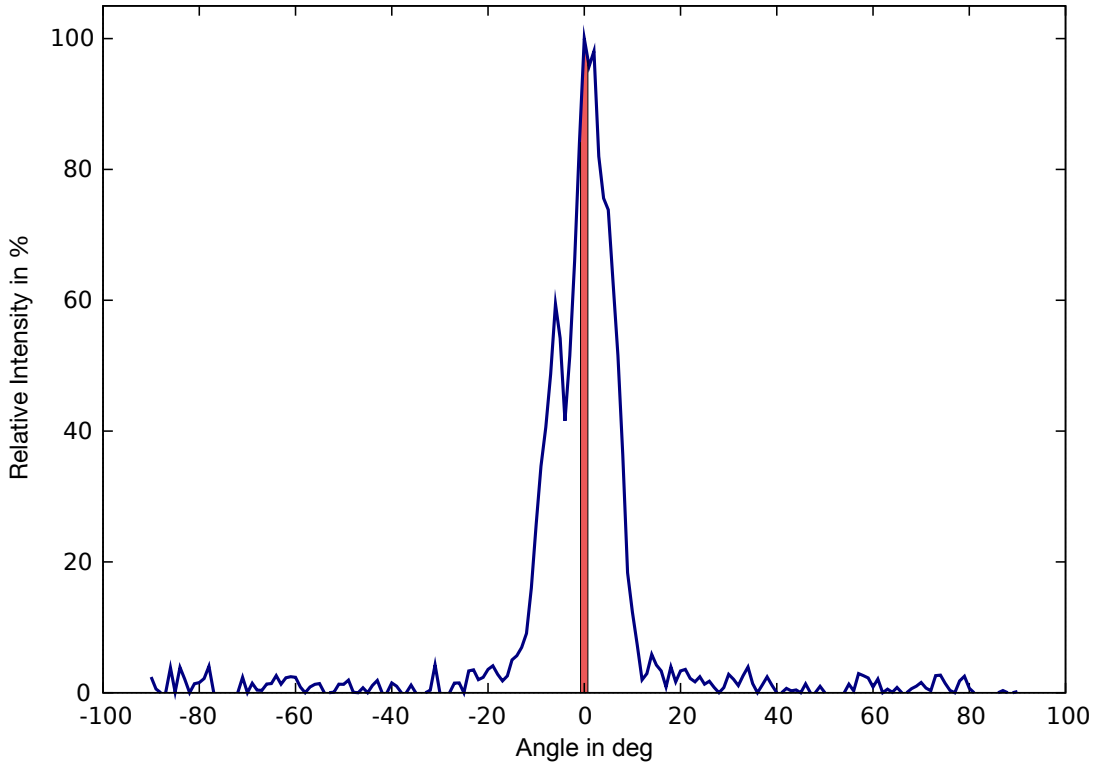

Figure 5.3: Radiation pattern of the used UV LED [33]. The red area marks an angle of ± 0.7° illuminating the lens.

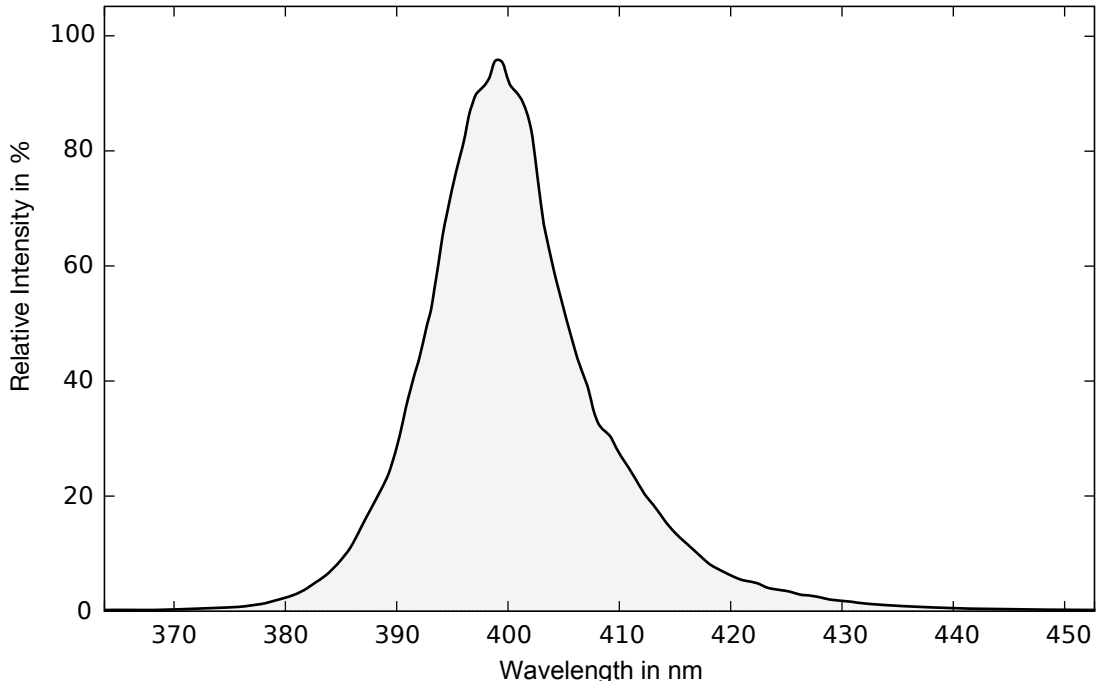

Figure 5.4: Spectrum of the used UV LED with peak intensity at λ = 400 nm. Measurement by Tim Enzweiler.

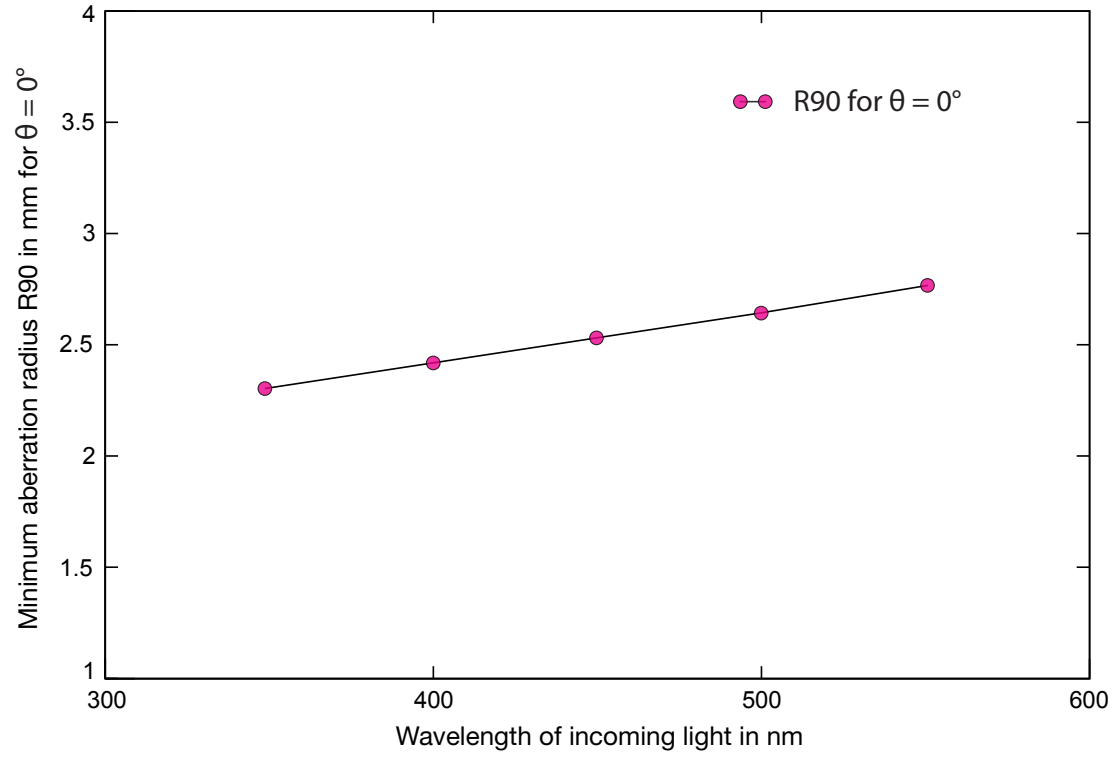

Figure 5.5: Simulated best focus aberration radius R90 as a function of the wavelength of the incoming light for an angle of incidence θ = 0°. The convolution with the Fresnel diffraction pattern is included.

For the measurement of the aberration radius R90 of the Fresnel lens, LED1 with 550 nm is used, to ensure a good compatibility with the light sensor of the Sony Nex-5. To conclude on the aberration radius R90 for UV-light, a series of simulations is performed to study the dependency of the aberration radius on the wavelength of the incoming

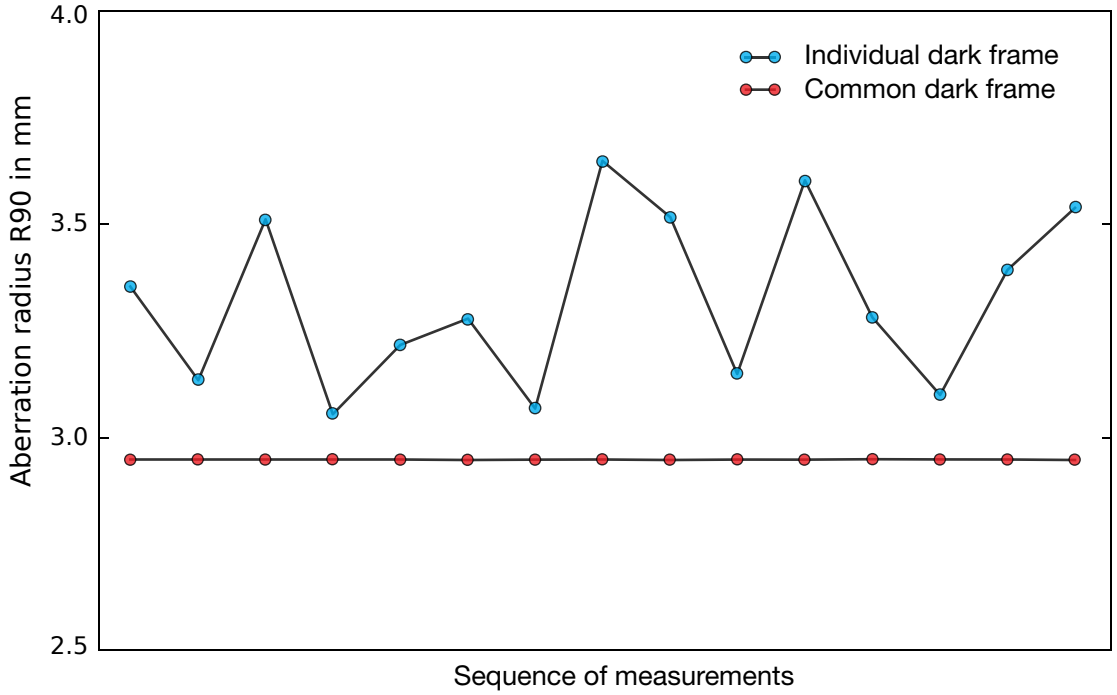

Figure 5.6: Two series of measurements: Measurements with individual background image show high fluctuations of about 0.5 mm, while measurements with constantly activated LED show nearly no fluctuation of about 0.5 µm.

light. In figure 5.5, the aberration radius is plotted as a function the wavelength for an angle of incidence $\theta = 0°$. As the diffraction of light also depends on the wavelength, this effect is included in figure 5.5 (cf. section 6.2). For higher angles of incidence, the influence of the wavelength on the aberration radius decreases.

In the early stages of the experiment, the constructed light source was equipped with a remote power switch to turn off the light from the position of the lens to create frequent background image measurements. Details about background image subtraction are explained in chapter 7. However, after a couple of test measurements, the idea to follow a background image on each signal record had to be discarded because of a warm-up period of the LED. All measurements performed within a 10 minute window after switching on the LED showed a time dependence, and measurements with frequent on/off switching due to background image measurements gave highly inconsistent results. The LED brightness reduces during the warm-up period.

Two series of measurements of the aberration radius for the point spread function of the Fresnel lens are presented in figure 5.6. The experimental set-up remained unchanged for all measurement points. The line with blue points shows a sequence of measurements with an individual background image for each single measurement. The horizontal line with red points results from a sequence of measurements wich was performed with a common background image taken at the end of the sequence, which was started after a 15 minute warm-up time of the LED. The higher LED brightness during the warm-up period in combination with the image compilation as part of the analysis process (cf. chapter 7) leads to an increased aberration radius R90 for the measurement with individual background images (blue dots).

5.2 Dark room

All measurements are carried out in a long tunnel of the RWTH Physikzentrum to ensure absolute darkness while measuring. This is of high importance as the large Fresnel lens does an excellent job in collecting light from small and weak sources that impair measurement results. The only obviously unwanted light sources that had to be eliminated were a basement window and an emergency lighting. After numerous successful test runs, a few smaller light sources were spotted, for example light passing through the keyhole of the door.

The tunnel is roughly 2.5 m wide, 2 m high and over 30 m long. As stated before, the point light source is placed in about 22.3 meter distance to the lens, also called the long conjugate. Another disruptive effect is involved when the light rays of the point light source are scattered at nearby side walls, supporting pillars and the ceiling, hence arriving at the lens under fault angles. To prevent that, a partition wall is placed between lens and light source. The wall contains a circular window, correctly sized and positioned to grant direct visual contact from the light source to every point of the lens, but blocks all other scattered rays, see figure 5.7.

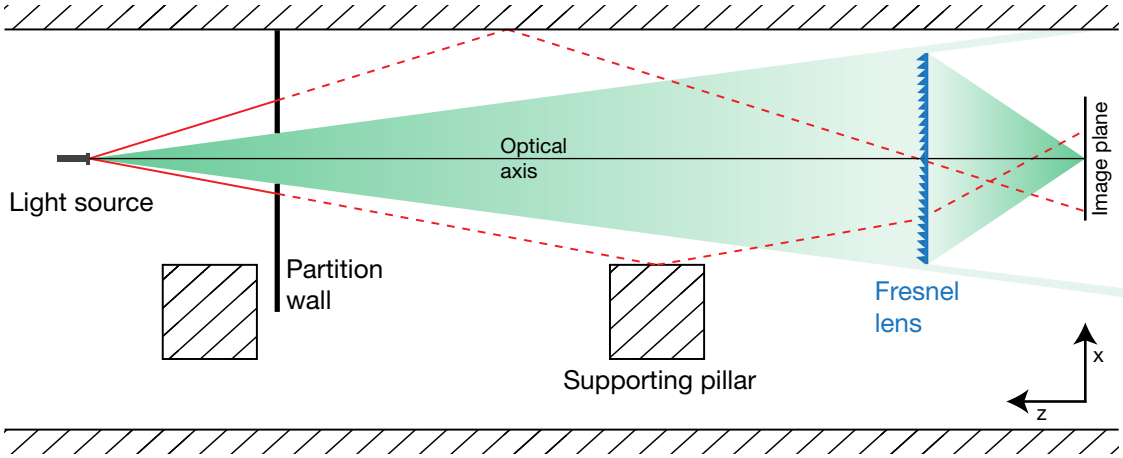

Figure 5.7: Top view of the experimental setup in a long tunnel of a cellar. A partition wall is placed between lens and light source to prevent false light scattering at the side walls, supporting pillars and the ceiling.

5.3 Light sensor

The point spread function of a Fresnel lens is a two-dimensional light intensity distribution, which can be measured by a suitable light sensor placed parallel to the focal plane. Based on first simulations, the spot size, described by the aberration radius R90, ranges between 2 mm for parallel incident light and 9 mm for incoming light with an incidence angle of 12°. With the aim to minimise optical components to reduce unknown characteristics involved to the process of measurement, the focused light coming from the Fresnel lens is directly recorded by the APS-C format image sensor of a modified Sony Nex-5 digital compact camera (figure 5.9). The camera needs to fulfill certain requirements as described in the following.

To record a light spot of up to 1 cm radius, the camera needs to be equipped with a big light sensor, which is normally found in digital single lens reflex (DSLR) cameras. On the other hand, the flange focal distance (FFD), which is the distance from the lens mounting flange to the image sensor (figure 5.8) needs to be small, since the light which comes from the outer regions of the Fresnel lens (with radius R and focal length f) has an incidence angle of arctan(R/f) = 28.7° on the image sensor and is obstructed by the camera housing.

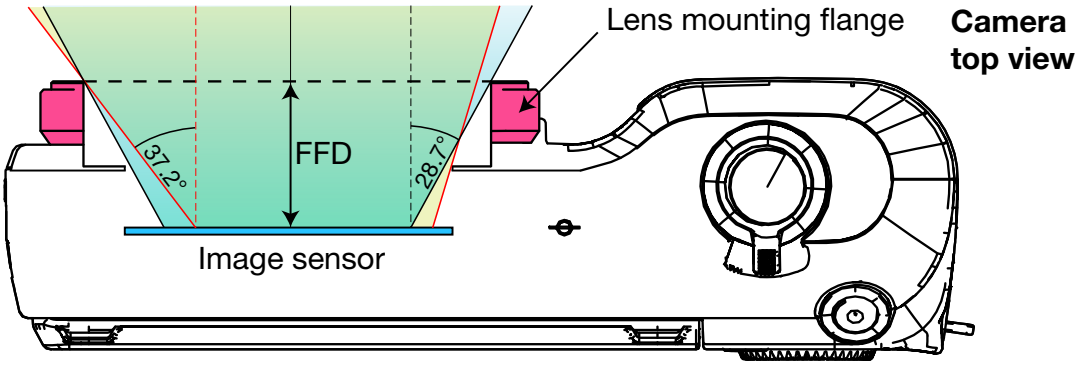

Figure 5.8: Top view of the Sony Nex-5. The camera housing and lens mounting system have a shading effect for light coming from outer regions of the Fresnel lens, which has an incidence angle of 28.7°. The maximum incidence angle of 37.2° on the image sensor results from off-axis image points with 12° incidence on the Fresnel lens. The obstruction decreases for a smaller flange focal distance. Modified from [34].

Therefore, DSLR cameras are not suitable for the experiment as the mirror cage is positioned between the lens mounting system and the image sensor, which results in high flange focal distances. Figure 5.8 illustrates the inner structure of the Sony Nex-5 compact camera which was selected for the experiments.

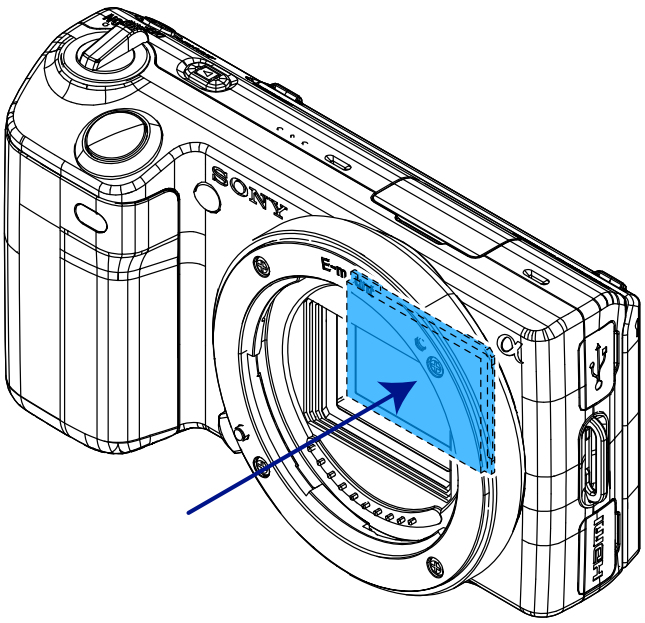

Figure 5.9: Sketch of the Sony Nex-5 without lens. Despite the low flange focal distance, the image sensor (blue) is still obstructed by the camera housing. Adapted and modified from [34].

This camera uses a 14.2 megapixel APS-C format CMOS image sensor of 23.4 mm width and 15.6 mm height. In addition to that, the camera uses Sony's "E"-mount system which is derived from "eighteen" and describes a very low flange focal distance of only 18 mm. Despite these good conditions, the sensor is still obstructed, which leads to problems with the measurement of off-axis image points with a maximum incidence angle of 12° on the Fresnel lens resulting in 37.2° maximum inclination on the image sensor (figure 5.8). To avoid obstruction in this situation, the camera was completely disassembled. The lens mounting system was removed and the shutter unit was modified (see figure 5.11) to provide the image sensor with a maximum field of view. The modified Nex-5 is shown in figure 5.10.

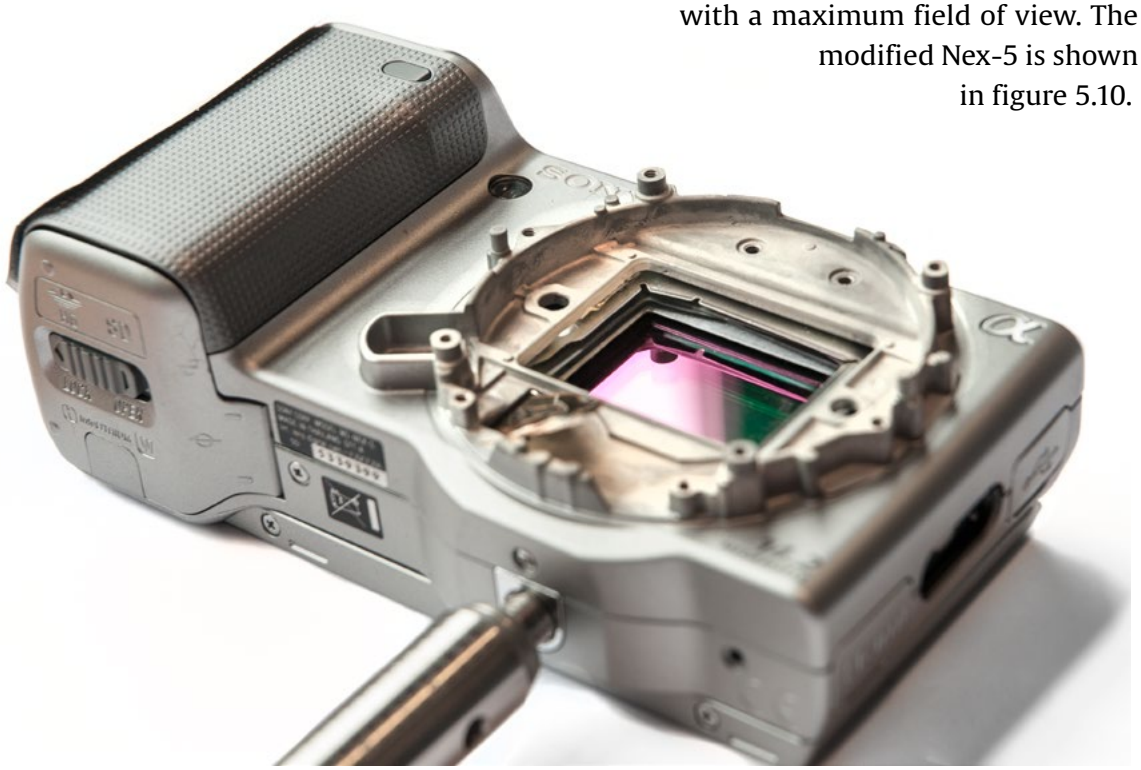

Figure 5.10: Picture of the modified Sony Nex-5. The lens mounting system is removed and the shutter unit is modified.

Figure 5.11: Exploded view of the Sony Nex-5. The red parts are removed completely and the shutter unit (green) was modified, to enhance the field of view of the image sensor (blue). To access the shutter unit, the camera had to be disassembled completely, as it can only be opened at the cabinet rear block and each following layer has to be removed seperately. Modified from [34].

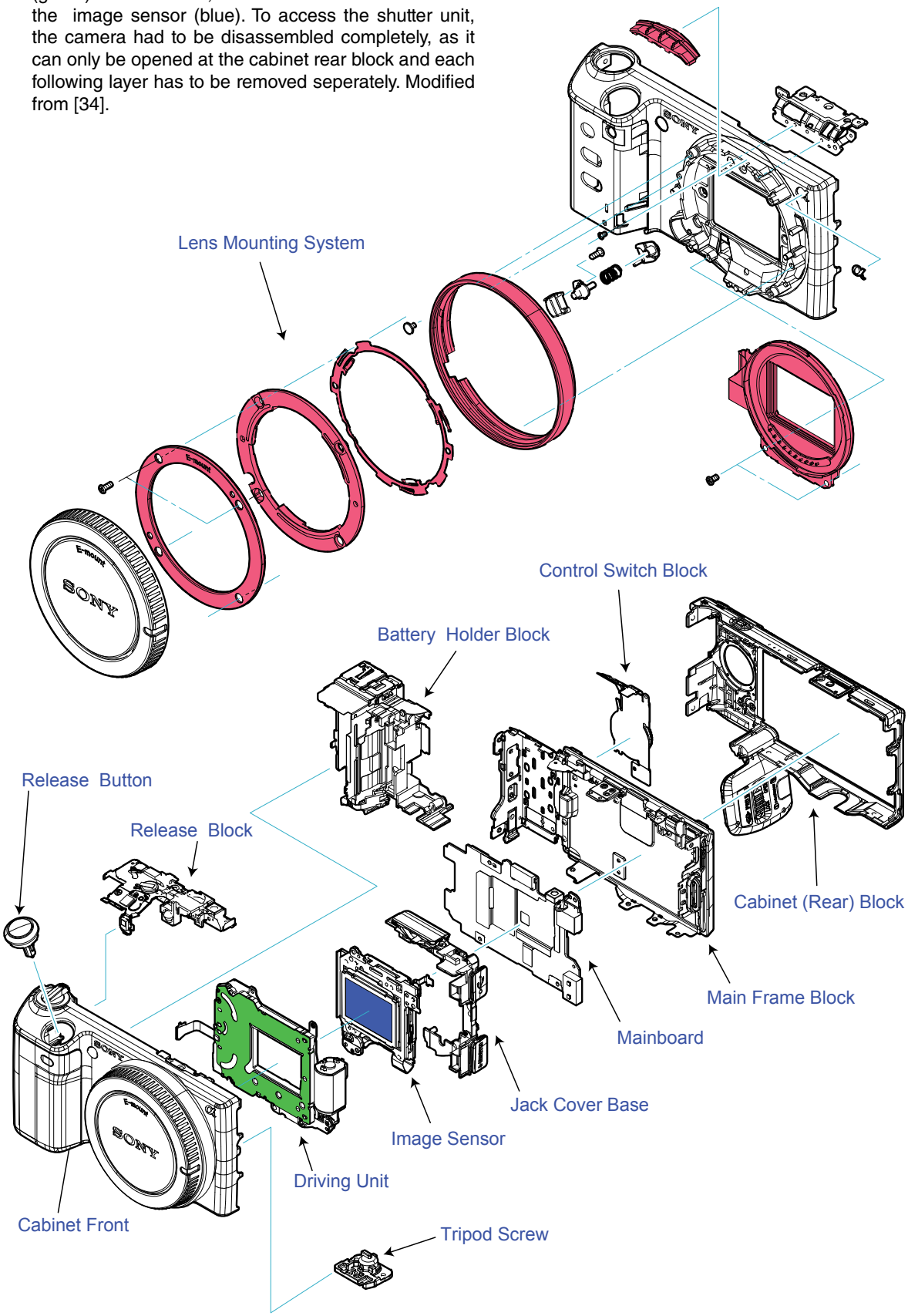

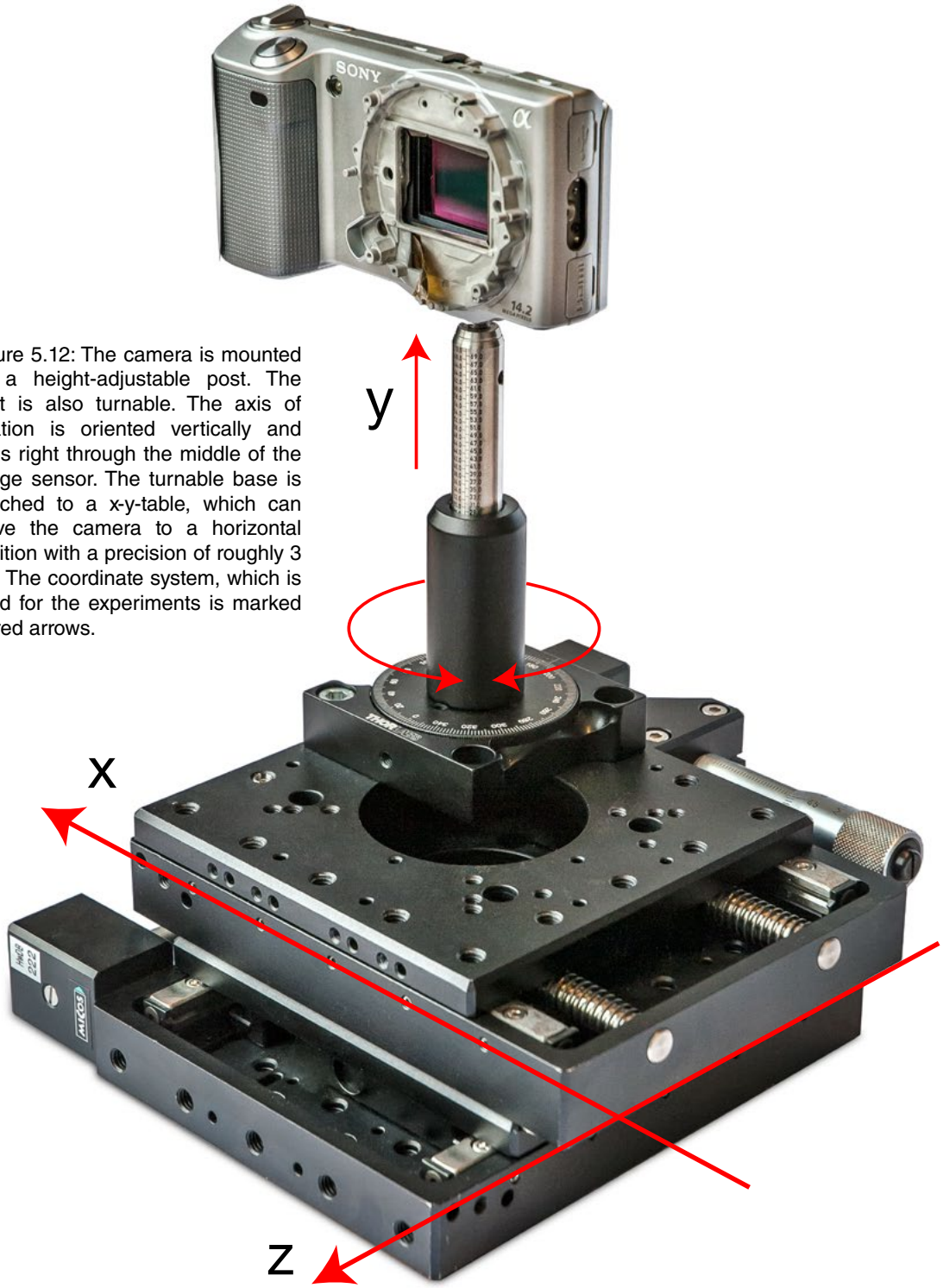

Figure 5.12: The camera is mounted on a height-adjustable post. The post is also turnable. The axis of rotation is oriented vertically and goes right through the middle of the image sensor. The turnable base is attached to a x-y-table, which can move the camera to a horizontal position with a precision of roughly 3 µm. The coordinate system, which is used for the experiments is marked as red arrows.

To control and vary the relative position of the camera to the lens, the modified Nex-5 was mounted to a height-adjustable post on a turnable base with vertical axis of rotation, as shown in figure 5.12. To set a desired horizontal position, a x-y-table with a precision of roughly 3 µm is used. For the experiment, this sensor is mounted on a specially designed test bench, which is described in the following section.

5.4 Test bench

The precise alignment of all optical components is crucial for the characterisation of the Fresnel lens. To control the position of lens and camera, a test bench was designed. The Fresnel lens is clamped by three aluminium profiles as shown in figure 5.14 without any mechanical stress. As the purpose of this lens is the focussing of a collimated light beam, the grooves, which approximate the curved optical surface, are directed towards the point light source, as explained in chapter 4.1 for the plano convex conventional lens. The profiles and the image sensor including the x-y-table are fixed on a breadboard.

To measure the point spread function of an off-axis image point, i.e. light rays of that point will enter the aperture (Fresnel lens) with an incidence angle α relative to the optical axis, the breadboard, including lens and image sensor, can be rotated with a vertical axis of rotation in the center of the Fresnel lens (see figure 5.13). The position of the image sensor relative to the breadboard has to be re-adjusted to record the point spread function for different incident angles . The angle of rotation can be adjusted with the help of an angle scale, which is positioned in 0.5 m distance from the axis of rotation and allows to set an angle with a precision of approx. 0.05°.

For the measurement of the point spread functions, the image sensor is always aligned parallel to the lens. The z-axis is defined by the optical axis which is perpendicular to the image sensor and the lens. The distances between image sensor and Fresnel lens are measured perpendicular to the z-axis and not with regard to the lens center. The x- and y-axes describe the dimensions of the image plane, while the x-axis is aligned horizontally. As the focal point manifests along the axis of incidence of the incoming light, the image sensor has to be moved along the z- and x-axis, while searching the best focus for off-axis image points.

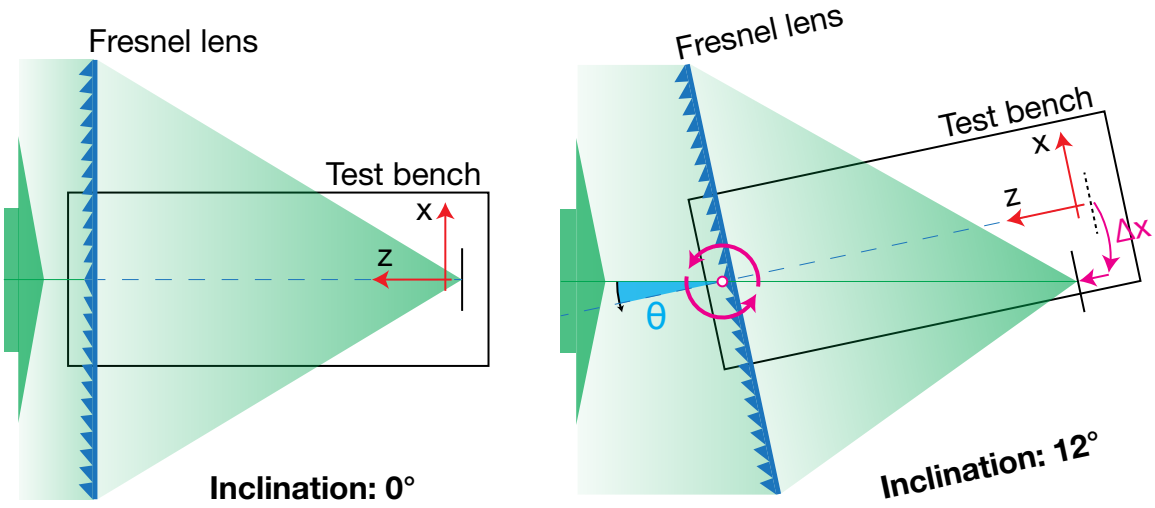

Figure 5.13: Top view on the test bench for two inclination settings. On the left, the axis of incoming light equals the optical axis with an incidence angle θ of 0°. On the right, the test bench is adjusted for the maximum relevant incidence angle of θ = 12°. The position of the camera has to be re-adjusted due to the rotation of the test bench and petzval field curvature.

Figure 5.14: Photo of the test bench. The breadboard is rotatable including Fresnel lens and image sensor. The axis of rotation intersects at the middle of the Fresnel lens, which is clamped by three aluminium profiles without any mechanical stress. The angle scale (close-up) is positioned with a radius of 0.5 m to the axis of rotation.

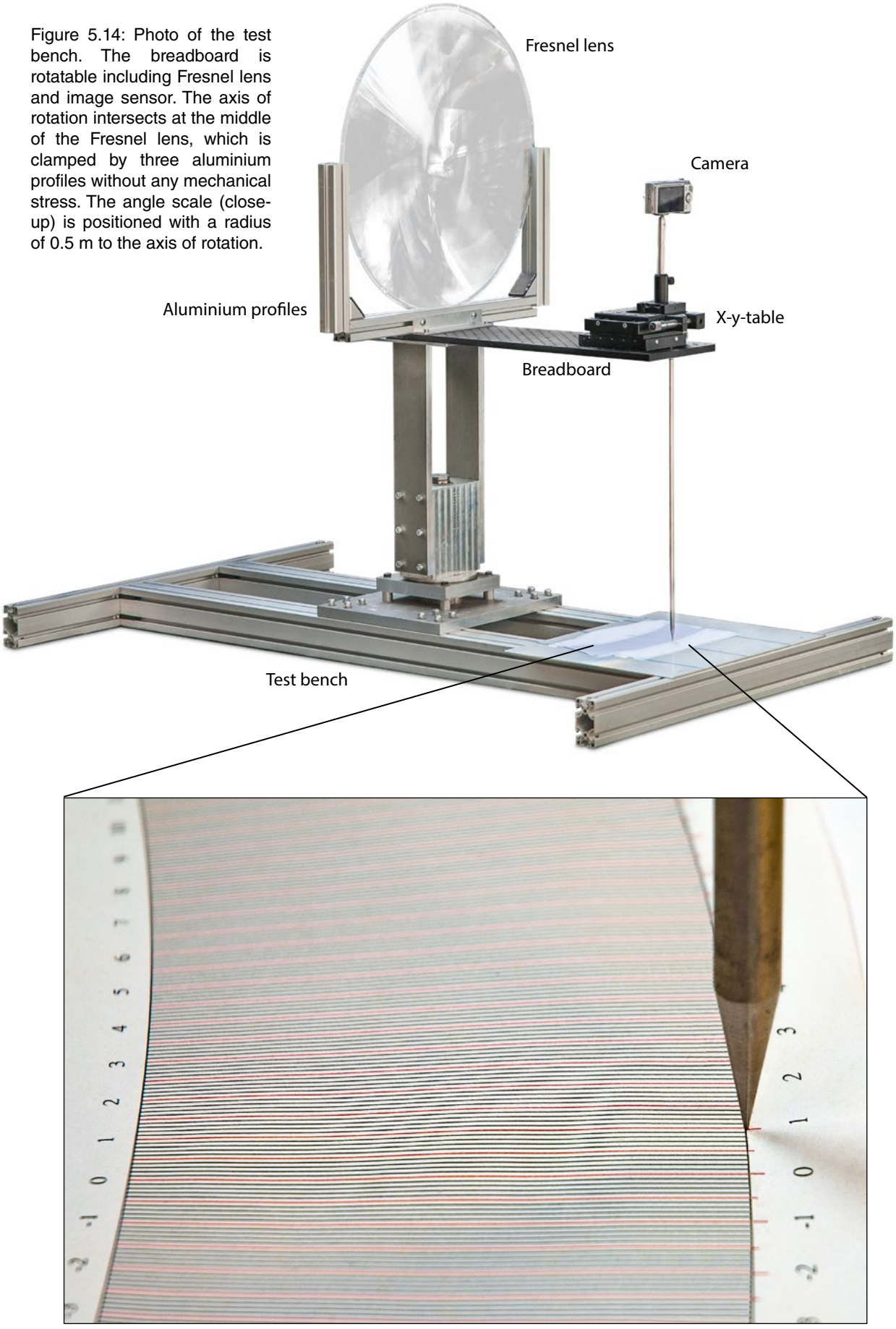

6 Raytracing simulation

The ray tracing simulation of the Fresnel lens was developed on basis of the Geant4 toolkit in [18]. To analyse the point spread function, a light source of 1 mm in diameter, placed in 22.3 m distance, illuminates the lens homogeneously. A limited number of randomly distributed optical photons is sent towards the lens. While interacting with the lens material, reflection and refraction at medium boundaries as well as bulk absorption processes are considered. The diffraction of light is not implemented at that point and needs to be introduced later.

To measure the simulated point spread function, multiple detector surfaces are placed in 0.4 mm intervals along the axis of incoming light on the other side of the lens (cf. figure 6.1). Each of these surfaces is transparent for photons, but tracks the point of impact. By this means, the complete light beam can be sampled in layers, including one layer which records the image of the point spread function of minimal aberration radius R90, see figure 6.1. The detector surfaces are aligned parallel to the lens, to reproduce a flat focal plane. Each detector surface is 0.01 mm thick and has an extent of 100 mm in width and height. Additionally, a smaller area of that surface can be defined as a secondary detector to analyse the impact of limited detector sizes.

6.1 Fresnel lens groove profile

To add more realistic features to the surface of the Fresnel lens, the parameterisation of the groove profile was improved as described in the following sections:

First, a draft angle ψ for the inactive faces was implemented (figure 6.4). The purpose of this angle is to prevent total reflection of light rays which are refracted towards the draft face on entering the groove. Additionally, a draft angle is important for the manufacturing process as it helps to extract the Fresnel lens from the mold cavity. A series of simulations using different constant draft angles ψ is performed to study its influence on the aberration radius R90 and on the transmittance. The draft angle is implemented to the grooves as illustrated in figure 6.5. The slope of the active faces and the groove width remain unaffected to keep the global parameters (focal length and granularity) of the lens unchanged.

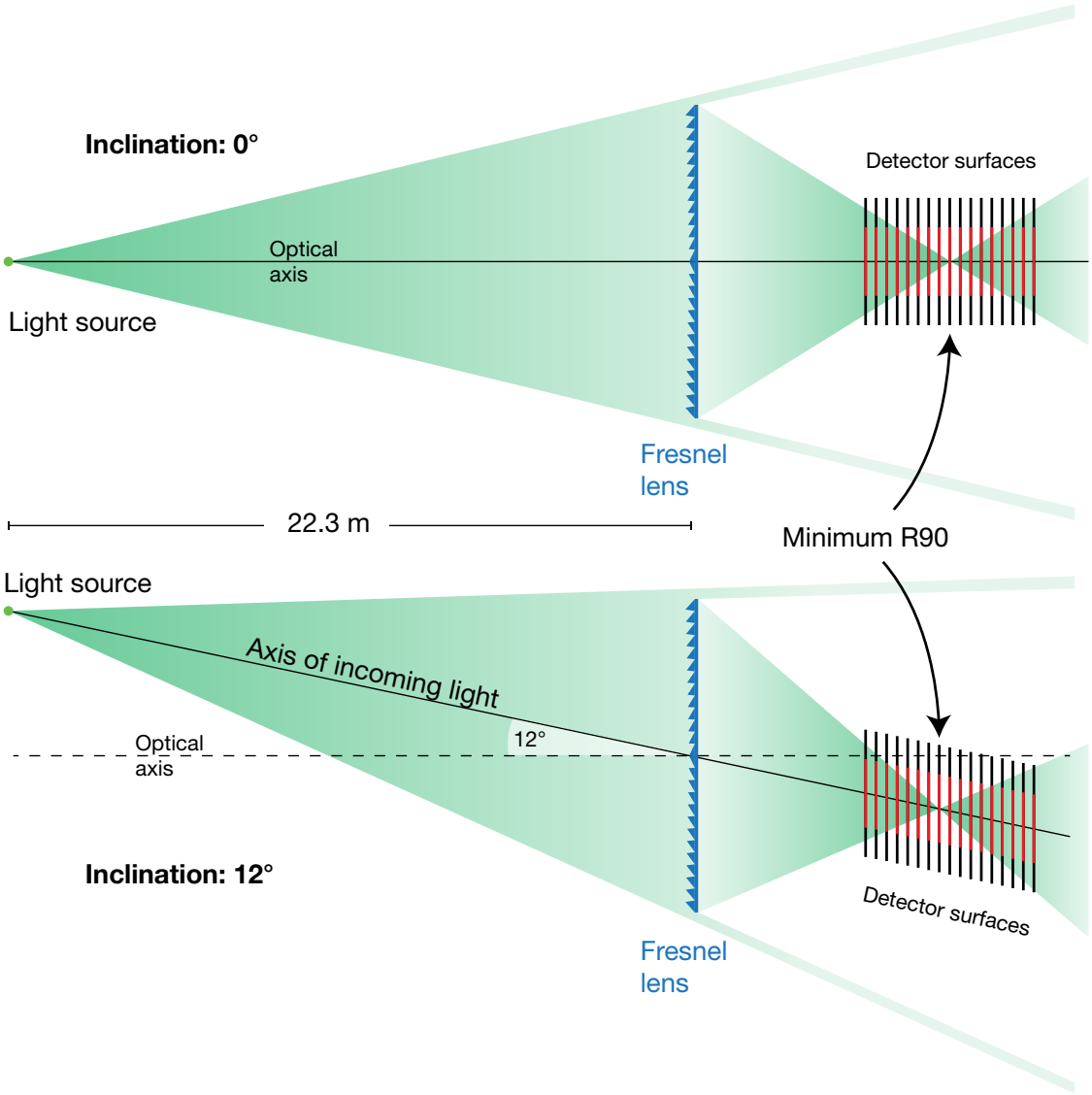

Figure 6.1: Top view of the simulation layout for two different incidence angles: 0° (top) and 12° (bottom). A series of detector surfaces is placed along the axis of incoming light with a spacing of 0.4 mm to find the focal point with a minimum aberration radius R90. A smaller detector (marked red) is defined to analyse the impact of a limited detector size. The detector surfaces are aligned parallelly to the lens.

In figure 6.2, the aberration radius R90 is plotted as a function of constant draft angle ψ and different peak rounding radii, as discussed later (cf. figure 6.4). For larger draft angles than $\psi > 10°$, the aberration radius R90 decreases. This dependency can be explained with photons which contribute to the outer parts of the focal point, i.e. photons which are not refracted perfectly and fill the outer parts of the PSF. For higher draft angles, more of these photons are scattered off the inactive faces of the grooves to completely miss the focal plane. As a result, the PSF is only formed by photons arriving near the actual focal point - the aberration radius decreases as well as the transmittance (cf. figure 6.3).

To analyse the contribution of light scattered off the inactive faces and peaks of the grooves to the aberration radius R90, these parts of the lens are shaded. The results of this simulation are presented in figure 6.2 and figure 6.4 as purple dots. The contribution of photons, which are scattered by inactive faces, to the aberration radius is relatively small, as most of them would miss the focal plane anyway.

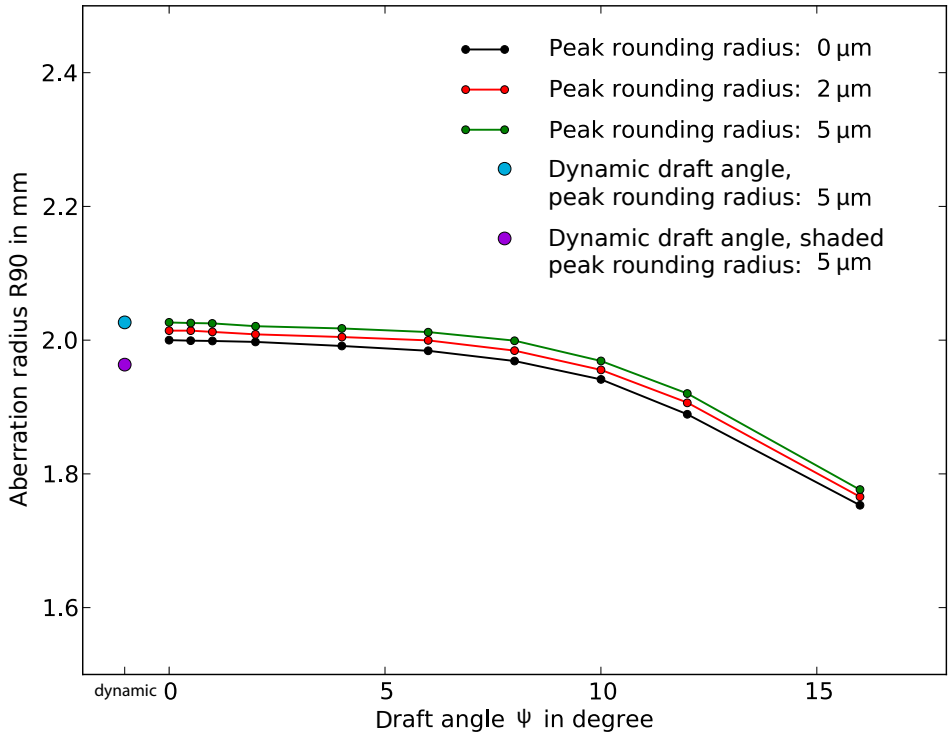

Figure 6.2: Series of simulations using different constant draft angles in comparison with a dynamic draft angle. The aberration radius R90 drops for higher draft angles, which is the result of an increasing number of photons which miss the focal plane. See also figure 6.3. The influence of different peak rounding radii is plotted in different colours. The incoming light has a wavelength of 350 nm.

To achieve an optimal groove profile for the Fresnel lens, the draft angle ψ of each groove has to equal the bending angle of light, passing the corresponding active face [35]. As the bending angle increases with distance to the center of the lens, a constant draft angle leads to an optimised height profile for only a small fraction of all grooves of the lens. Consequently, the draft angle ψ needs to increase with the distance of the corresponding groove to the center of the lens, as the bending angle does, starting from 0° for the center grooves. However, the minimum draft angle is limited to ψ = 3° due to the manufacturing process. The dynamic draft angle in degrees as a function of the distance to the center of the lens in mm for the used lens of FAMOUS is shown in figure 6.3 [35]. The results for the dynamic draft angle are also presented in figures 6.2 and figure 6.4.

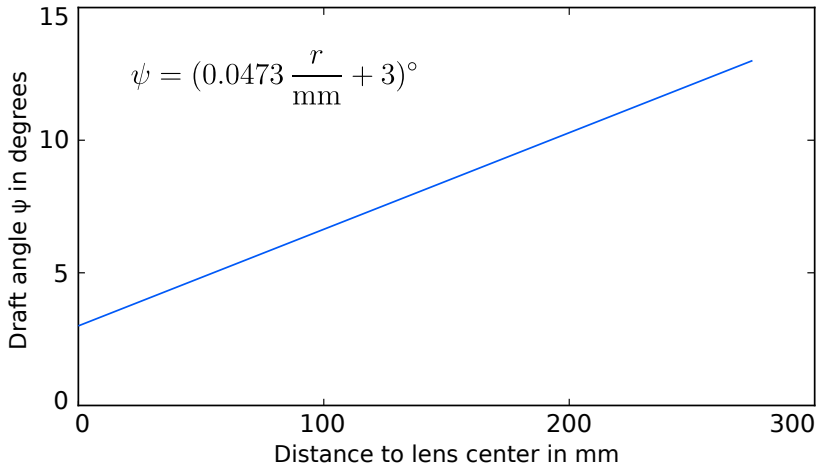

Figure 6.3: Dynamic draft angle ψ as a function of the distance of the corresponding groove to the lens center.

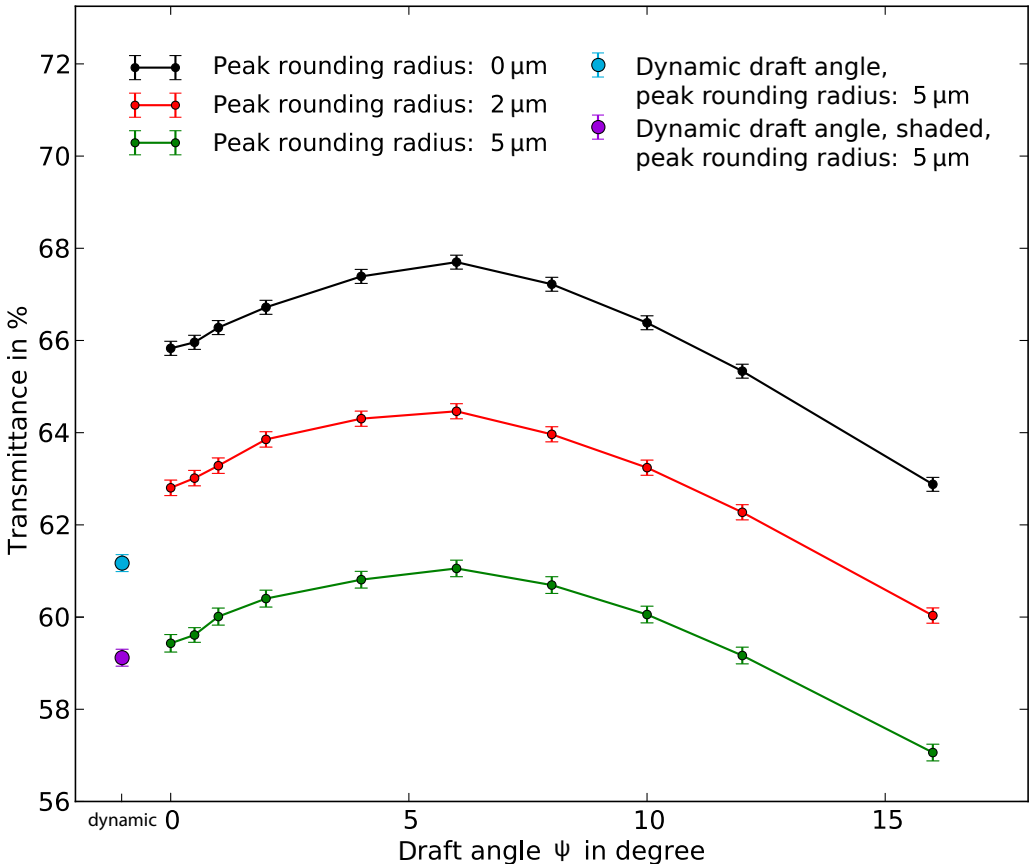

Figure 6.4: Series of simulations using different constant draft angles in comparison with a dynamic draft angle. The transmittance increases for smaller draft angles but decreases for $\psi > 6°$. The statistical uncertainty is derived from the standard deviation of the counted photons. Each run contains 10^4 photons. The influence of different peak rounding radii is plotted in different colours. Light of 350 nm wavelength is used.

Furthermore, the tips of the peaks of all grooves are not perfectly sharp, but rounded with a preferably small rounding radius. This feature was also implemented in the simulation as follows:

A circle of adjustable radius r is calculated to be tangent to the active and inactive face of a groove (figure 6.5). These points of contact are the start and the endpoint of curvature. The circular arc has to be approximated since all volumes are described by polygons in Geant4, which means that surfaces cannot be defined by continuous functions but by linear segments. For this reason, a second parameter can be configured, which sets the number N of points to be used to describe the rounded edge. For the presented results, all curved parts of the grooves are approximated using $N = 5$ points. The needed geometrical considerations to calculate the points of contact and the center of the circle are shown in figure 6.5. Additionally, a similar procedure is applied for the connection edge of the grooves to give a rounding with radii r_2 and r_3 to them. The final groove profile is shown in figure 6.5. The rounding radius r of the Fresnel lens of FAMOUS ranges between 5 and 6 µm, while the radii r_2 and r_3 are set to 1 µm, the width of the groove is set to $d = 100$ µm. The influence of different rounding radii r are also presented in figure 6.2 and figure 6.4.

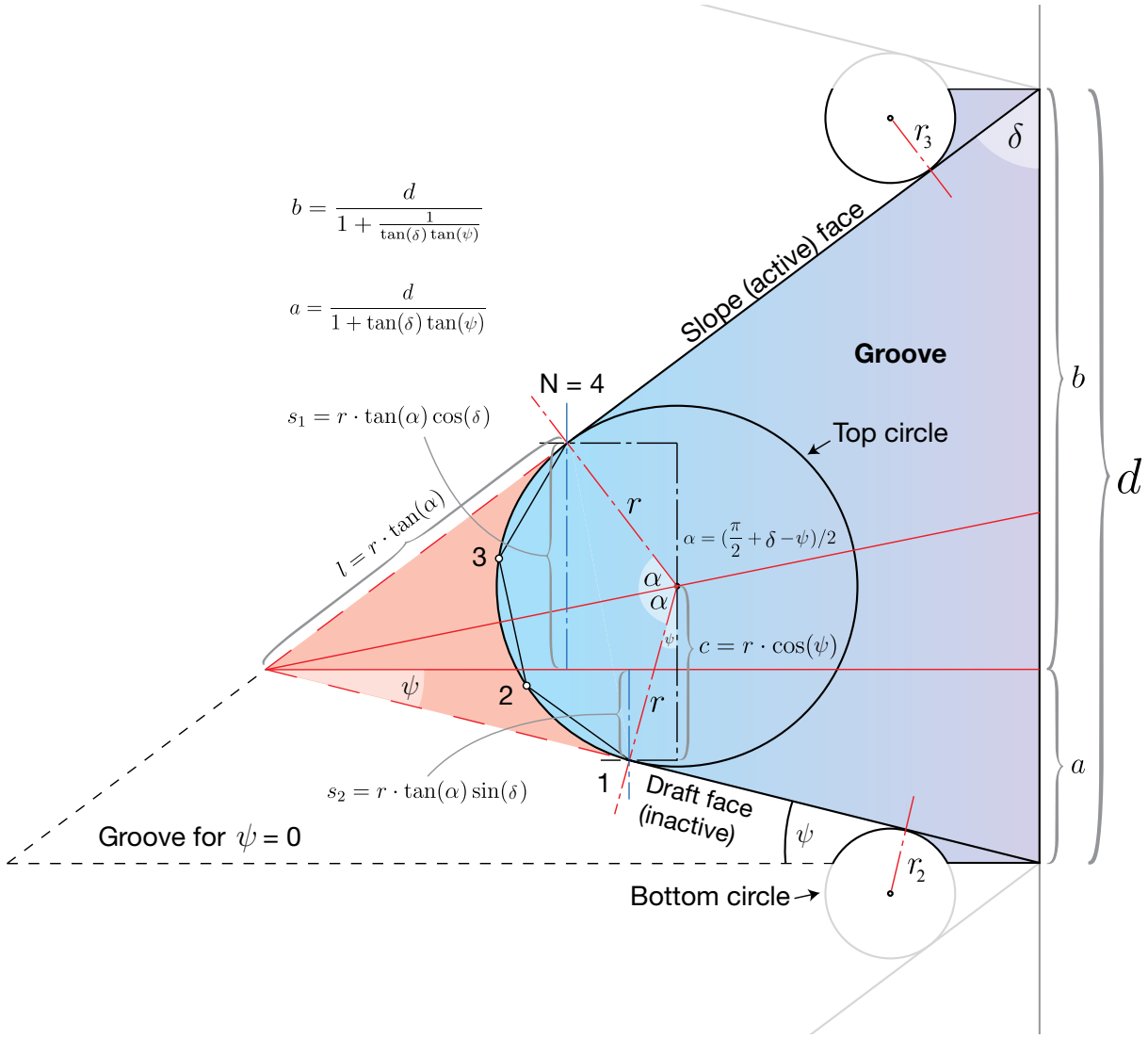

Figure 6.5: Cross section of a groove of the simulated Fresnel lens. A circle of adjustable radius r forms the top peak. The red filled area marks the perfect groove profile. Two additional circles of smaller radius r_2 and r_3 form the connection between the consecutive grooves. Half of both connections are part of the actual groove. The generated curved parts of the groove need to be approximated by linear segments, since Geant4 uses polygons. The number N of points used to describe the peak and connection rounding is also adjustable. For the presented results, every circular arc is approximated by N = 5 points. The relative size of the circles and the groove do not correspond to reality.

For small groove heights of the order of the adjusted rounding radii and below, which can be the case for the inner grooves of the lens, this procedure runs into problems as top and bottom circle fail to form the intended groove connection. In that case, the top circle is shifted to the common intersection point with the bottom circle and the draft face to solve the problem, as illustrated in figure 6.6. The generated transition is not always smooth, but this is not needed as the transitions of the inner grooves of a realistic Fresnel lens are dominated by irregular structures (cf. figure 6.7). A microscopy picture of the tilted second inner groove is shown in figure 6.7.

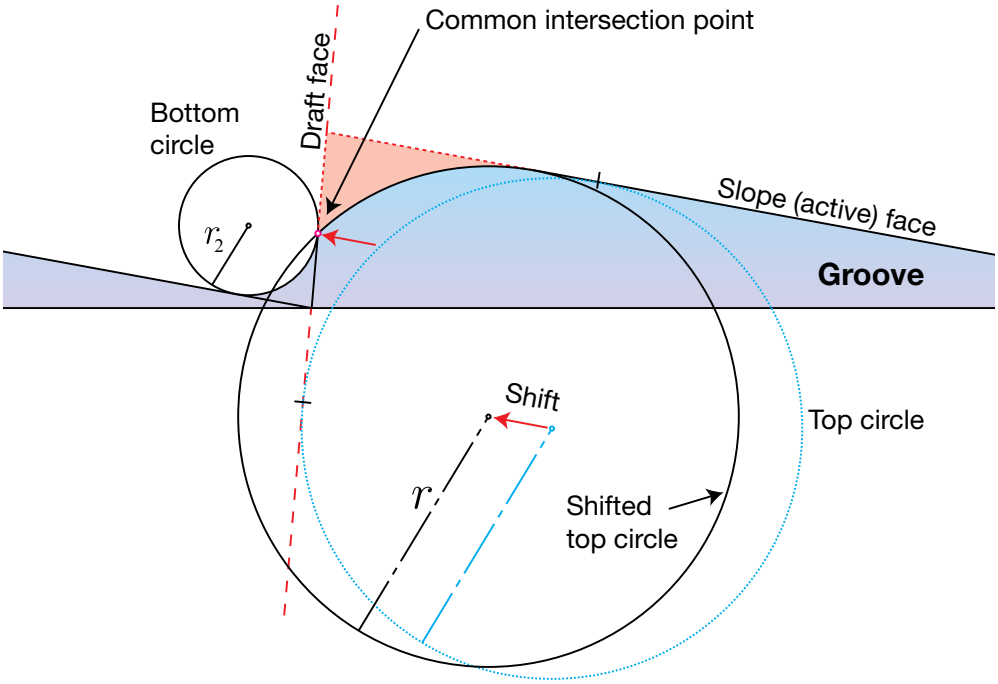

Figure 6.6: Cross section of an inner groove of the simulated lens. The groove height is smaller than the rounding radius. To create the groove connection, the top circle (blue) is shifted to a common intersection point with the bottom circle and the draft face.

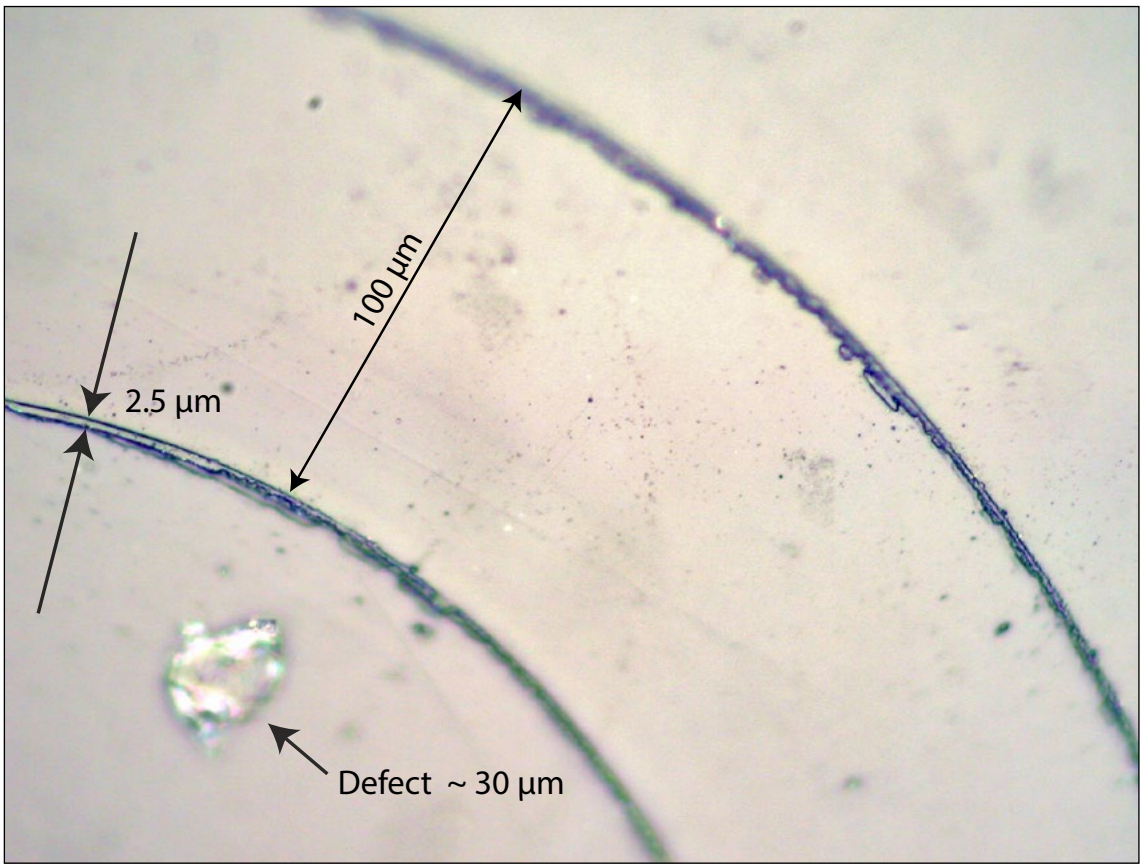

Figure 6.7: Microscopy picture of the slightly tilted Fresnel lens of FAMOUS. The second inner groove and its transitions to the previous and next groove are shown. A defect of approx. 30 µm is also visible.

6.2 Wave characteristics of photons

In section 4.2.3, the diffraction of a Fresnel lens is discussed. This effect must not be neglected in a simulation of a Fresnel lens, since its influence on the aberration radius R90 is of the order of one millimeter.

In the ray tracing simulation of the Fresnel lens, photons are treated as particles and the wave characteristics are not considered. For that reason, the simulated PSFs $D(x,y)$ are convoluted with the Fresnel diffraction pattern $I(r)$ with $r = \sqrt{a^2 + b^2}$ as derived in section 4.2.3 for photons with 550 nm wavelength (cf. section 5.1) [36]

$$(I * D)(x, y) = \sum_{a,b} I(a, b)\, D(x - a, y - b) \tag{32}$$

with the aim to approximately include the effect of diffraction. The coordinates x and y represent the bin or pixel position of the PSF, while the coordinates a and b represent the position of a value of the Fresnel diffraction pattern with its center at (0,0). As illustrated in figure 6.8, the influence on the aberration radius for an incidence angle θ = 0° is noticeable, while the effect is nearly negligible for larger aberration radii.

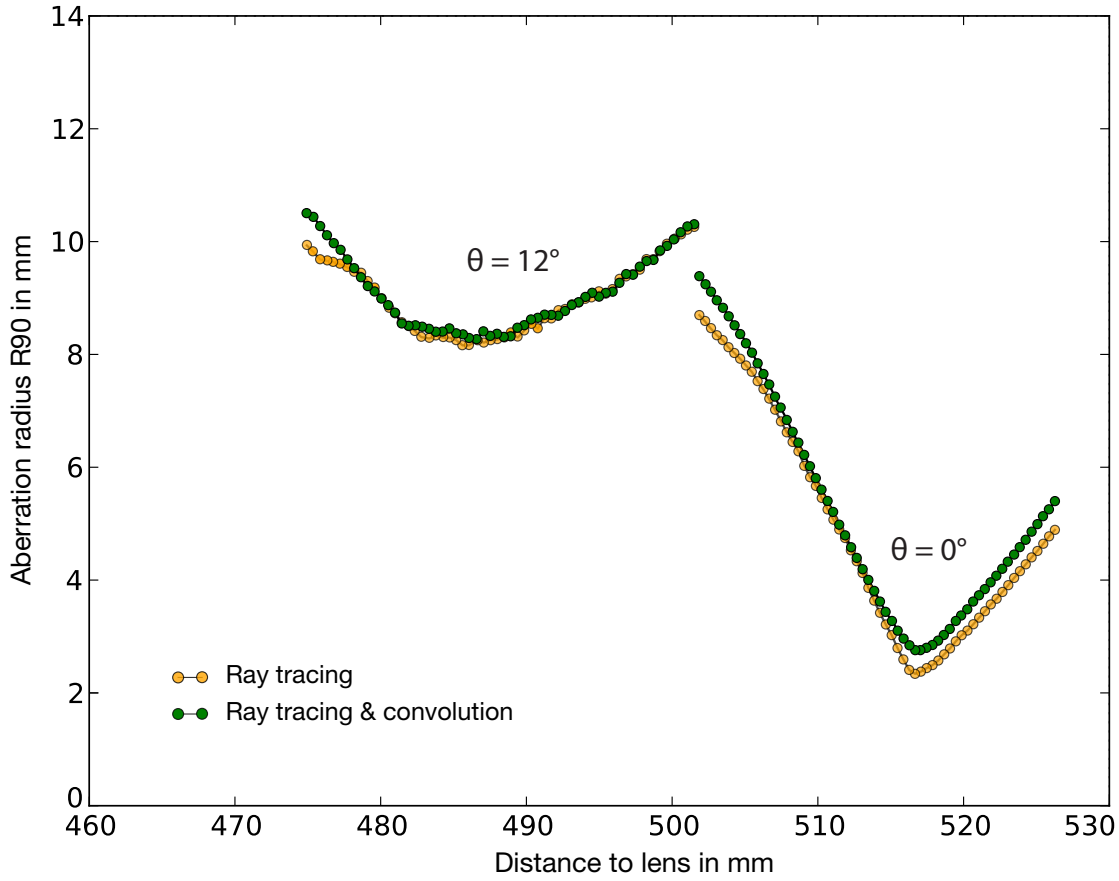

Figure 6.8: Simulated aberration radius as a function of distance to the Fresnel lens for different angles of incidence θ. The yellow graphs show the results of the ray tracing simulation while the green graphs include the convolution with the Fresnel diffraction pattern. Light of 550 nm wavelength is used.

7 Analysis framework

The main goal of the experiments is the measurement of size and position of the focal point and the transmittance of the Fresnel lens used for the fluorescence telescope FAMOUS. Therefore, the light formation of the lens in different scenarios is recorded with the image sensor of a Sony Nex-5 compact camera (section 5.3). To achieve a high quality and physically correct result, a dedicated measurement and analysis procedure is developed, which is presented in this chapter. At the beginning, the fundamental challenges of the correct measurement of light fluxes with a camera chip are discussed.

7.1 Brightness measurement with a camera CMOS chip

A picture of a digital camera is a two-dimensional array of typically a few million pixels. Each pixel usually consists of three colour values: red, green, blue (RGB), which are used to span an additive colour space and generate nearly every chromaticity visible to the human eye.

Based on this principle, images are digitised and processed by modern cameras and computers. Mostly differing in compression algorithms and quality, many file formats exist to save an image. The JPEG file format uses a maximum of $2^8 = 256$ luminance or brightness levels for each of the three colours, which can be expressed as a 8-digit binary number. Such an image has a colour depth of 8 bit.

An important property of nearly all file formats for images is the gamma encoding, which gives a relationship between the 256 binary levels and the actual luminance of the imaged scene. A camera sensor gives linear response to light levels, i.e. twice the number of photons result in twice the signal, while the human eye responds logarithmically.

As a consequence, linear brightness steps do not appear to be linear and the density of steps seems to increase for brighter tones (figure 7.1 bottom). To reduce the file size and to distribute the brightness steps homogeneously over the range of brightness, the steps are recalculated logarithmically to adapt the non-linear perception of light of the human eye.

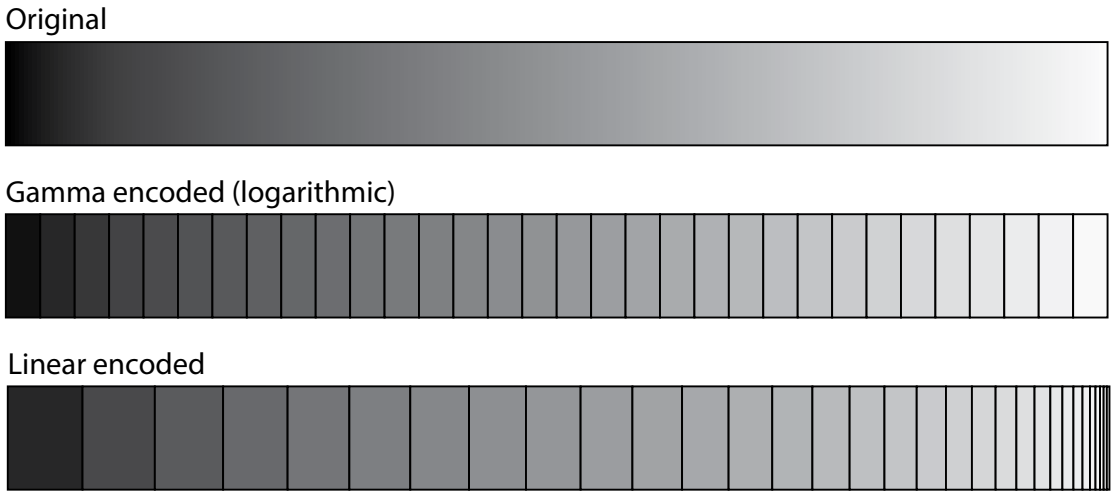

Figure 7.1: Comparison of a linear encoded brightness gradient to a gamma encoded brightness gradient. The brightness steps of the linear coding do not seem to be homogeneously distributed. Both gradients are encoded using 32 brightness levels (5 bit).

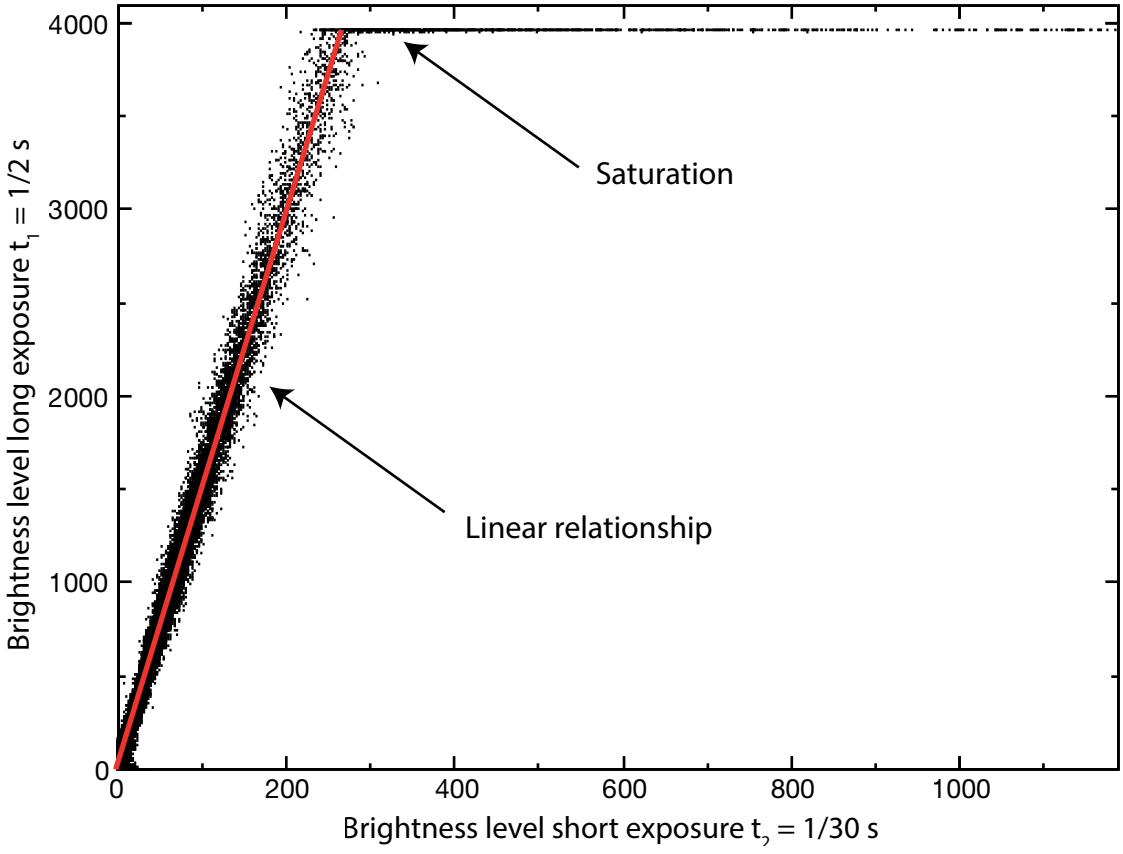

Figure 7.2: Two pictures of the same scene with two different exposure times t_1 = 1/2 s and t_2 = 1/30 s are taken with the Sony Nex-5. The two brightness values of each pixel are plotted against each other. At a brightness value of about 4000, the sensor becomes saturated which is visualised by a kink. A smaller range of brightness steps (0 - 1200) for the short exposure is shown on the x-axis for a better visualisation of the linear relationship between the brightness values of both pictures.

The gamma encoding is only one part of a series of image processing steps which are intended to enhance the image quality and accessibility in terms of art and visual appearance, but complicate or falsify the physically correct interpretation of the scene.

To avoid false interpretation of the brightness values, it is necessary to extract the linear sensor data before it is processed. This is possible by saving and reading all images with the camera raw format. To test the linearity of the extracted data, a scene is recorded using two different shutter speeds. The two different brightness values of each pixel position are then plotted against each other (figure 7.2). This is not a camera response curve, as both data sets are taken with the same camera chip, but it can still reveal non-linearities with the assumption that at least smaller segments of the data are recorded with linear response. By this means, the saturation of the long exposure picture becomes visible as a kink, which is expected to appear at a brightness level of about 4000 for a camera sensor with 12 bit = 4096 brightness levels. Apart from the saturation, this procedure shows a good linearity of the data.

7.2 Bayer pattern

The sensor cell of each pixel of a CMOS chip, which is used in the Sony Nex-5, is only sensitive to luminance and not to chrominance. To still enable a separation in RGB colours, each cell is coated with a filter, to record only one of the three colours.

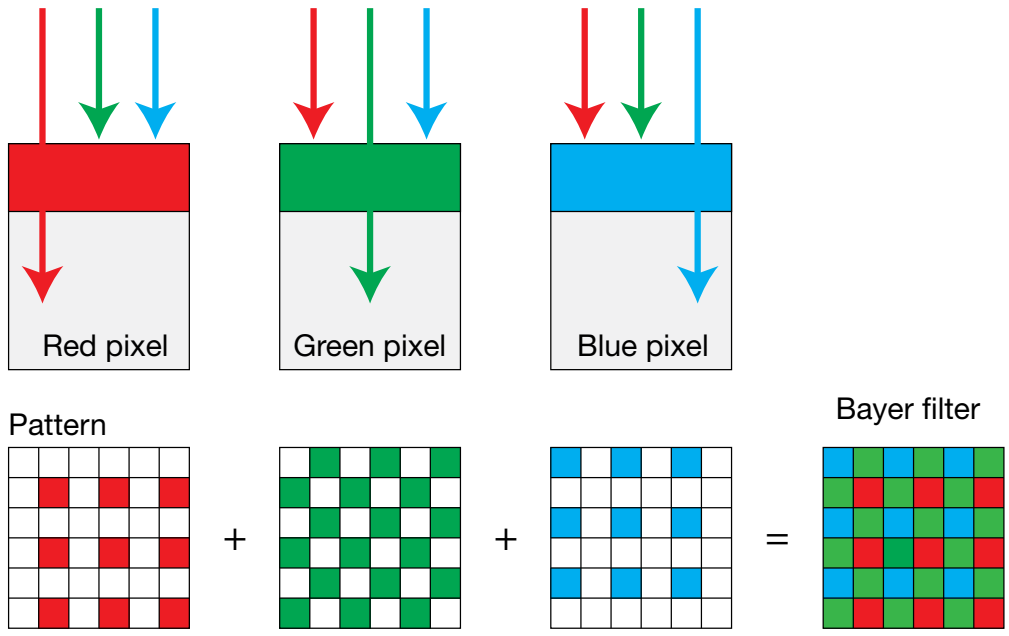

Figure 7.3: Construction of a Bayer filter mosaic. Each pixel is filtered to record only one colour. The green colour is privileged due to its high importance to the human perception of sharpness.

The three different pixels, i.e. different colour filters, are arranged in a Bayer pattern forming a Bayer filter mosaic [37], which describes the allocation of red, green and blue pixels on a square surface as shown in figure 7.3. The green pixels take 50 % of the total area while red and blue share the remaining portion in equal parts (25 % each). The special partitioning is again motivated by the human eye: it is most sensitive for green light, so the green pixels are privileged [38].

As the measured luminance values of an image taken in the experiment have to be comparable, the linear sensor data of only one of the three colour channels is extracted and used for the analysis. To achieve the best possible resolution for the measurement of the aberration radius of the focal point of the Fresnel lens, a green LED is used and the corresponding green colour channel is chosen for extraction.

To enable an uncomplicated handling for further procession steps, the resulting mosaic picture is demosaiced with the LibRaw-demosaic-pack-GPL2-0.14.8 [39], filling the positions of the red and blue pixels with interpolated green colour values.

7.3 Dynamic range

In general, the dynamic range describes the ratio between maximum and minimum value of a variable quantity, which is the light intensity in case of an image sensor (cf. figure 7.4). It can also be expressed as a base-2 logarithmic value known as f-stops or exposure values (eV).

The upper limit of light intensity which can be measured by a CMOS or CCD sensor mostly depends on the size of its pixels and the quality of their readout electronics. Incoming photons are converted into electrons by means of the photoelectric effect, which induces an electric field. A pixel of a modern CMOS or CCD chip can store nearly 10^5 electrons [40]. If this limit is exceeded, the pixel is saturated due to technical problems caused by high electrical fields.

The lowest light intensity which can be measured by a camera chip (black point) is defined by the darkest light values, that can be distinguished from the total noise, composed of several effects, e.g. the thermal noise of the sensor. Despite the fact, that every electrical signal is accompanied by noise, it is practically nonexistent, if the signal to noise ratio is high enough. To reduce the noise of the amplifier to a minimum, the lowest (native) signal amplification ISO-100 is chosen for all experiments.

The measured and amplified data of the image sensor is translated into discrete numerical values by an analog to digital converter (ADC). The ADC of the Sony Nex-5 divides the light intensity range with a precision of 12 bit, which means that $2^{12} = 4096$ brightness levels are used. Theoretically, the smallest light portion can be doubled 12 times (12 f-stops), and the sensor is still able to detect it. In practice, the black point is not clearly defined as it depends on quality criteria which tones are too noisy and need to be rejected.

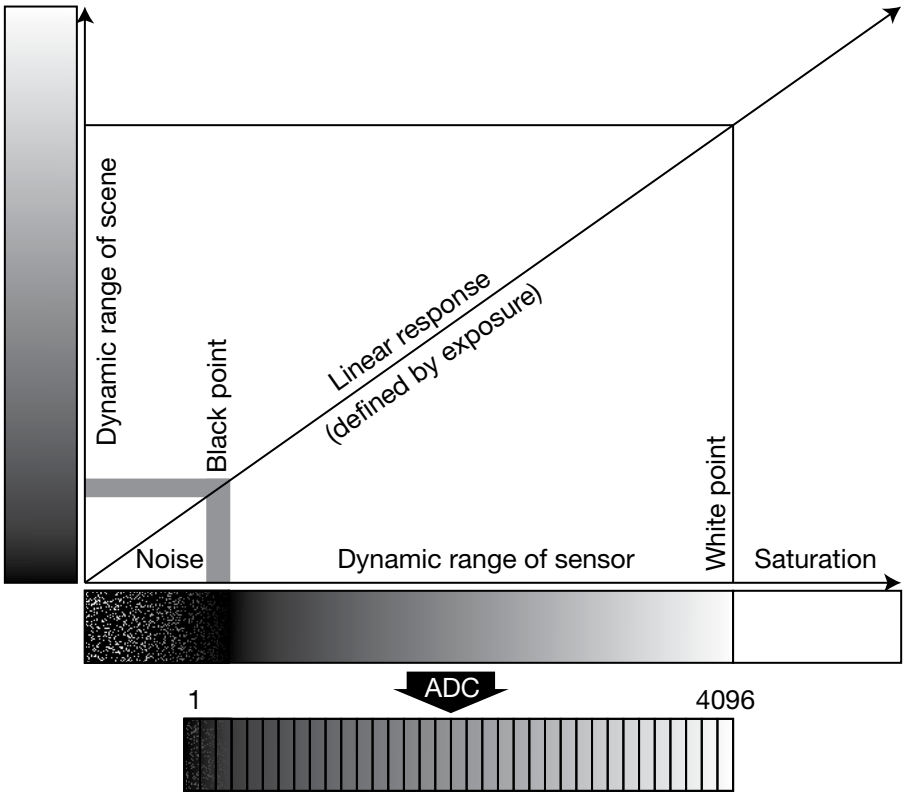

Figure 7.4: The dynamic range of a scene is translated to the dynamic range of an image sensor. The white point is defined by the saturation of pixels while the black point is not clearly defined, as it depends on the needed signal to noise ratio.

External reviews of the Sony Nex-5 show, that the theoretical dynamic range of 12 f-stops is nearly completely usable (11.9 f-stops), if a relative noise with a RMS of 1 f-stop is accepted [41].

7.3.1 High Dynamic Range Feature

First test measurements of the focal area of the Fresnel lens of FAMOUS show that its dynamic range exceeds the dynamic range of about 12 f-stops of the Sony Nex-5. The brightest point is over 30.000 times brighter as the darkest parts of the “tail” of the intensity distribution. As already seen for the Airy pattern, the aberration radius R90 is extremely sensitive to the outer regions with higher radial distance to the center of the distribution. For this reason, it is important to distinguish brightness steps over a great brightness spectrum.

To achieve this, a high dynamic range (HDR) image is created by merging two images with different exposure times (see figure 7.5). A picture with twice the exposure time collects twice the number of photons. Therefore, a linear relationship exists between the two pictures.

The picture with long exposure time t_1 is taken to map the faint parts of the focal point on the dynamic range of the camera chip. The inner, brighter part of this image is saturated. The second image with shorter exposure time t_2 maps the bright part of the image on the dynamic range of the chip, which was saturated in the first picture.

To merge both images, each pixel of the picture with long exposure is tested for saturation. If its value exceeds 3500, the pixel value of the picture with short saturation is taken instead and multiplied by the quotient of the two exposure times $v = t_1/t_2$.

The maximum dynamic range of the resulting image depends on the used shutter speeds and can contain a brightness range of over 18 f-stops. The procedure is expandable to many photos, but for the described experiment, two photos with $t_1 = 1/5$ s and $t_2 = 1/50$ s are sufficient. The resolution of brightness is not constant for the resulting high dynamic range photo, as the brightness step length for the short exposure picture changed in

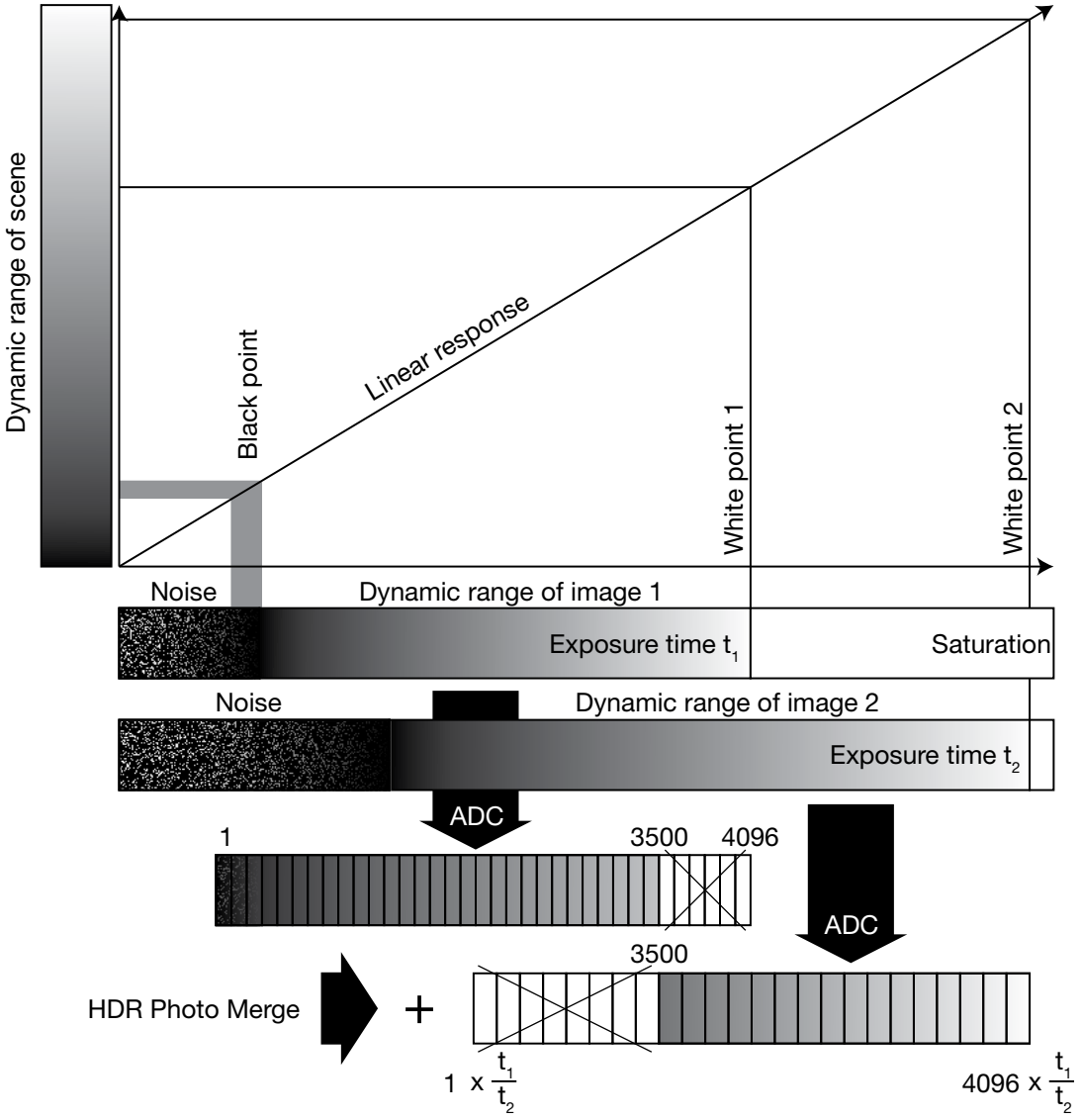

Figure 7.5: The dynamic range of a scene is recorded two times with different exposure times $t_1 = 1/5$ s and $t_2 = 1/50$ s. The resulting pictures contain different parts of the original dynamic range and can be merged to a HDR photo.

comparison to the long exposure picture. The profile of the recorded light intensity of the focal point with two exposure times is shown in figure 7.6 and the profile of the resulting high dynamic range image with background subtraction is shown in figure 7.7.

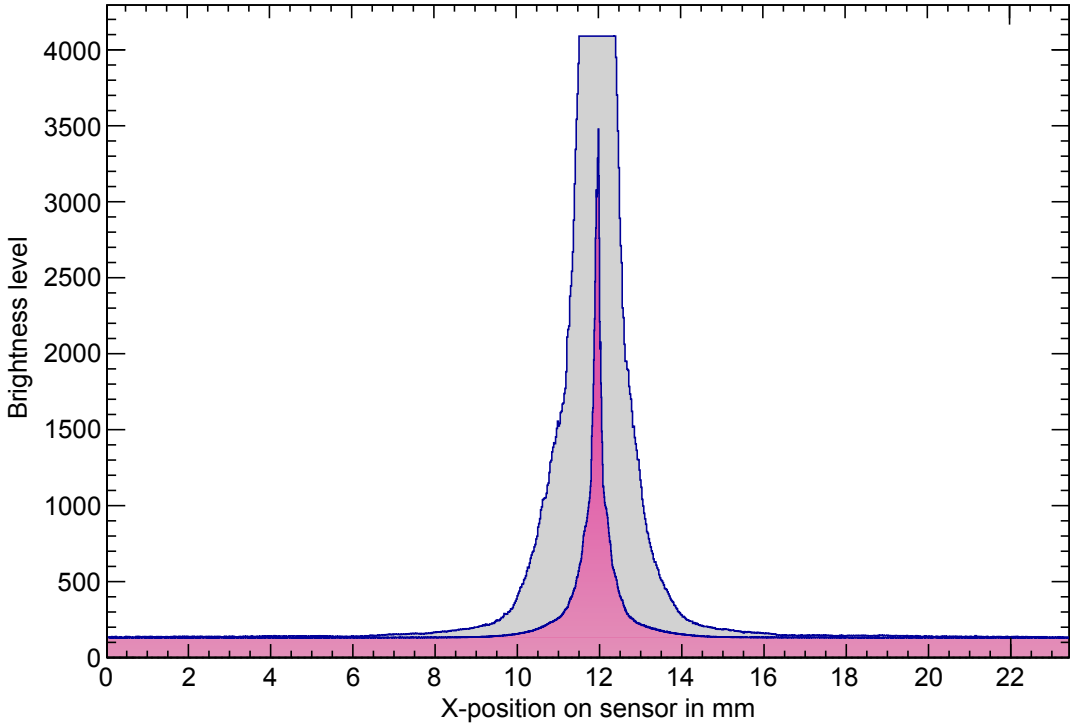

Figure 7.6: Profile of long exposure image (grey) and short exposure image (red) with background level.

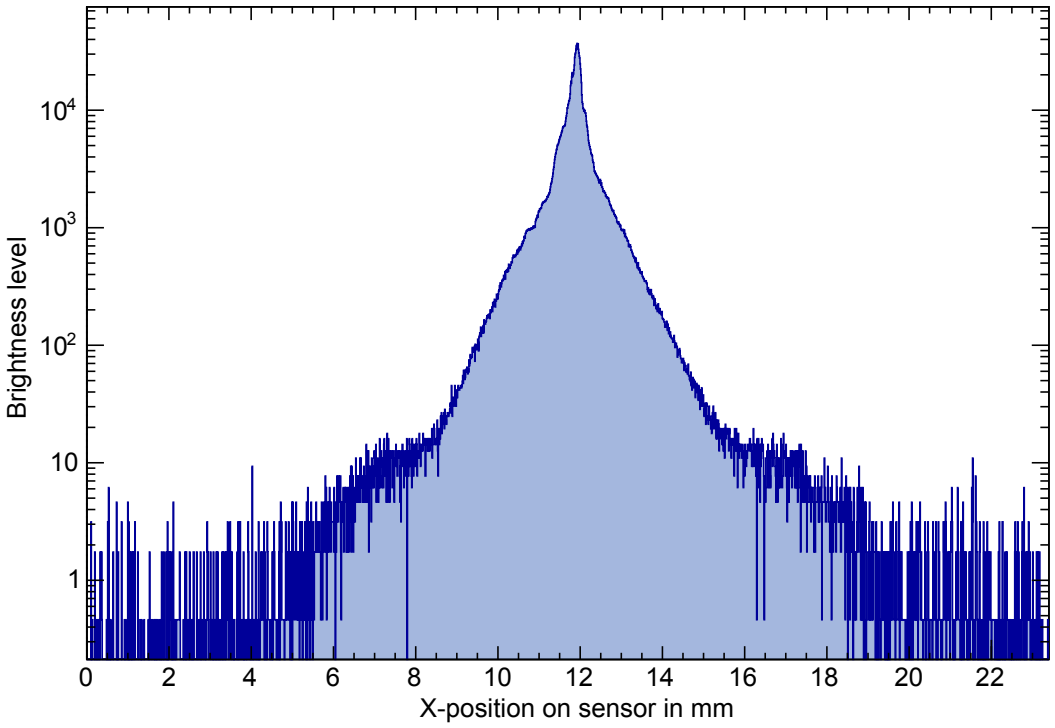

Figure 7.7: Profile of HDR image of FAMOUS focal region. The background is subtracted as described in the next section.

7.4 Background subtraction

The measurement of a signal is always accompanied by noise, which has to be subtracted. For the measurement of the focal point of the Fresnel lens with the CMOS sensor of the Sony Nex-5, different noise sources contribute:

Background light sources

The dark room is prepared to be as dark as possible. However some very faint light sources can still be present as the room is not intended for this purpose. If these light spots are present, it is assumed that they remain constant in time and position and can be recorded by a background image - a picture taken while the light source is switched off. The background image is subtracted from the picture containing the signal with the aim to subtract the false light sources.

Statistical sensor noise

As the sensor is an electronic device, typical statistical fluctuations caused by thermal influences are wrongly interpreted as signal. As each pixel is a counting experiment with positive counting range and poissonian uncertainty, absolute darkness may result in a variation of positive numbers with an average of a positive number while the right value should be exactly zero. The mean intensity of the fluctuation is relatively small compared to the complete counting range (factor 10^{-3}), but has noticeable influence on the final result, as all pixel values are integrated to calculate the aberration radius R90.

This effect is reduced by the background image subtraction, as similar poissonian fluctuations are present in both images. The result after subtraction is illustrated in figure 7.8. More details on this effect are discussed in section 7.4.1.

Hot pixels

Some pixels of the camera chip produce systematically more noise than most others. These pixels are called “hot pixels” and can also be removed partially by background image subtraction.

Amplifier noise

The amplifier of the camera introduces additional statistical fluctuations, which are treated as the statistical noise.

Reflections of light source

The reflections of the point light source at side walls and the ceiling are minimised (see section 5.2), but even the fixture of the Fresnel lens leads to unwanted reflections which can not be avoided. The influence of this effect is estimated as negligible by visual inspection of the resulting images as no expected deviating structure from a circular point spread function is spotted.

7.4.1 Offset Correction

As described in the previous section, the offset due to poissonian fluctuation of the sensor and the amplifier is reduced by background image subtraction (image A - image B = image C). The subtraction leads to statistical fluctuations (in image C) with a mean value of zero (on outer parts of the sensor which are not illuminated), if the poisson fluctuation for the background image (image B) and signal image (image A) are equal.

However, an analysis of the resulting image (image C) after subtraction of the background image (image B) shows statistical fluctuations with a mean value which is not zero, as illustrated in figure 7.8.

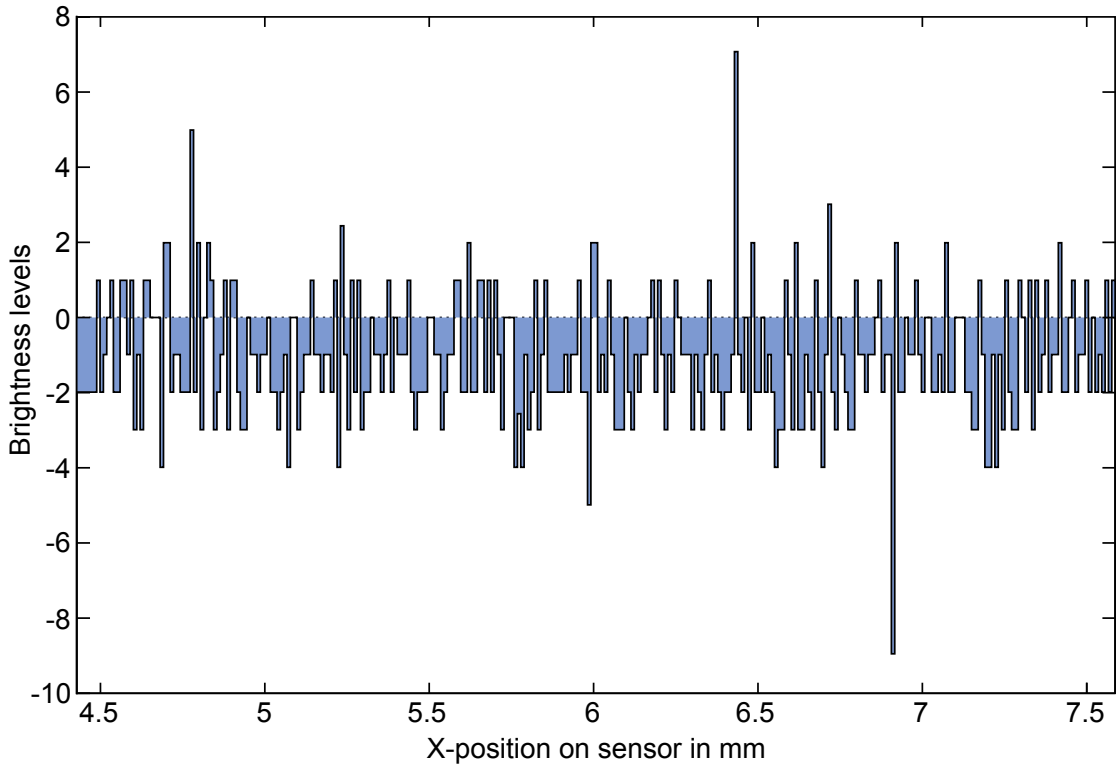

Figure 7.8: Row of pixels of the resulting image (image C) after background image subtraction of a region of the sensor which is not illuminated. The mean value of the fluctuation is -0.95 with standard deviation σ = 1.24.

To eliminate the offset, a location on the resulting image (image C) of the outer region of the sensor can be defined to calculate the mean value of the fluctuation and subtract it from the resulting image (image C - mean = image D). The result (image D) is shown in figure 7.9. In figure 7.10, the aberration radius R90 is plotted as a function of the distance to the lens. The line with blue dots represents the development of the aberration radius without additional subtraction of the offset (image C) as described in this section, which results in noticeable steps. The line with red dots represents the same series of measurements while the offset subtraction is performed (image D).

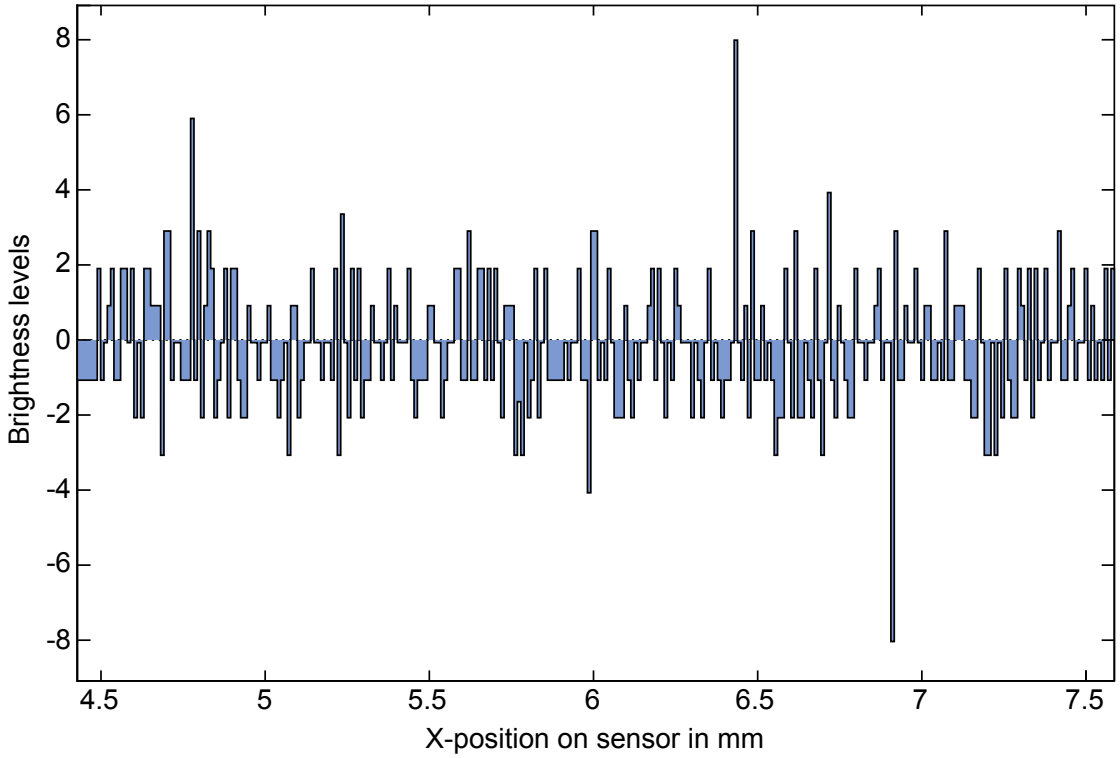

Figure 7.9: Row of pixels of figure 7.8 after offset subtraction (image D). The mean of the fluctuation is 0.

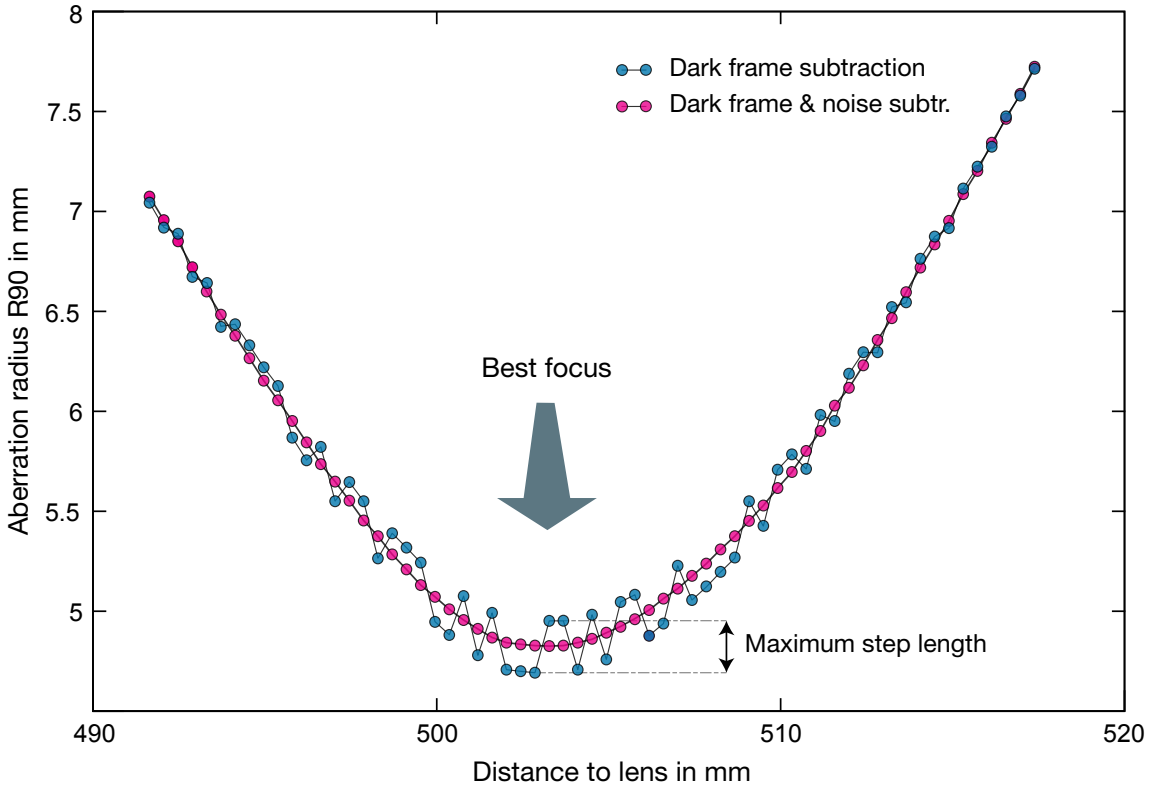

Figure 7.10: Aberration radius for an incidence angle of θ = 6° as function of distance to the lens along z. The results after background image subtraction are presented as blue dotted line, while the results with additional noise subtraction are plotted as red dotted line.

7.5 Image Compilation

The focal point for off-axis image points with an incidence angle on the Fresnel lens of more than $\theta = 8°$ exceeds an aberration radius of 7 mm for best focus. As the aberration radius will further increase up to $\theta = 12°$ and it is also desirable to study the aberration radius for small deviations from best focus, the height of the camera chip of 15.6 mm is not sufficient.

To solve this problem, the analysis software is equipped with an algorithm to combine two locally shifted high dynamic range pictures to one image (see figure 7.11). Each of the two pictures has to contain the maximum of the focal point, to determine the relative shift of the two pictures. One image contains the upper part of the recorded focal point, the other contains the bottom part. The combined image has a height H of typically 25 mm and a width W of 22.3 mm which equals the width w_1 and w_2 of the single images, i.e. the horizontal shift is zero in most cases. The image compilation is performed for the measurement of the aberration radius of the focal point for an incidence angle of incoming light on the Fresnel lens of $\theta = 6°$ and larger.

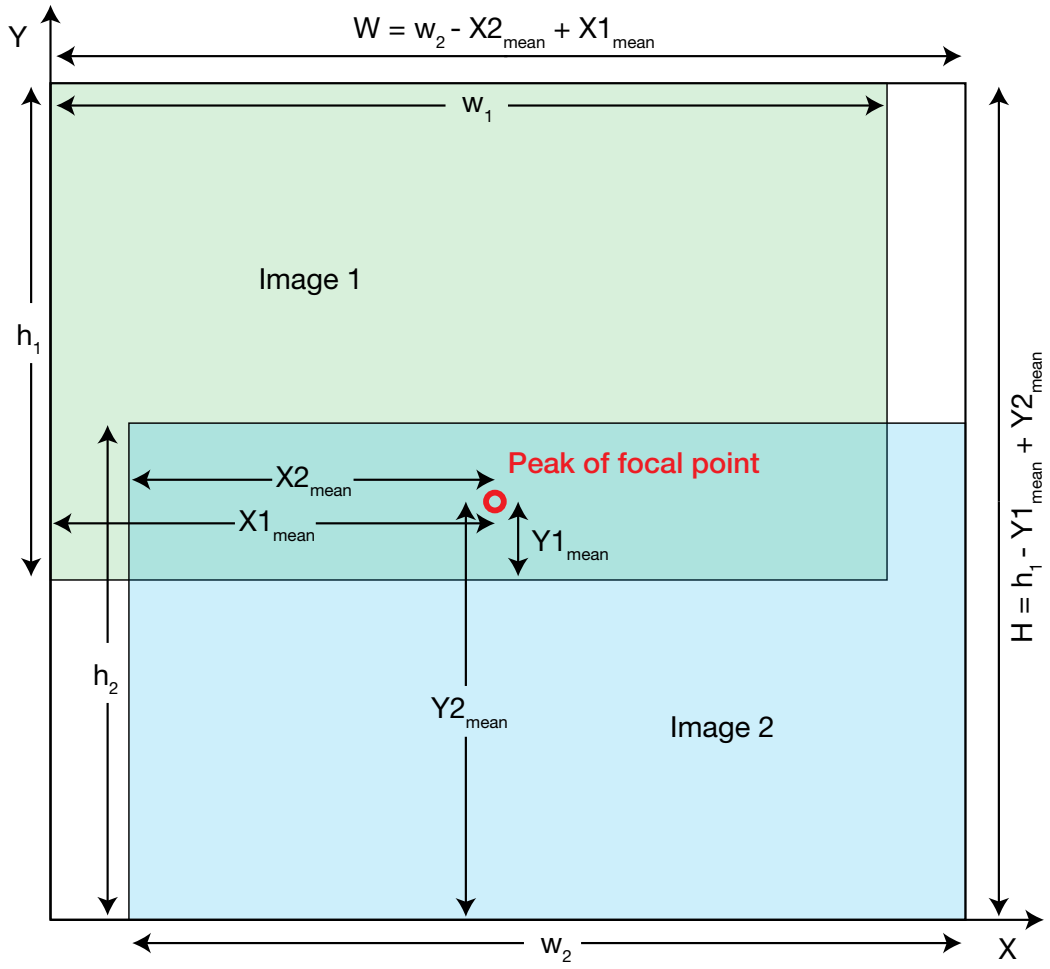

Figure 7.11: Schematic of image compilation. The maximum intensity of the focal point serves as indicator for the relative shift of the two pictures. The total width W and height H of the combined image for instance, can be calculated as shown in the illustration.

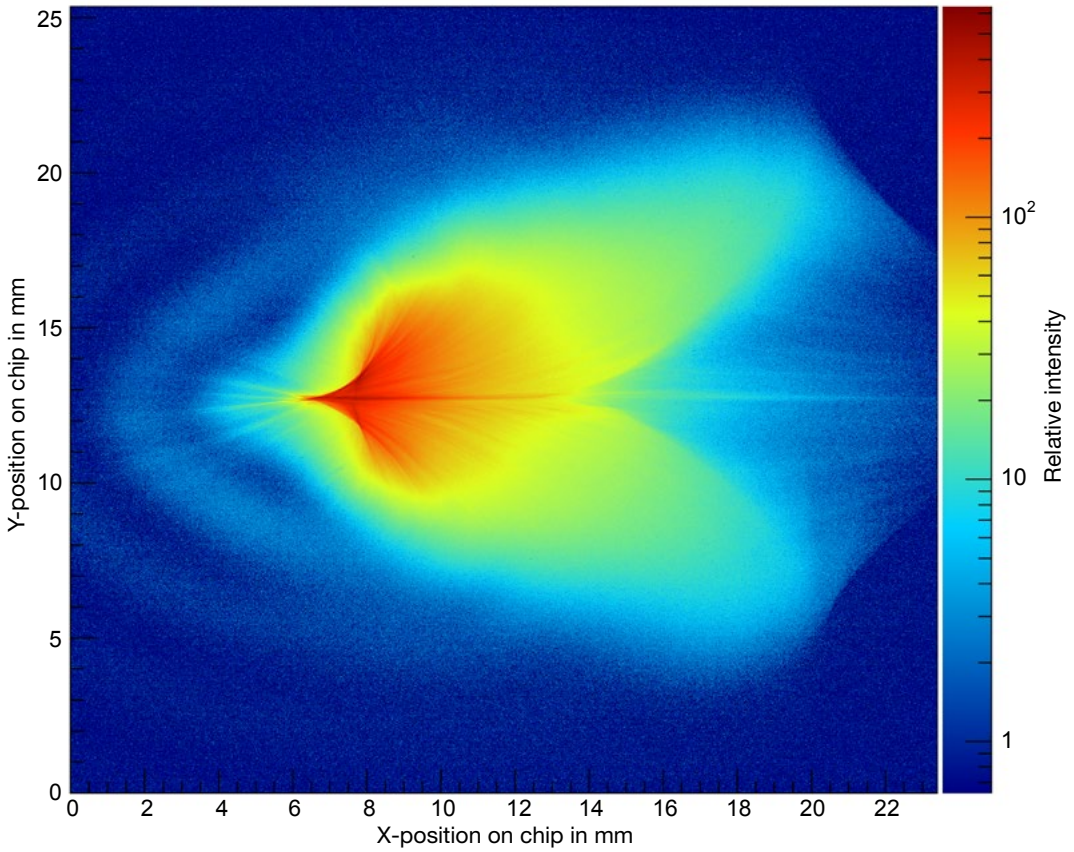

Figure 7.12: Measured best focus point spread function for an incidence angle on the Fresnel lens of θ = 10°.

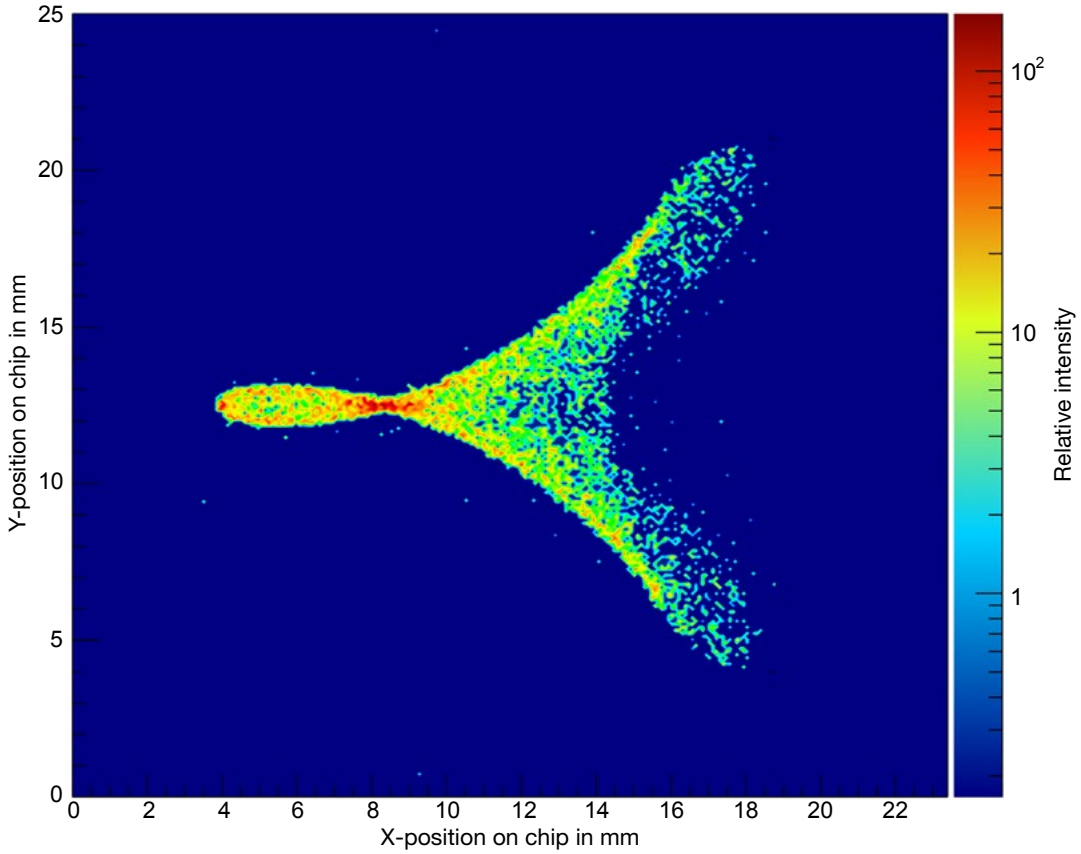

Figure 7.13: Simulated best focus point spread function for an incidence angle on the Fresnel lens of θ = 10°.

The algorithm does not use any functionality to smooth the transition between both pictures. The pictures are cut horizontally at the common location of maximum intensity and arranged vertically.

The high quality of the final image (e.g. figure 7.12) is a feedback of a good reproducibility of the measurement as well as all earlier performed image processing steps (background image subtraction, high dynamic range merge, noise subtraction), as the "top" images and "bottom" images are taken in individual, independent series of measurements. The most important parts of the complete process chain is illustrated in figure 7.14. For a comparison with the measurement, the simulated best focus PSF for an angle of incidence of $\theta = 10°$ is shown in figure 7.13.

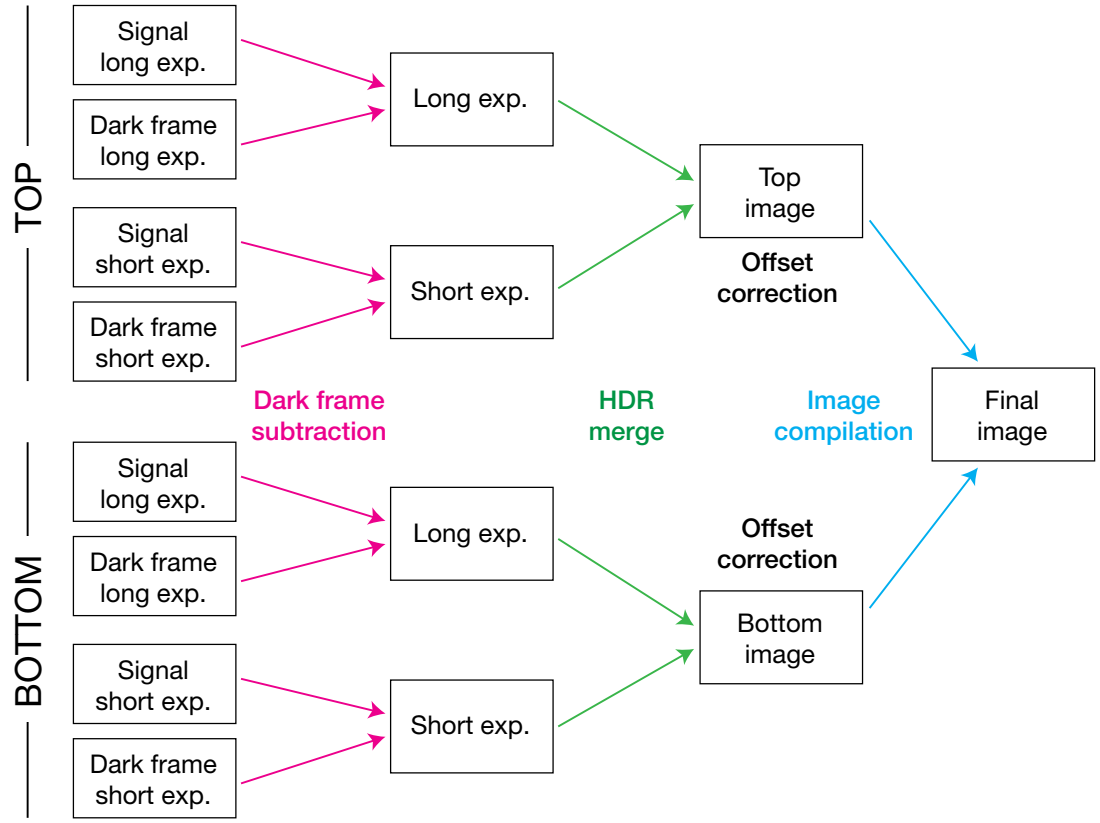

Figure 7.14: Schematic of the most important steps of image processing. Each data point consists of up to 8 images.

8 Aberration radius and best focus

In this chapter, the results concerning size and position of the focal point of the Fresnel lens of FAMOUS are presented. The experimental setup and optical components, presented in chapter 5, are used to measure the focal point for different incidence angles of the light on the Fresnel lens. The necessary data are recorded and processed as described in chapter 7. The explicit procedure of the measurement is explained in the following section.

8.1 Measurement of the aberration radius

After the LED of the point light source is switched on, and a minimum waiting time of 15 minutes for a stable temperature and light intensity of the LED (see also section 5.1), the test bench is adjusted for the desired incidence angle as described in section 5.4 and the camera including x-y-table is visually positioned to the best focus point of the lens with the help of the preview monitor of the camera. The sliding range of the table along the optical axis (z-axis) is adjusted to give a certain path length forward and backward (towards the lens) relative to the best focus point (see figure 8.1).

As the sliding range of the table is limited to 25 mm, and manual repositioning of the table within a series of measurements is not an option due to precision problems, the portion of the sliding range which is used forward and backward (towards the lens) from best focus along the optical axis has to be well chosen. The ideal image plane of the Fresnel lens is expected to be curved as described by Petzval field curvature (cf. section 4.1.3.4), which means the focal length reduces with incidence angle θ. As the aberration radius of the point spread function at a given distance to the lens for different incidence angles needs to be compared, the sliding ranges for different incidence angles need to overlap as illustrated in figure 8.1. However, the total overlapping for all cases is not possible and the desired position of best focus for higher incident angles is difficult to find as the visual estimation of the point of best focus becomes nontrivial due to varying shapes of the point spread function (e.g. figure 7.12).

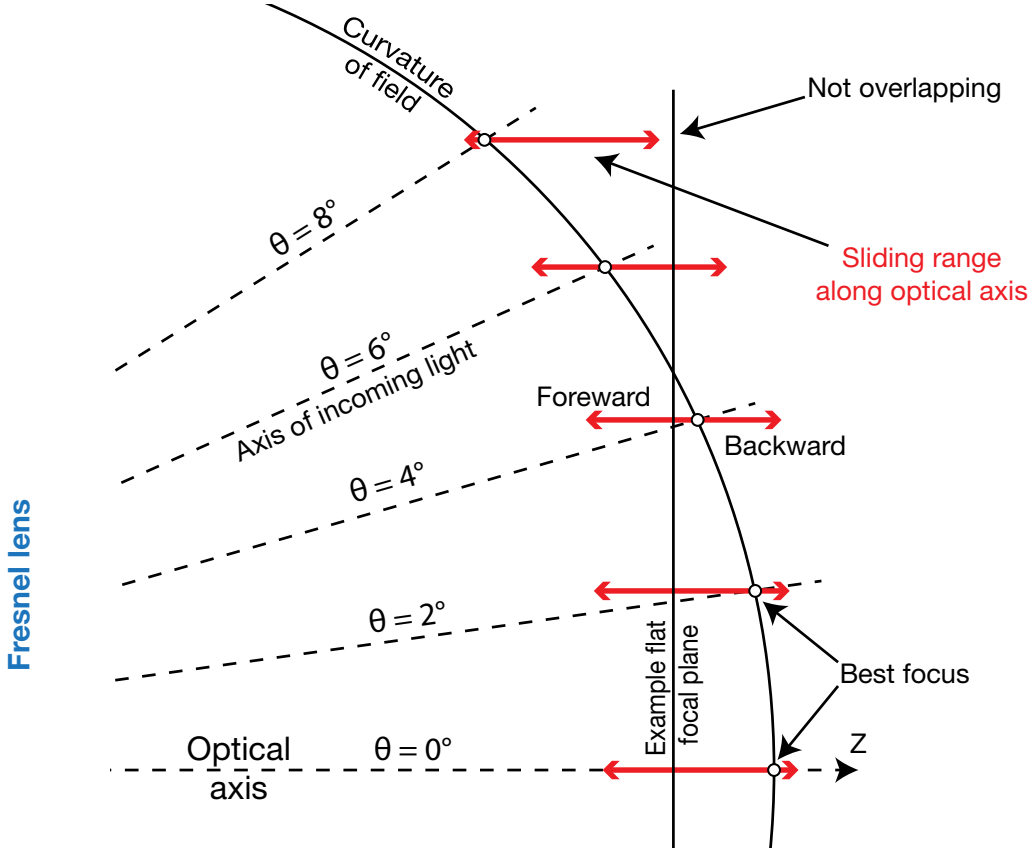

Figure 8.1: Top view on the curved image plane of the Fresnel lens. The sliding range of the z-table defines the measurement range of the focal point for each incidence angle and needs to be adjusted to overlap with the range of the other angles of incidence. Proportions and angles are not drawn to scale.

After positioning of camera and table, the sliding range is sampled in 0.4 mm steps, beginning at the largest distance to the lens. For $\theta > 0$, the position of the camera is also corrected along the x-axis, perpendicular to the optical axis in each step, as the center of the point spread function moves along the axis of incoming light.

At every position, two pictures of different exposure times are taken. The exposure times are chosen for the focal point for $\theta = 0°$ as this picture needs to have the largest dynamic range and are not changed for all series of measurements. For $\theta = 6°$ and higher, two series of measurements are performed for each angle, with the camera adjusted to different heights (top and bottom part of the point spread function, see section 6.5). The positive angles in the range from $\theta = 0°$ to $\theta = 12°$ is measured in 2° steps, as well as $\theta = -4°$ to verify rotational symmetry in direct comparison to $\theta = 4°$.

After each series of measurements, two different background images in the center of the sliding range are taken with previously defined exposure times, which are used for the background image subtraction of every corresponding image taken in this series.

8.2 Results of the measurement

The recorded data is processed using the analysis framework which is presented in chapter 7. The final image of each position is transformed to cylindrical coordinates. The center of the coordinate system is placed to the center of gravity[4] of the recorded point spread function. After that, the light intensity values of all pixels are integrated radially from the center. The radius of 90 % of the total integrated intensity defines the aberration radius R90. Theoretically, this is the same concept as used to describe the aberration radius of the Airy pattern and Fresnel diffraction pattern (see sections 4.1.2 and 4.2.3), but practically, the integration range is limited to the size of the camera chip. To estimate the related error, different sensor sizes are implemented to the simulation of the Fresnel lens.

The aberration radius R90 as a function of the distance to the Fresnel lens along the optical axis (z-axis) for all positive angles of incidence θ are presented in figure 8.3. The distances of best focus are located up to 35 mm apart. The best focus for an incidence angle of θ = 12° has an aberration radius of R90 = 8.5 mm. The high dynamic range image of the point spread function for best focus and incidence angle θ = 0° is shown in figure 8.2. A circle with the aberration radius R90 = 2.89 mm is marked as dashed black line and compared to the circular entrance window with a radius r_W = 6.71 mm of a Winston cone which defines the pixel size of FAMOUS.

The distance to the Fresnel lens was measured with a relatively high systematic uncertainty of ± 3 mm for all points of measurement, which is due to the thickness of the lens and its inherent bending, resulting in different distances to the center of the lens and to its outer regions. This effect is discussed at the end of section 8.4. The statistical uncertainty on the aberration radius is negligible as the statistical fluctuation of ~ 10^6 pixels of the Sony Nex-5 is averaged on integration. This is confirmed by multiple measurements of the same spot with low fluctuations of the aberration radius of about 0.5 µm (cf. section 5.1, figure 5.6).

The total uncertainty on the aberration radius R90 is dominated by systematical uncertainties, which are introduced by the experimental setup, e.g. the angular scale to adjust the angle of incidence, the limited size of the image sensor, the bending of the Fresnel lens, and possibly other factors. In the following section, the systematical uncertainties are discussed and estimated with the help of the simulation of the Fresnel lens and the measurement of a conventional lens.

The results of the measurement show that the Fresnel lens fulfils the required qualifications in terms of imaging resolution. For the maximum angle of incidence of FAMOUS θ = ± 6°, the minimum aberration radius of R90 = 4.72 ± 0.13 (sys.) mm is measured and for θ = 0°, an aberration radius of R90 = 2.89 ± 0.13 (sys.) mm is measured. If a flat image plane is used, it should be placed in a distance of 505 mm to 507 mm, to accept a compromise between the aberration radii for the angles of incidence θ = 0° and θ = 6°. The maximum aberration radius in that case is estimated to be smaller than 5 mm, which is 25 % less than the entrance radius of r_W = 6.71 mm of the pixels of FAMOUS.

[4] The two dimensional intensity distribution is projected on the x-axis and y-axis and the mean x- and y-position of the corresponding projected histogram is calculated using the related intensity distribution as weighting function.

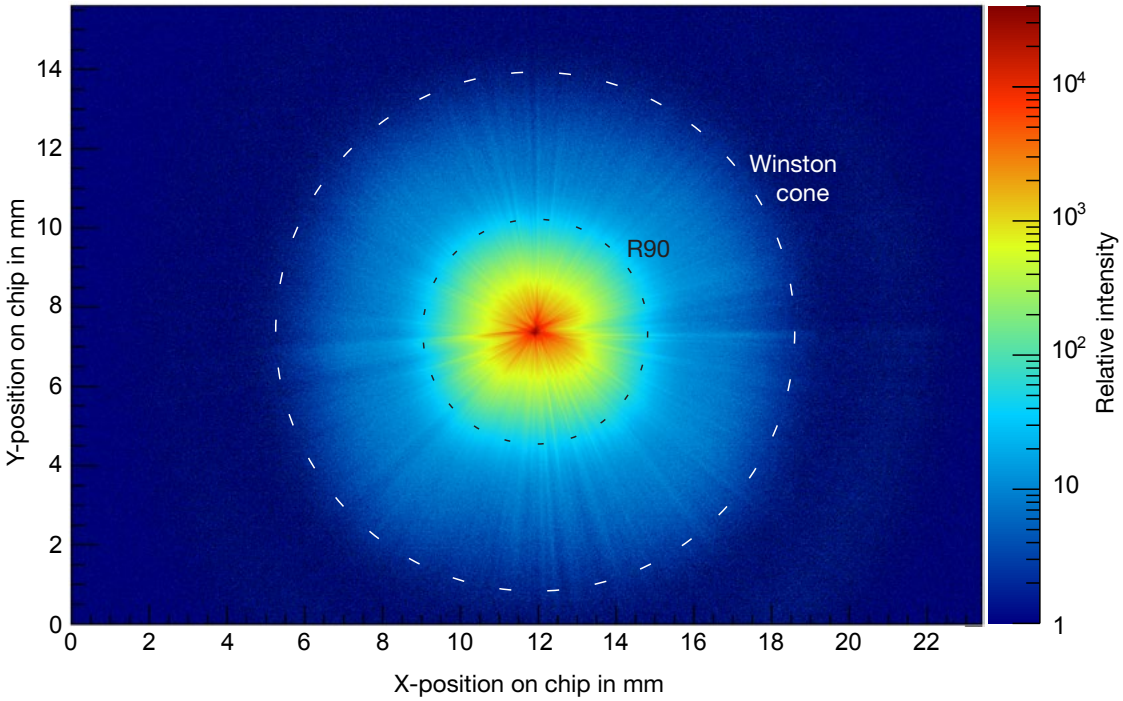

Figure 8.2: Measured best focus point spread function for an incidence angle on the Fresnel lens of θ = 0°. The black dashed line describes a circle with the aberration radius R90 = 2.89 mm while the white dashed line represents the circular entrance window of a Winston cone with radius r_w = 6.71 mm.

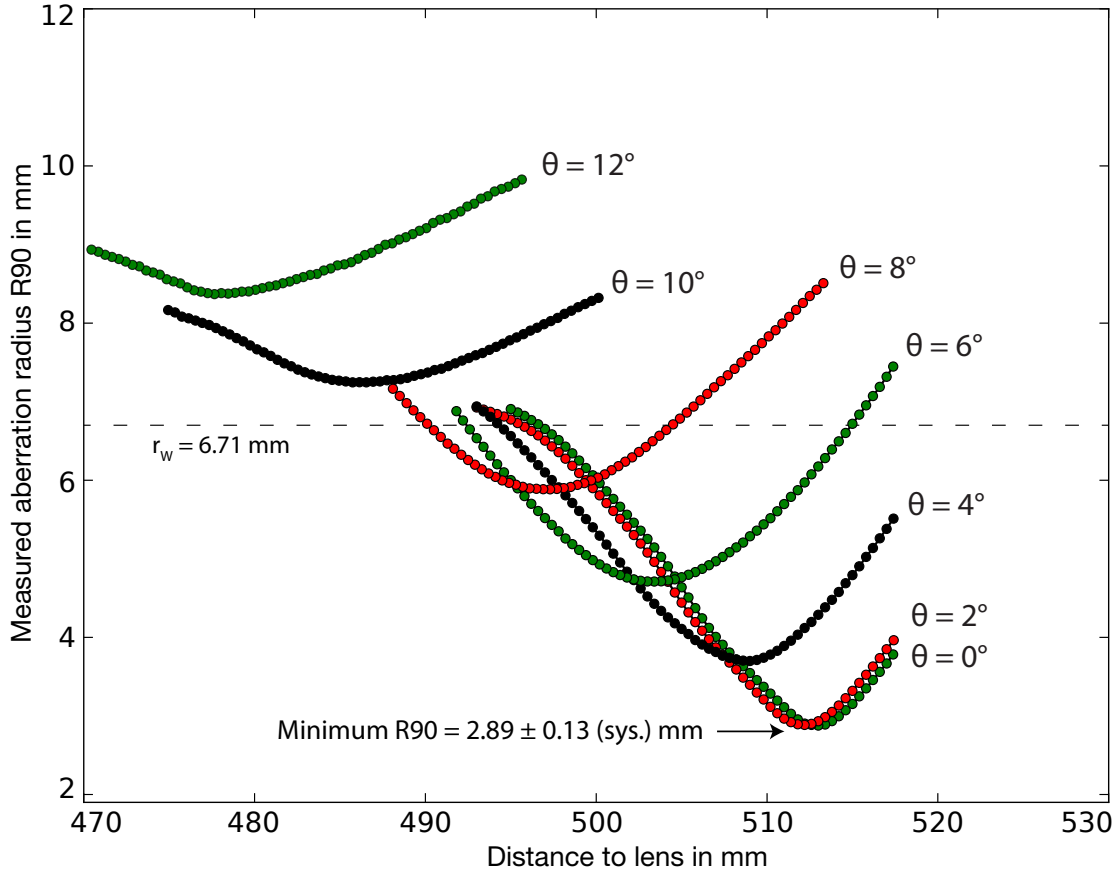

Figure 8.3: Measured aberration radius R90 in mm as a function of distance to the Fresnel lens along the optical axis in mm for different angles of incidence θ as marked by different colors. The radius of the entrance window of a Winston cone with radius r_w = 6.71 mm is marked as dashed line.

8.3 Results of the simulation

The simulation framework, which is introduced in chapter 6, is used to test the theoretical model of the Fresnel lens. To estimate the influence of a limited image sensor, two different sizes of sensor surfaces are implemented to the simulation: a large sensor surface of 100 x 100 mm^2 and a dynamic surface of 23.4 mm width and 15.6 mm height for incidence angles of θ = 0°, 2° and 4° as well as 25 mm height for θ = 6°, 8°, 10° and 12° to reproduce the situation of the measurement.

The position of the smaller sensor surface is chosen as the initial position of the camera in the experiment: The position of the center of gravity of the point spread function on the measured best focus image is taken to set the position of the small sensor surface relative to the center of gravity of the simulated point spread function on the large sensor surface. While shifting the sensor surfaces to different distances along the axis of incoming light (as shown in figure 6.1), the relative position of the small and large sensor surfaces remains constant.

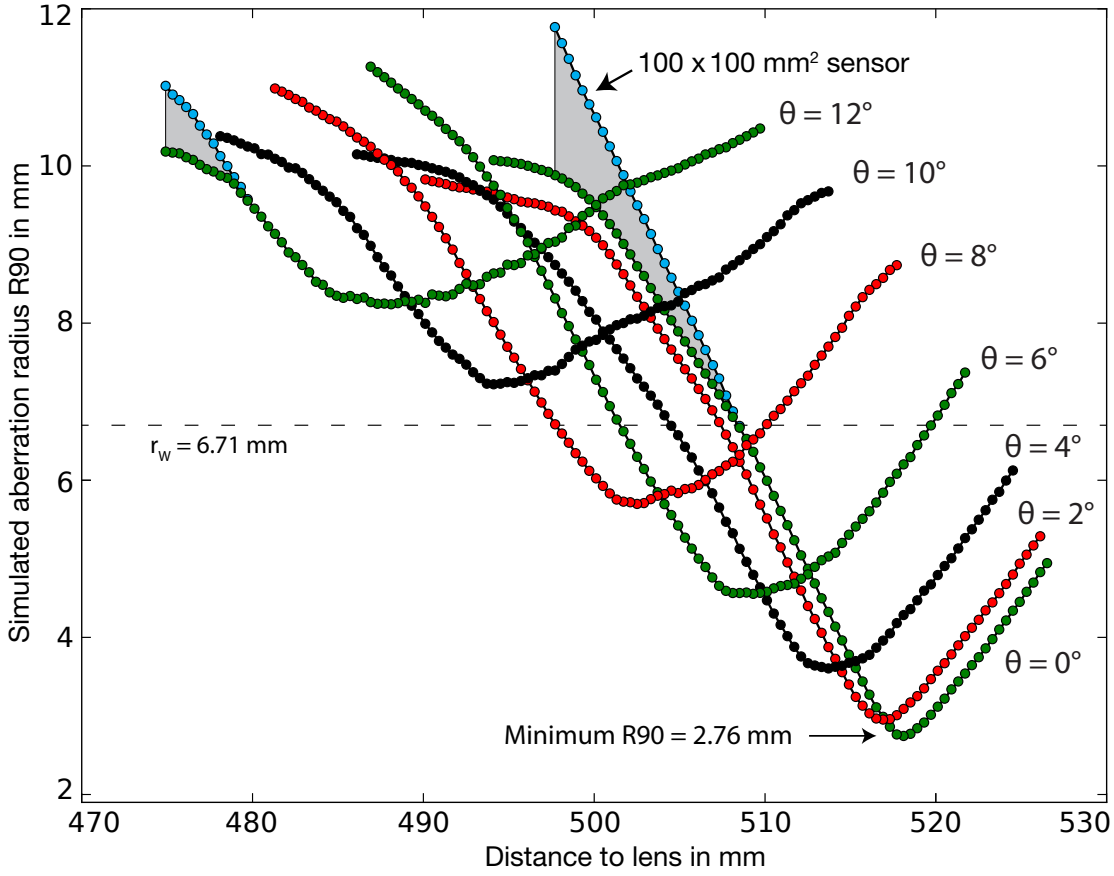

Figure 8.4: Simulated aberration radius R90 as a function of distance to the Fresnel lens along the optical axis for different angles of incidence θ as marked by different colors. The results for the large sensor surface are plotted for θ = 0° and θ = 12° (blue dotted lines) to reveal the influence of a limited sensor size. The radius of the entrance window of a Winston cone with radius r_w = 6.71 mm is marked as dashed line.

The simulated aberration radius as a function of the distance to the lens for the measured angles of incidence is shown in figure 8.4. The blue data points correspond to the aberration radii calculated on the large sensor surface as the other colored points are calculated for the smaller sensor which is comparable to the measurement.

For $\theta = 0°$, 2° and 4° the reduced height of the sensor surface starts to affect the results for aberration radii of 7 mm and above. The images with a height of 25 mm affect the aberration radius if it is larger than 10 mm. With the help of the simulation, the measured development of the point spread function for an unfocused focal point is better understood and the uncertainty can be estimated. The aberration radius for best focus is not affected by the limited sensor size.

The direct comparison of measurement and simulation shows that the measured focal points for all angles of incidence are systematically located closer to the lens than predicted by simulation. The differences are of the order of the systematical uncertainty on the measured distances, increasing for higher angles, as illustrated in figure 8.5. For an angle of incidence of $\theta = 0°$, the best focus aberration radius is simulated to R90 = 2.76 mm

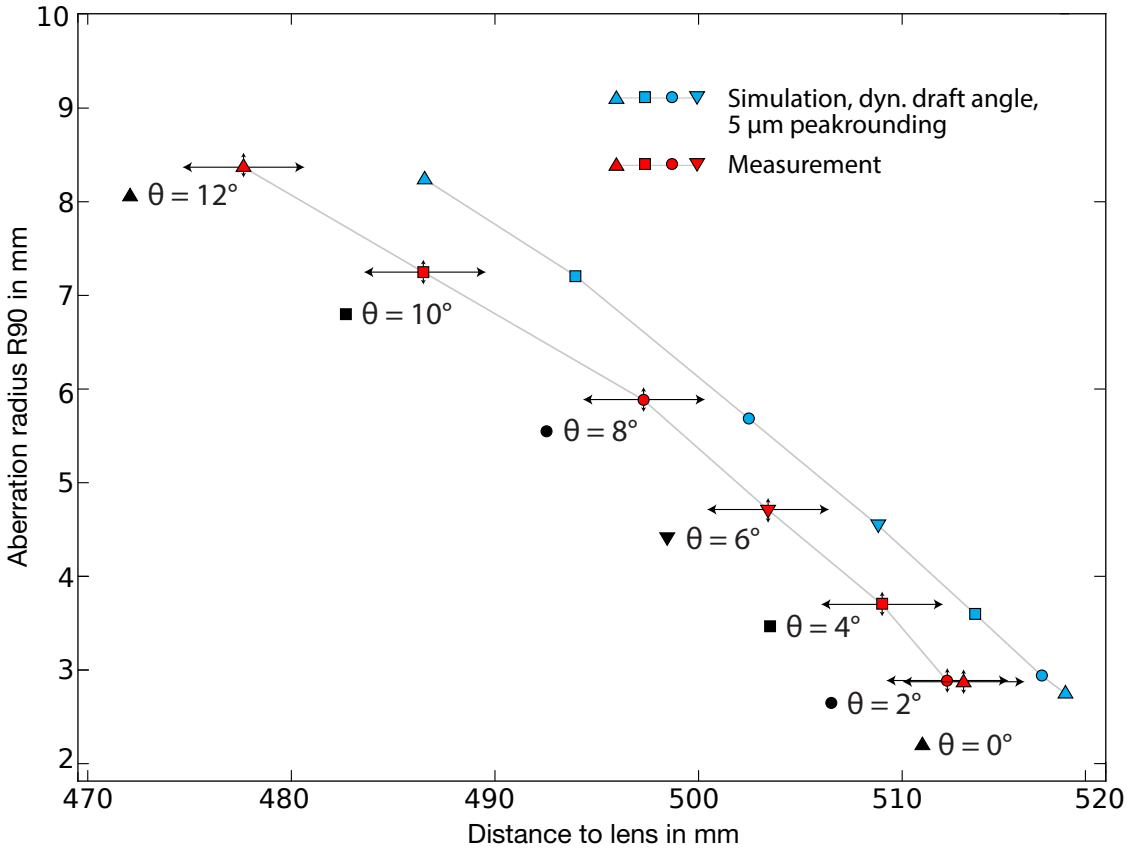

Figure 8.5: Comparison of measured and simulated best focus aberration radius as a function of distance to the Fresnel lens for multiple angles of incidence. The difference in focal length for each angle of incidence is of the order of the systematical uncertainty of 3 mm on the measured distance to the lens (horizontal arrows). The systematical uncertainty on the aberration radius of 0.13 mm (vertical arrows) is discussed in the following section.

The overall simulation nearly reproduces the measurement results. In particular, the best focus aberration radius R90 of measurement and simulation is in good agreement in most cases. However, the measured aberration radius for $\theta = 0°$ contradicts the expectation as it is similar to the measured aberration radius for $\theta = 2°$. This effect can be caused by two problems: a miss-alignment of the angular scale for the angle of incidence θ, or the whole test bench in relation to the point light source, as well as an aberrational effect caused by the bending of the Fresnel lens.

8.4 Alignment test and systematical uncertainty

To estimate the uncertainty on the angle of incidence, a series of measurements is performed for a negative angle of incidence $\theta = -4°$ which is compared to the measurement of $\theta = 4°$ in figure 8.6. The focal distance for $\theta = -4°$ is 0.4 mm shorter and the best focus aberration radius drops from R90 = 3.71 mm for $\theta = 4°$ to R90 = 3.67 mm for $\theta = -4°$.

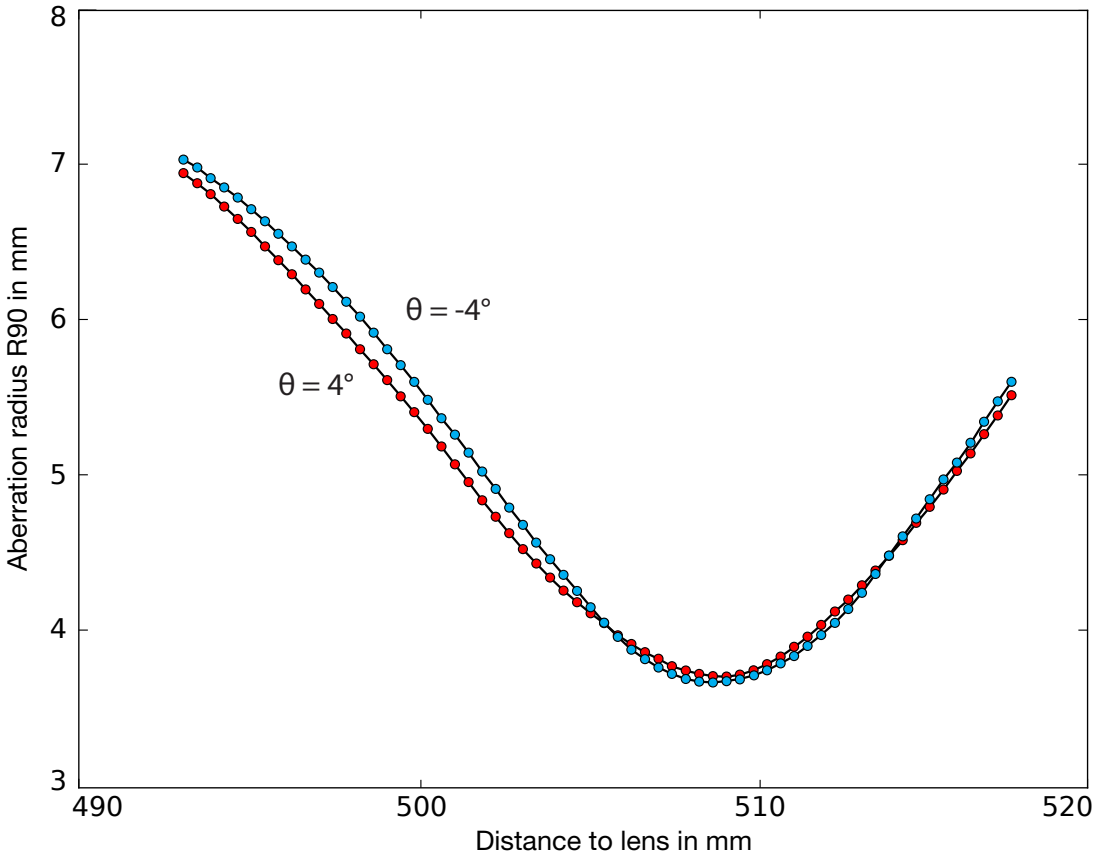

Figure 8.6: Comparison of measured aberration radius as a function of distance to the Fresnel lens for angles of incidence θ = 4° (red dotted line) and θ = -4° (blue dotted line). The focal distance for θ = -4° is slightly shorter.

With the collected information it is possible to visualise the curved focal plane of the Fresnel lens as shown in figure 8.7. According to section 4.1.3.4, the focal plane of a simple lens follows a parabolic profile called Petzval surface. As illustrated in figure 8.7, the data taken for the Fresnel lens is also in good agreement with a parabolic form.

The statistical uncertainties on the distance to the Fresnel lens are taken from the accuracy to obtain the best focus from the measured development of the aberration radius in figure 8.3. For the angles of incidence θ = 0°, 2°, 4° and 6°, the distance of ± 0.4 mm to the next measurement point is taken as uncertainty, for θ = 8°, 10° and 12° a distance of ± 0.8 mm is used due to the flat development of the aberration radius R90. The uncertainty along the x-axis is negligible, since the position is measured using a micrometer screw. The good fit result gives an indication of the good alignment of the used optical components. However, the fit parameter a = $-3.490 \cdot 10^{-3}$ mm^{-1} is in contradiction to the calculated value for a = $-1/(2nf) = -0.668 \cdot 10^{-3}$ mm^{-1}. The reason for this deviation is unknown but can be caused by the usage of a Fresnel lens, as the formula for the fit parameter a is valid for conventional lenses.

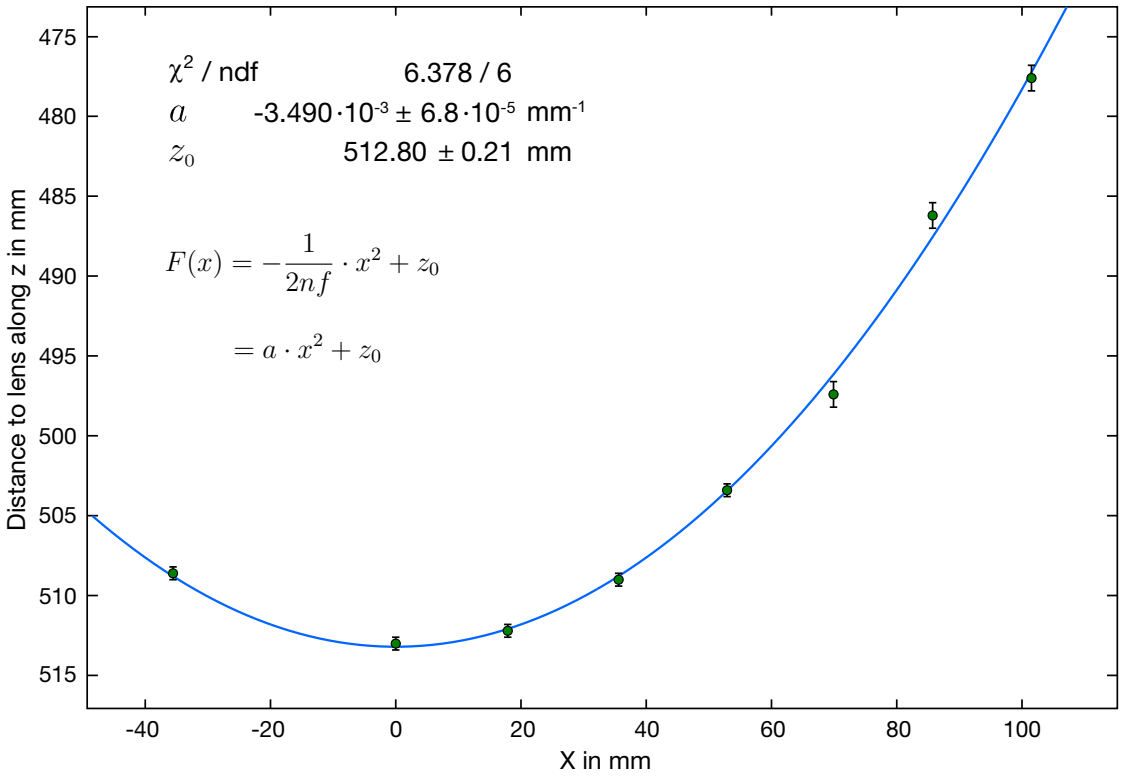

Figure 8.7: Measured focal plane of the Fresnel lens. The data can be described by a parabolic fit F(x) as predicted by Petzval field curvature. The calculation of the fit parameter a = -1/(2nf) = $-0.668 \cdot 10^{-3}$ mm^{-1} with f = 502.1 mm and n = 1.49 for the Fresnel lens leads to a contradiction to the fitted value a = $-3.490 \cdot 10^{-3}$ mm^{-1}.

A further possibility to validate the precision of alignment is given by the shift of the focal point along the x- and y-axis for different distances to the lens for an adjusted incidence angle of θ = 0°. If all components are perfectly aligned the shift along x- and y-axis has to be zero.

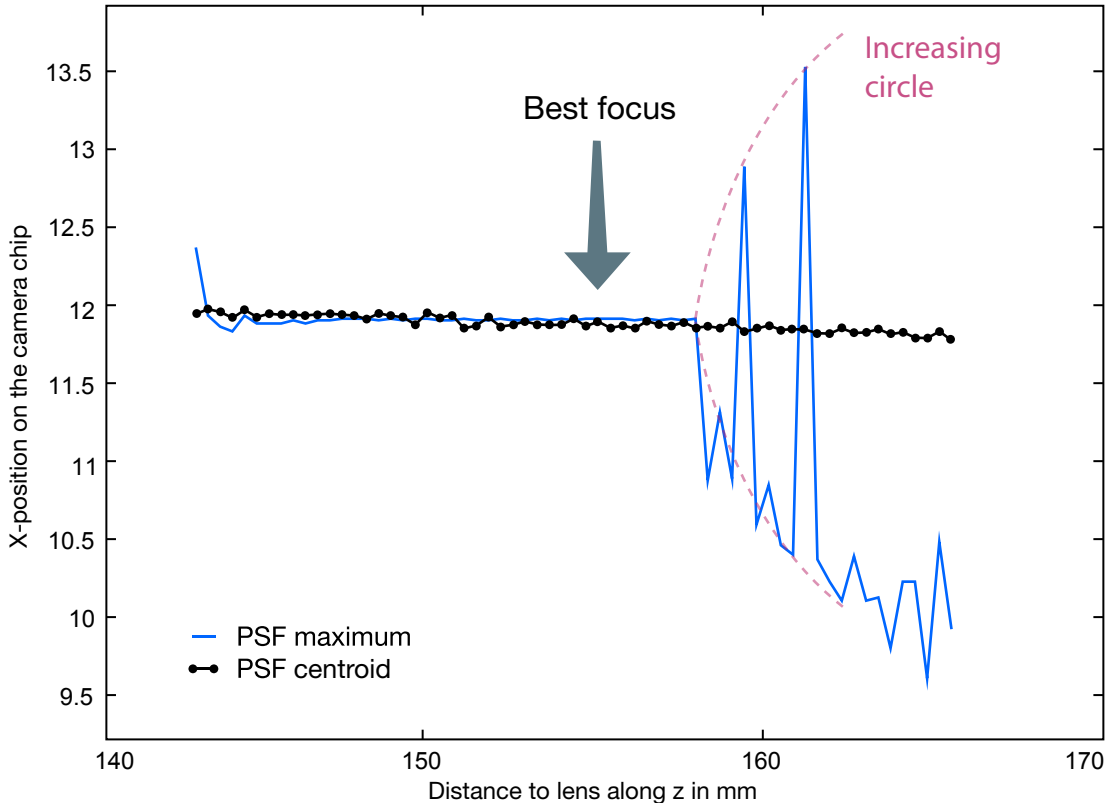

Figure 8.8: X-position of the maximum (blue) and center of gravity (black) of the measured point spread function of a conventional lens of diameter d = 75 mm and focal length of f = 150 mm for an angle of incidence θ = 0°.

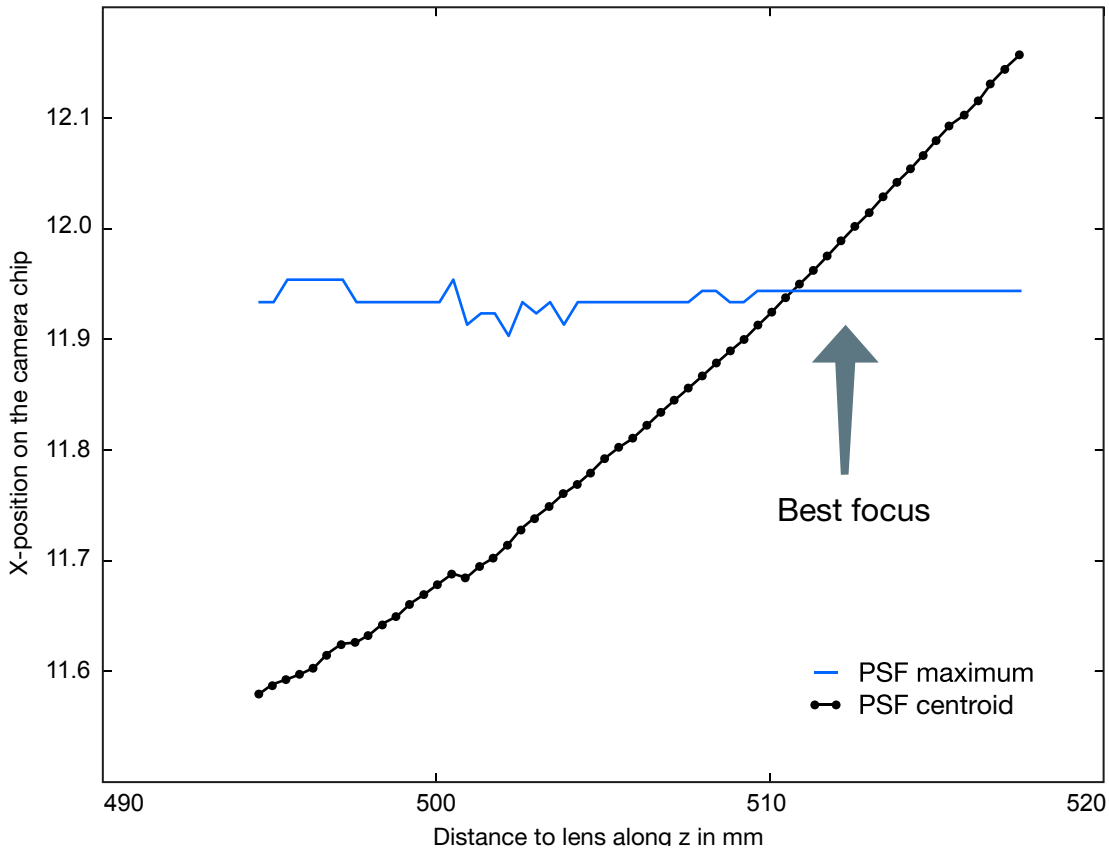

Figure 8.9: X-position of the maximum (blue) and center of gravity (black) of the measured point spread function of the Fresnel lens of FAMOUS for an angle of incidence θ = 0°.

The x-position on the image sensor of maximum[5] and center of gravity of the PSF as a function of the distance to the lens is shown in figure 8.8 for a conventional lens of diameter d = 75 mm and focal length f = 150 mm. The center of gravity and maximum position on the camera chip are in good agreement close to the best focus. The x-position of the center of gravity slightly decreases by approx. 0.15 mm on a range of 25 mm which can be caused by a misalignment of approx. 0.34° of any of the optical components. The maximum remains nearly on constant position. Right after the point of best focus the position of the maximum starts to fluctuate, which can be understood by studying the form of the PSF for this lens, presented in figure 8.10.

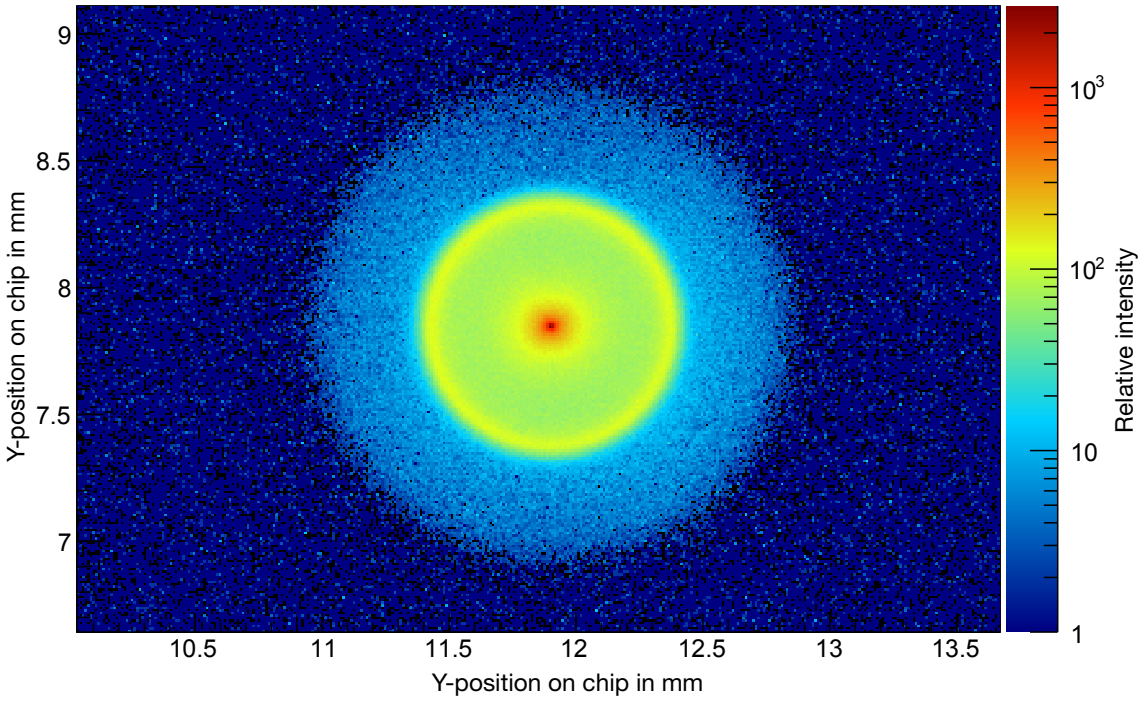

Figure 8.10: Measured best focus point spread function of a conventional lens for an angle of incidence θ = 0°. The maximum intensity in the center of the distribution is surrounded by a ring with locally higher intensity.

The global maximum intensity of the point spread function is surrounded by a circle with a local smaller maximum intensity. For defocussed positions, the global maximum intensity in the center of the point spread function decreases until the point of maximum intensity is located on the outer circle, which increases in radius while defocussing.

In figure 8.9, the x-position of center of gravity and maximum intensity of the point spread function of the Fresnel lens are presented. While the x-position of the maximum intensity is constant, the position of the center of gravity increases by roughly 1.2 mm along the x-direction, which could be caused by a missalignment of 2.75°.

To remove the described effect, the experimental setup is readjusted as a test. However, this new alignment is discarded directly, as the test bench is obviously inclined with respect to the common axis with the point light source. By this means, the original alignment can be excluded as a possible source of error.

[5]The position of the pixel with the highest intensity on the image.

In combination with the inconsistent developement of the position of center of gravity and maximum intensity for the Fresnel lens, which is not observed for the conventional lens, the experimental setup, i.e. all optical components, are assumed to be correctly aligned with an uncertainty smaller than 0.34°, which is derived from measurements with the conventional lens.

The most probable reason for the observed inconsistency between the position of center of gravity and maximum intensity is the bending of the Fresnel lens. In the experimental setup, three outer regions of the Fresnel lens are clumped into grooves of aluminim profiles without any stress, so the inner part of the lens can indulge the inner stress which is due to the different surface profiles (grooves and flat). If the inner parts of the lens are touched to change the amount of bending, the focal point starts to fluctuate heavily and the form of bending seems to have large impact on form, size and position of the focal point of the lens.

Consequently, this effect also remains the most probable reason for the observed differences between measurement and simulation. The focal length for all data points is measured from the center of the grooves of the aluminium profiles, ignoring the bending of the lens itself, which contributes to the systematical uncertainty on the focal length. Additionally, the effect of bending can have a stronger influence on the aberration radius for a small angle of incidence as the expected aberrational effects, which are induced due to higher angles of incidence, are dominant. Especially the deviation of the aberration radius for $\theta = 0°$ can be explained by this means.

With the aim to quantify the systematical uncertainty on the aberration radius, the images of the measurement with an incidence angle of $\theta = 0°$ are subdivided into a vertical and a horizontal part by using two straight lines with a slope of 45°, intersecting at the maximum intensity of the point spread function (figure 8.11). The aberration radius is calculated for both parts with the common center of the corresponding circles at the center of gravity of the total intensity distribution to reveal a deviation from rotational symmetry. For a perfect lens and a perfectly aligned experimental setup, rotational symmetry is expected.

As shown in figure 8.12, a deviation of $\Delta R90 = 0.26$ mm for the best focus aberration radius is determined. Also, a deviation in focal length of 0.4 mm in each direction for the point of best focus is detected. In a conventional approach, the effect leading to the detected deviation is assumed to be existent for all angles of incidence and its contribution to the final aberration radius R90 in comparison to other aberrational effects, which are induced due to higher angles of incidence is not known. For that reason, the systematical uncertainty on the measured aberration radii R90 is assumed to be $\Delta R90 / 2 = 0.13$ mm. Probably, the systematical uncertainty is overestimated for higher angles of incidence θ as other aberrational effects become dominant.

Additionally, it is assumed that the measured aberration radius $R90 = 2.89 \pm 0.13$ (sys.) mm for an incidence angle of $\theta = 0°$ can be reduced as predicted by simulation (cf. figure 8.5: measured aberration radius for $\theta = 0°$ and $\theta = 2°$ are equal) if the Fresnel lens is flattened perfectly.

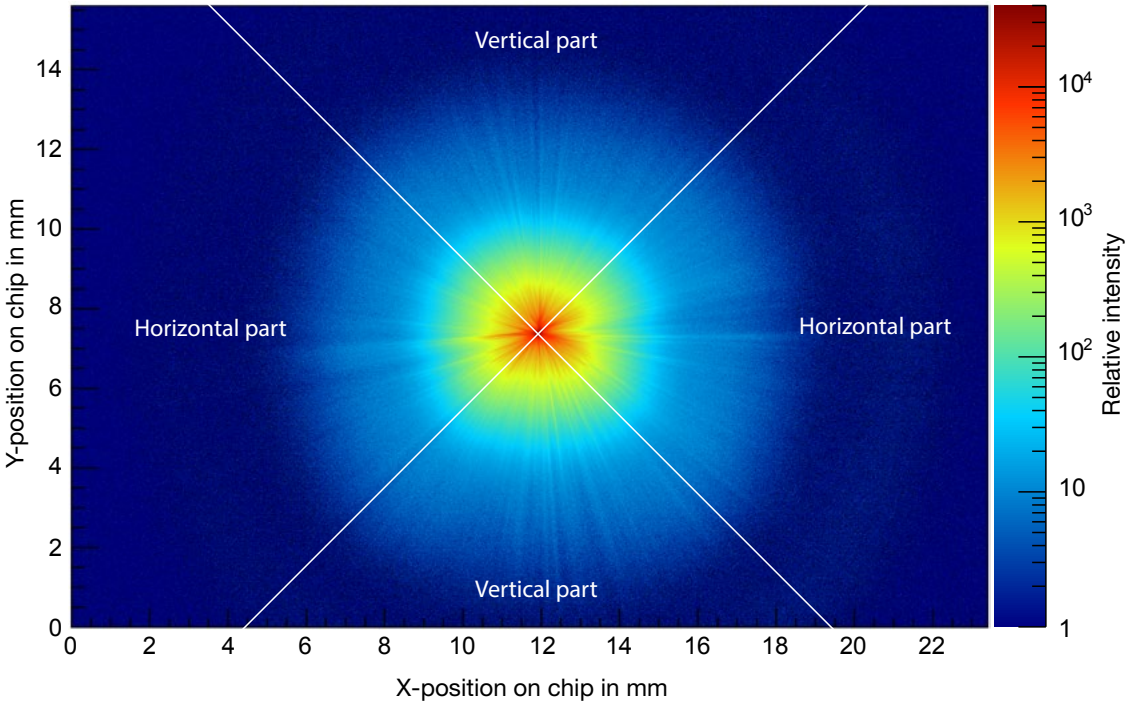

Figure 8.11: Measured best focus point spread function of the Fresnel lens for an angle of incidence θ = 0° as also shown in figure 8.2. The image is divided into a vertical and a horizontal part using two straight lines with a slope of 45°. The lines intersect at the maximum of the point spread function.

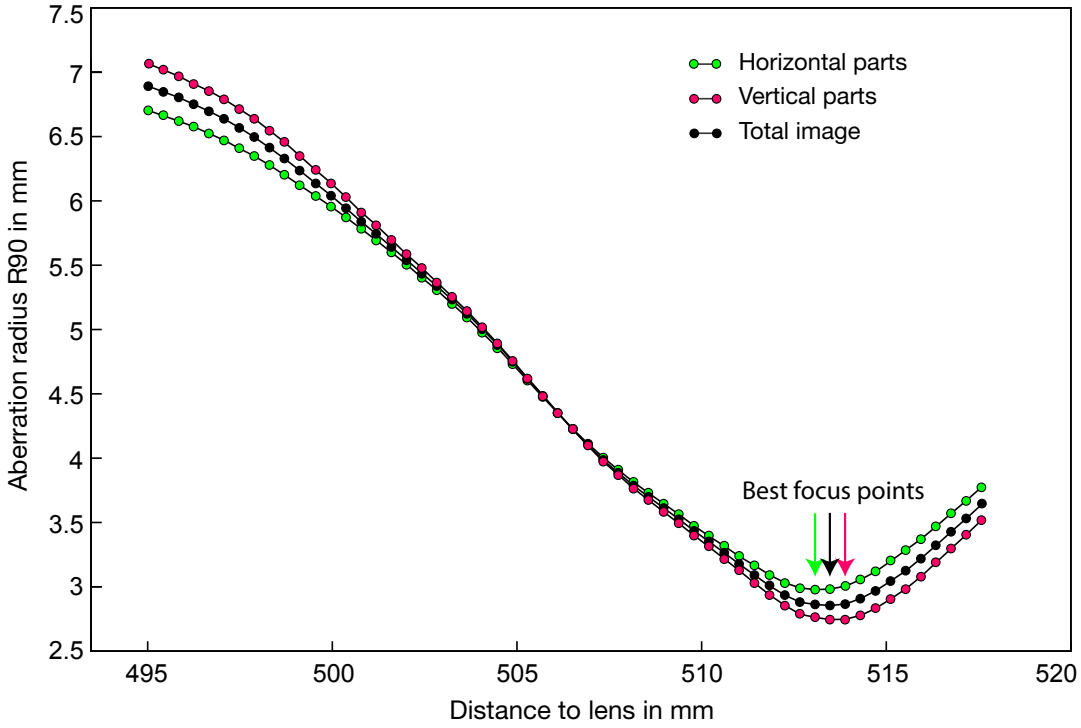

Figure 8.12: Measured aberration radius R90 as a function of the distance to the Fresnel lens for an angle of incidence θ = 0°. The aberration radius is calculated for the horizontal part (green dotted) and vertical part (red dotted) with the common center of the corresponding circles at the center of gravity of the total intensity distribution. The deviation is assumed to be caused by the bending of the Fresnel lens. For a comparison, the aberration radius for the total image is also plotted as black dotted line.

9 Transmittance

The transmittance of the Fresnel lens is an important criterion for the usage in a fluorescence telescope as it has direct influence on the photon count of an observed cosmic ray air shower. Besides the transmittance of the Fresnel lens, the transmittance and fill factor of the Winston cones in the image plane and the photon detection efficiency of the SiPMs contribute to the total detector efficiency.

The experimental setup which is used to measure the aberration radius is slightly modified to measure the transmittance of the Fresnel lens. All modifications and the procedure of measurement are presented in the following section. The measurement results are compared to the results of the simulated Fresnel lens as well.

9.1 Experimental setup and procedure of measurement

As the attenuation coefficient is typically greatly dependent on wavelength, the point light source is equipped with the UV LED which is presented in section 5.1, to reproduce the realistic situation of UV light of an extensive air shower as well as possible.

The transmittance T_i describes the ratio of the fraction of light F_i which can be detected after traversing the Fresnel lens to the total incoming light on the lens F_1:

$$T_i = \frac{F_i}{F_1} \ . \tag{33}$$

Therefore, the incoming light needs to be measured with and without lens. While the refracted portion of light is focussed to a small spot which can be captured with the image sensor of the camera, the incoming light intensity on the Fresnel lens is unknown and can not be accessed directly. For this reason, the transmittance of four smaller regions, which are radially distributed over the lens (cf. figure 9.2), are defined, to be able to capture both quantities needed.

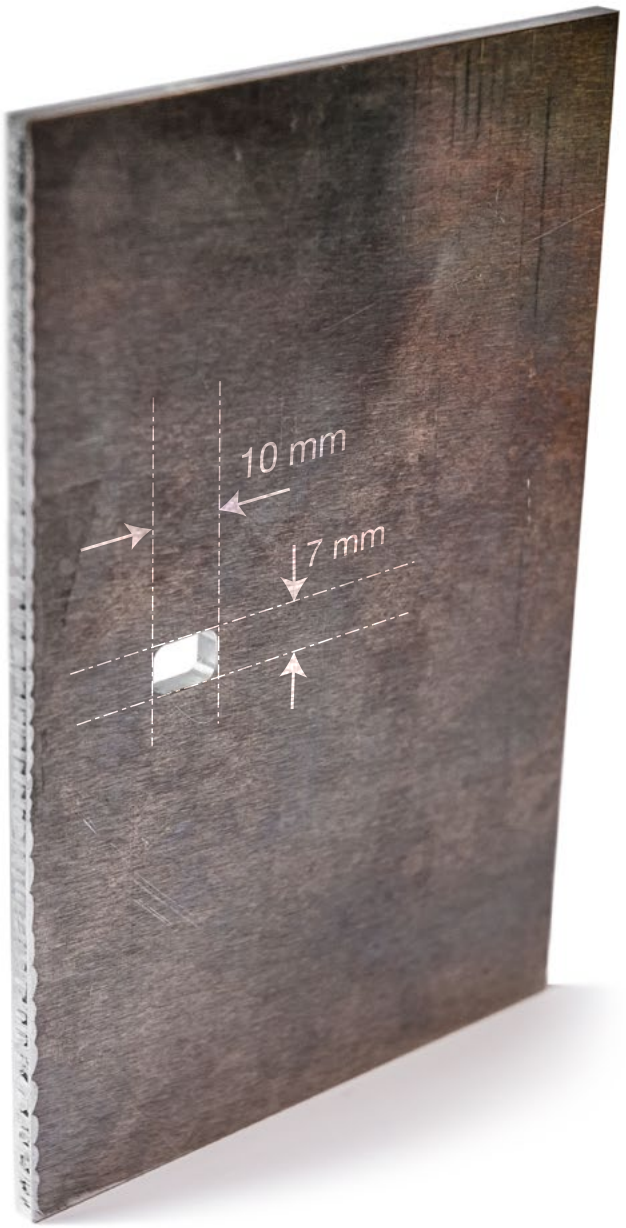

Figure 9.1: Aluminium plate with a milled window of 10 mm width and 7 mm height. The edges are rounded.

The region of interest is defined by a rectangular window with rounded edges of 10 mm width and 7 mm height, milled into an aluminium plate. A photo is shown in figure 9.1. The size of the window is chosen to be approximately half of the size of the camera sensor in each direction to be sure that all of the light passing through the window is captured.

The small window is placed directly in front of the lens (in direction to the light source), while the rest of the lens is completely covered and not illuminated. The bunch of light F_1, which passes through the defined window is refracted, scattered and also reflected by the lens.

To measure the amount of light F_2 after passing the lens (cf. figure 9.2), the camera sensor is placed as close to the lens as possible. It is important to note that the image sensor of the camera has to be aligned perpendicular to the direction of propagation of the light which

is captured as the acceptance of the image sensor depends on the angle of incidence. The direction of propagation after refraction of the lens can be calculated using the focal length of the Fresnel lens and the radial distance of the window to the center of the lens.

With each measurement, the camera chip captures a certain portion of the incoming light while the rest is reflected. The measured intensity values are not corrected for the reflection loss. If the camera chip is placed at position F_2 behind the lens, the portion of light, which is reflected from the camera chip is again reflected at the lens (cf. figure 9.2). If this portion is captured by the camera chip as well, the measured intensity for F_2 is overestimated and a transmittance of T > 100 % can be achieved wrongly. For this reason, multiple scattering has to be avoided with correct positioning of the camera (cf. figure 9.2).

The image sensor is also placed at the position of the focal point to measure the amount of light F_3 which effectively contributes to that point. For the measurement of the incoming light F_1, the Fresnel lens is removed while the position of the window remains unchanged. The light sensor is placed parallel to the aluminium plate to consider the angular acceptance of the sensor. The portion of light which is reflected from the sensor surface passes the window again and is not captured a second time.

The angular scale which is used to align the camera perpendicular to the direction of propagation of the light can be adjusted to the desired angle Φ with an accuracy of approx. 0.6°. To estimate the uncertainty which is introduced due to a false angular adjustment, three images are taken at each position F_3 and F_2. The two additional images are taken with a slightly overestimated angle $\Phi + d$ and underestimated angle $\Phi - d$ with $d \approx 1°$. The complete procedure is performed at four different radial positions of the lens.

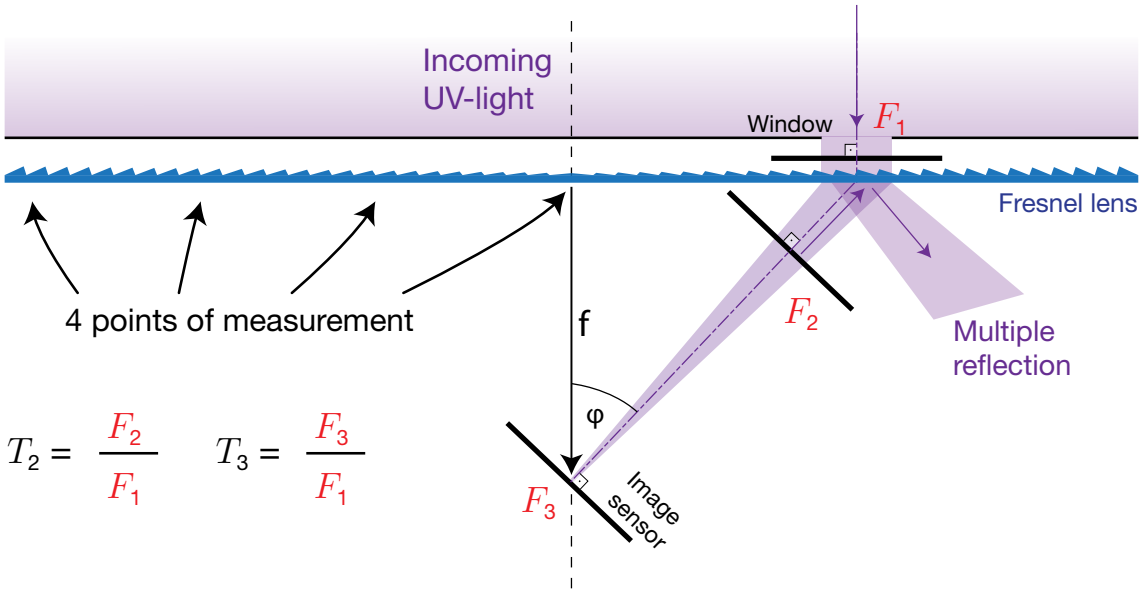

Figure 9.2: Schematic top view of the experimental setup and principle of measurement. For each of the four points of measurement, the camera is placed in three different positions to capture the total incoming light F_1 through the window, the amount of light which is refracted directly at the lens F_2 and the effective portion of light F_3 which contributes to the focal point.

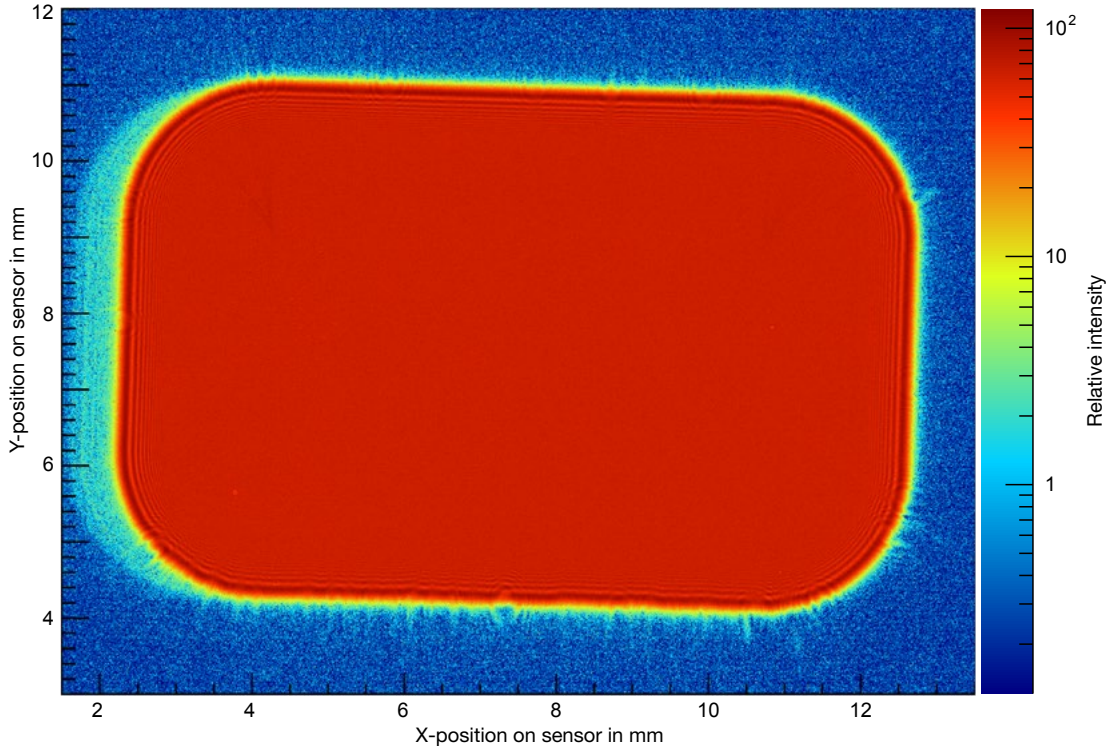

Figure 9.3: Captured image of the light passing through the window at position F_1 without lens.

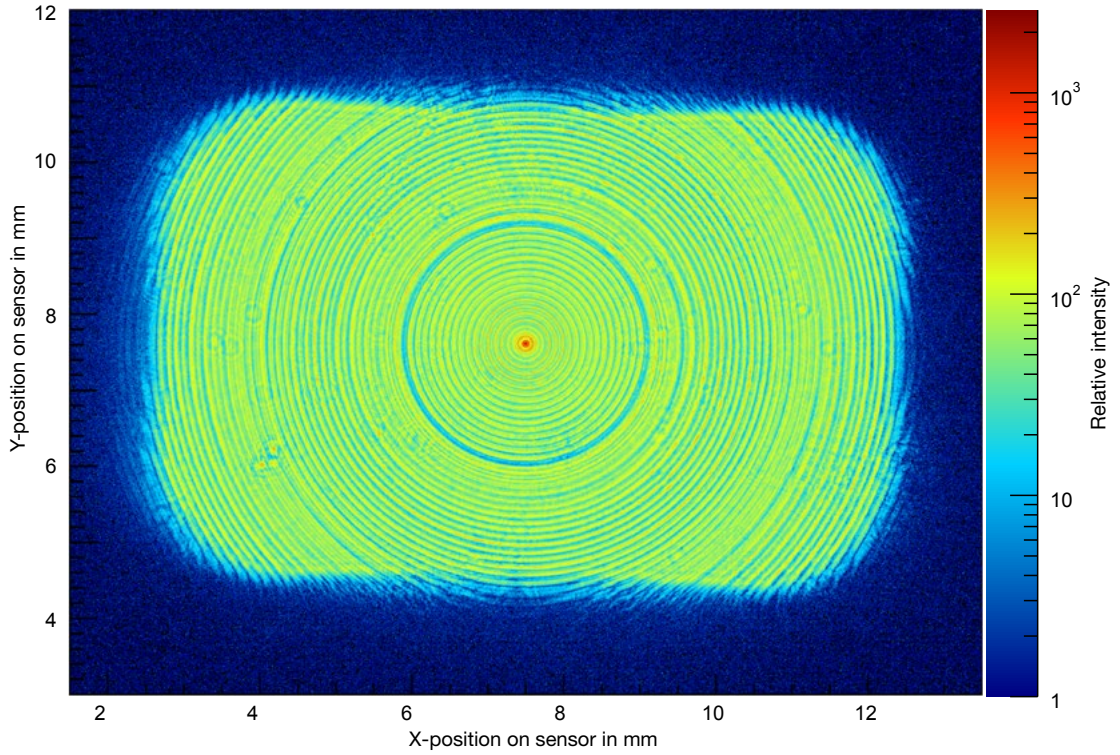

Figure 9.4: Captured light after passing the window and the center of the Fresnel lens at position F_2.

9.2 Measured and simulated results

For the analysis of the measurement, the ratio of the integrated blue pixel intensities of the corresponding camera raw files is formed. The intensity distributions of the camera positions F_1 and F_2 are shown in figure 9.3 and figure 9.4. For each point of measurement, the three images taken with slightly different angles Φ are processed independently resulting in three values for the transmittance of each point. The mean of these values is plotted as actual transmittance and the maximum deviation is taken as systematic uncertainty. The statistical uncertainty is neglibigle as the fluctuation of $\approx 10^6$ pixels of the camera is averaged on integration.

The measured values of transmittance T_2 close to the lens (F_2) are plotted as black line in figure 9.5 and the transmittace related to the focal point T_3 is plotted as red line. While the center of the Fresnel lens reaches a peak transmittance of $T_3 \approx 81\,\%$ for the focal point, the outer regions drop to $T_3 \approx 40\,\%$. The effective transmittance T_3 at the focal point is systematically reduced by 10 % (absolutely) in comparison to the transmittance measured close to the lens T_2 due to a component of the light, which is not correctly focussed, but still captured by the camera at position F_2.

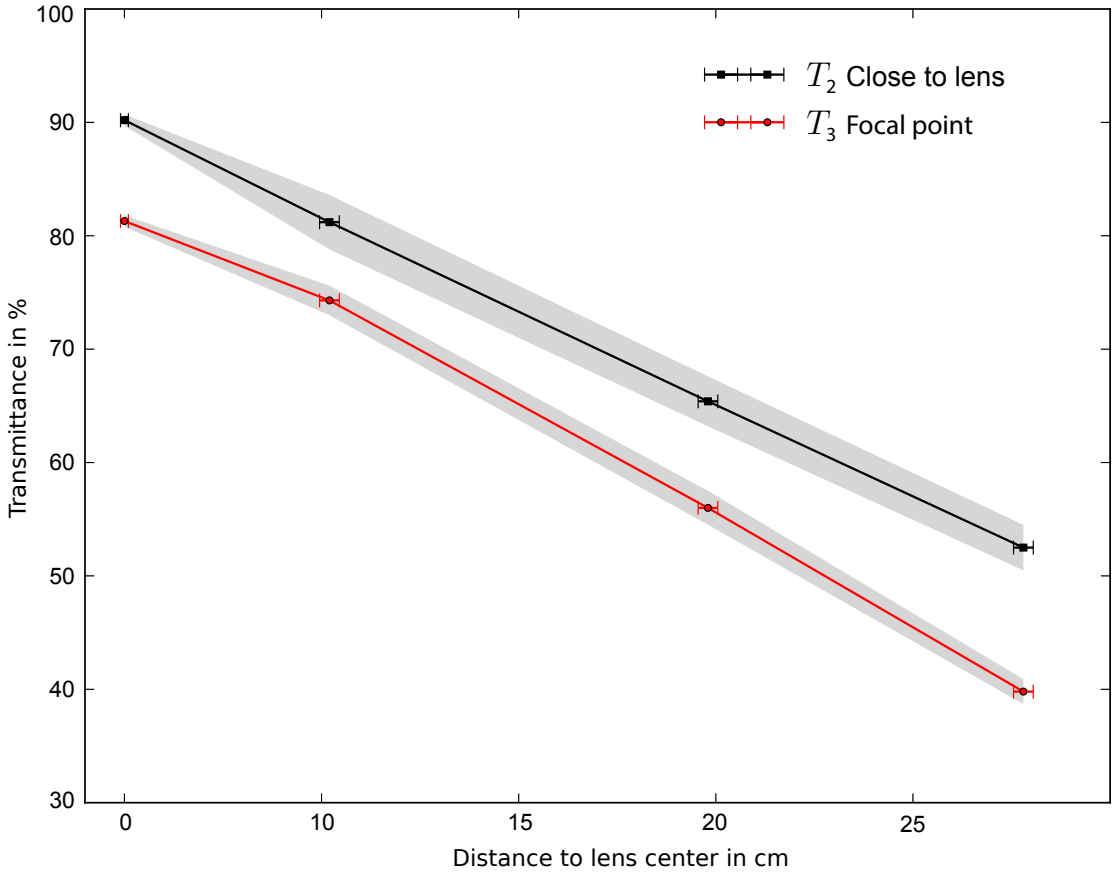

Figure 9.5: Measured transmittance of the Fresnel lens as function of the distance to the center of the lens. The black line represents the transmittance measured close to the lens at position F_2 while the red line represents the transmittance measured at the focal point at position F_3.

The linear relationship between the transmittance and the distance to the center of the Fresnel lens as illustrated in figure 9.5 can be understood with the radially increasing slope and draft angles of the grooves, which result in a radially decreasing size of the active face of the grooves. Additionally, the transmission coefficient for light decreases for an increasing slope of the active face of the grooves.

The total transmittance for $\theta = 0°$ of the Fresnel lens $T_{\text{total}} = 50.5 \pm 2\,(\text{sys.})\,\%$ is estimated by the weighted mean of the measured radial values. The weight for each measurement point is the circumference with the radial distance of the center of the window to the center of the lens. For the weight of the measured value at the center of the lens, half of the width of the window (3.5 mm) is used.

The transmittance of the simulated lens $T_{\text{sim}} = 61.2 \pm 1.8\,(\text{stat.})\,\%$ is derived by the quotient of all photons arriving at the lens and the number of photons hitting the small focal plane (23.3 mm width and 15.6 mm height). The statistical uncertainty is involved due to the limited photon number of 10^4 for the simulation. The large difference between simulation and measurement could not be examined but has to be incorporated and considered in the detector response simulation. The trigger probability of FAMOUS, shown in figure 3.8, is expected to decrease for a reduced transmittance of the Fresnel lens.

10 Summary and Outlook

The fluorescence telescope FAMOUS is a prototype which uses SiPMs as active detector component to detect extensive air showers. The telescope uses a refractive optical design with a Fresnel lens of a diameter D = 549.7 mm and a focal length of f = 502.1 mm. A thickness of only 2 mm and a granularity of 10 grooves per mm promise a high transmittance for light of λ = 350 nm and an imaging performance which is good enough to focus the incoming light onto the circular pixels with an entrance radius of r = 6.71 mm.

To measure the spot size of the focal point and the transmittance of the Fresnel lens, an experiment is designed and performed and a measurement procedure is developed. To process and analyse the recorded data, a special software is developed. The aberration radius R90 is used to describe the size of the focal point and is defined by a circle containing 90 % of the captured light intensity on the image plane.

A simulation program of a Fresnel lens, created by Tim Niggemann [18], is further developed to gain insight into its functioning and to enhance the detector response simulation of FAMOUS. The sizes of the simulated and measured focal points for a field of view of 12° show reasonably good agreement, while the transmittance of the Fresnel lens is overestimated by 10 % in the simulation, which can be caused by many traces of usage like fingerprints, scratches and dust on the measured lens. These are not considered in the simulation.

The best (compromising) focal length of the inspected Fresnel lens for a field of view of 6° and a flat image plane is determined to 505 - 507 mm. In that case, the maximum spot sizes of the focal points are determined to be smaller than 5 mm, which is 25 % less than the pixel size of FAMOUS. Theoretically, the spread of the focal point over multiple pixels could be used to gain additional information about the maximum of the point spread function, as a low resolution picture of its shape can be obtained. To make use of the best imaging performance of the lens, a curved image plane is recommended.

The optical performance of the chosen Fresnel lens suffices for the use in the fluorescence telescope FAMOUS. However, the transmittance of roughly 50 % for light of 400 nm wavelength deviates from the simulation. To enhance the transmittance and optical performance, the manufacturer recommends the usage of a Fresnel lens with reduced granularity of about 2 grooves per mm. The best performance is expected for a Fresnel lens with radially increasing granularity, while the active face of the inner grooves is not approximated by a linear slope.

Regarding the fact that the aberration radius R90 for an inclination angle $\theta = 8°$ is smaller than the pixel size of FAMOUS, the field of view can easily be extended to $2 \cdot 8° = 16°$ for a flat image plane. Using a curved image plane, the field of view can even be further extended.

The bending of the Fresnel lens seems to have influence on the measured aberration radius. To quantify this effect, a series of measurements is recommended, with the aim to study the dependence between the aberration radius R90 and the bending. A tiny hole in the center of the Fresnel lens with a string attached can be used to achieve a controlled bending. By this means, the prediction for the aberration radius R90 of the simulation for an incidence angle $\theta = 0°$ can be verified.

References

[1] http://timelessphotography1.co.uk/ - 2012.

[2] J. R. Hörandel, “On the knee in the energy spectrum of cosmic rays”, Astroparticle Physics, vol. 19, no. 2, pp. 193-220, 2003.

[3] B. Falkenburg and W. Rhode, “From Ultra Rays to Astroparticles”, pp 34, Springer Verlag, 2012.

[4] Particle Data Group, Review of particle physics. Journal of physics, Inst. of Physics Publ., 2011.

[5] D. R. Bergman and J. W. Belz, “Cosmic Rays, The Second Knee and Beyond”, The State University of New Jersey, Department of Physics and Astronomy, Piscataway, New Jersey, USA, arXiv:0704.3721v1, 2007.

[6] The Pierre Auger Collaboration, “The Pierre Auger Observatory: results on the highest energy particles”, arXiv:1307.3956v1, 2013.

[7] J. Blümer, R. Engel, and J. Hörandel, “Cosmic rays from the knee to the highest energies” Progress in Particle and Nuclear Physics, vol. 63, no. 2, pp. 293-338, arXiv:0904.0725v1, 2009.

[8] Todor Stanev, High Energy Cosmic Rays, pp 249, Springer Verlag, 2010.

[9] R. D. Evans, “Atomic Nucleus”, Chapter 25 p. 713, McGraw-Hill New York, 1955.

[10] L. Perrone, S. Petrera and F. Salamida, “Gaisser-Hillas Profiles and FD Simulation”, University of Wuppertal, GAP-2005-087, 2005.

[11] The Pierre Auger Collaboration, “The Fluorescence Detector of the Pierre Auger Observatory”, Nuclear Instruments and Methods in Physics Research Section A: Accelerators, Spectrometers, Detectors and Associated Equipment, arXiv:0712.2832v1, 2010.

[12] The AIRFLY Collaboration, “Precise measurement of the absolute fluorescence yield of the 337 nm band in atmospheric gases”, arXiv:1210.6734v1, 2012.

[13] A. Obermeier, “The Fluorescence Yield of Air excited by Electrons measured with the AIRFLY Experiment”, Institut für Kernphysik, Forschungszentrum Karlsruhe, 2007.

[14] F. Arqueros, J. R. Hörandel, Bianca Keilhauer, “Air Fluorescence Relevant for Cosmic-Ray Detection”, El Escorial, arXiv:0807.3760v1, 2007.

[15] P. Assis, P. Gonçalves, M. Pimenta, “Simulation of the fluorescence telescopes of the Pierre Auger Observatory using GEANT4”, Laboratório de Instrumentação e Física Experimental de Partículas (LIP), Lisbon, GAP-2009-104, 2009.

[16] The Pierre Auger Collaboration, “The Surface Detector System of the Pierre Auger Observatory”, Nuclear Instruments and Methods in Physics Research Section A: Accelerators, Spectrometers, Detectors and Associated Equipment, arXiv:0712.2832v1, 2008.

[17] J. Brack et al. “Characterization of the Hamamatsu R11780 12 inch Photomultiplier Tube”, arXiv:1210.2765v2, 2013.

[18] T. Niggemann, “New Telescope Design with Silicon Photomultipliers for Fluorescence Light Detection of Extensive Air Showers”, Master thesis, Phys. Inst. III A, RWTH Aachen University, Aachen, 2012.

[19] M. Stephan, T. Hebbeker, M. Lauscher, et al. “Future use of silicon photo-multipliers for the fluorescence detection of ultra-high-energy cosmic rays”, SPIE, 8155 81551B-1, Inst. III A, RWTH Aachen University, Aachen, 2011.

[20] M. Lauscher, “Characterisation Studies of Silicon Photomultipliers for the Detection of Fluorescence Light from Extensice Air Showers”, Master thesis, Phys. Inst. III A, RWTH Aachen University, Aachen, 2012.

[21] T. Niggemann, T. Hebbeker, M. Lauscher, et al. “The Optics and Detector-Simulation of the Air Fluorescence Telescope FAMOUS for the Detection of Cosmic Rays”, Inst. III A, RWTH Aachen University, Aachen, 2012.

[22] C. Peters, “Design Studies for an Air Fluorescence Telescope with Silicon Photomultipliers for the Detection of Ultra-high-energy Cosmic Rays”, Master thesis, Phys. Inst. III A, RWTH Aachen University, Aachen, 2013.

[23] J. F. Healy, “Pliny the Elder on Science and Technology“, Oxford University Press, 1999.

[24] H. C. King, “The history of the telescope”, Dover Publications, 2011.

[25] W. Bruce, “Science Makes a Better Lighthouse Lens.” Smithsonian magazine, v30 i5 p30, August 1999.

[26] G. Kweon, “Aspherical Lens Design by Using a Numerical Analysis”, 2007.

[27] E. Hecht, “OPTICS”, fourth edition, pp. 529, Adelphi University, 2002.

[28] W. Heisenberg, “The Physical Principles of the Quantum Theory”, University of Chicago Press, Chicago, 1930.

[29] H. Gross, W. Singer and M. Totzeck, Handbook of Optical Systems: Physical image formation. Wiley-VCH, 2005.

[30] A. Davisa, K. Levesqueb, S. Wilta, “Prism peak rounding in injection molded Fresnel lens solar concentrators”, Reflexite Energy Solutions, 500 Lee Rd., Rochester, NY, USA 14606, 2011.

[31] Rivolta, Applied Optics, 25, 2404, 1986.

[32] A. P . WOOD, “Image forming infrared Fresnel lenses”, JOURNAL OF MODERN OPTICS, VOL. 37, NO. 8, 1329-1342, 1990.

[33] R. Kräzler, “Messprotokoll Nr. 0286 5mm Superhelle LED UV”, LUMITRONIX LED-Technik GmbH, Haigerlocher Str. 42, 72379 Hechingen, 2008.

[34] “Sony NEX 5 Service Manual LEVEL 1”, Sony Techno Create Corporation, 2010.

[35] Reflexite Energy Solutions, private communication, 2013.

[36] L. W. Kheng, “CS4243 Computer Vision and Pattern Recognition “, National University of Singapore, 2011.

[37] S. B. Howell, “Handbook of CCD Astronomy”, Cambridge University Press, 2006.

[38] M. Abramowitz, S. H. Neaves and M. W. Davidson, “Human Vision and Color Perception”, The Florida State University, 2003.

[39] B. E. Bayer, “Color imaging array”, Eastman Kodak Company, 1976.

[40] http://www.libraw.org - 2013.

[41] “Sony NEX-5 Imatest Results”, Imaging Resource, http://www.imaging-resource.com/PRODS/NEX5/NEX5IMATEST.HTM - 2013.

Acknowledgements - Danksagungen

An dieser Stelle danke ich all denjenigen, die mir während des letzten Jahres bei der Erstellung dieser Masterarbeit zur Seite gestanden haben.

Herrn Prof. Dr. Thomas Hebbeker danke ich dafür, dass ich diese Forschungsarbeit an seinem Institut durchführen konnte und vor allem dafür, dass er mir eine praxisorientierte Arbeit für das Pierre Auger Observatorium ermöglicht hat. Er gab mir stets neue Impulse, die mir dabei halfen, Probleme zu lösen und einen anderen Blickwinkel zu bekommen. Ebenfalls danke ich Herrn Prof. Dr. Christopher Wiebusch für seine Bereitschaft, das Zweitgutachten meiner Arbeit anzufertigen.

Ein großer Dank gilt auch meinem Betreuer Tim Niggemann, der mich mit viel Geduld und Akribie beraten hat und sich auch durch intensives Korrekturlesen verdient gemacht hat, und den Mitarbeitern der Auger Arbeitsgruppe des III. Physikalischen Instituts A der RWTH Aachen, die mir jederzeit hilfreich zur Seite standen. Auch Lukas Middendorf danke ich für seine Hilfe bei der Erstellung der benötigten Software, Maurice Stephan für seine alternativen Ansätze und Ideen, sowie Christine Peters für ihre hilfreichen Hinweise beim Korrekturlesen.

Ich bedanke mich bei den Mitarbeitern der Mechanik-Werkstatt des Instituts für die gute Zusammenarbeit bei der Anfertigung des Versuchsaufbaus, insbesondere Herrn Barthel Philipps, der mich jederzeit mit Rat und Tat unterstützt hat.

Mein Dank geht auch an Janina Rüttgers, die mir während der zeitaufwändigen Messreihen half und an meine Schwester Claudia für ihr Englisch-Lektorat.

Nicht zuletzt geht ein sehr großer Dank an meine Eltern, für ihre große Geduld, moralische Unterstützung und ihren Glauben an mich. Ohne deren Fürsorge, auf die ich mich immer verlassen konnte, wäre ein solches Studium nur schwer möglich gewesen.

Erklärung

Hiermit versichere ich, dass ich diese Arbeit einschließlich beigefügter Zeichnungen, Darstellungen und Tabellen selbstständig angefertigt und keine anderen als die angegebenen Hilfsmittel und Quellen verwendet habe. Alle Stellen, die dem Wortlaut oder dem Sinn nach anderen Werken entnommen sind, habe ich in jedem einzelnen Fall unter genauer Angabe der Quelle deutlich als Entlehnung kenntlich gemacht.

Aachen, den 10. März 2014

Hans Michael Eichler